REVIEW ARTICLE

Digital particle image thermometry/velocimetry: a review

Dana Dabiri

Abstract Digital particle image thermometry/velocimetry (DPIT/V) is a relatively new methodology that allows for measurements of simultaneous temperature and velocity within a two-dimensional domain, using thermochromic liquid crystal tracer particles as the temperature and velocity sensors. Extensive research has been carried out over recent years that have allowed the methodology and its implementation to grow and evolve. While there have been several reviews on the topic of liquid crystal thermometry (Moffat in Exp Therm Fluid Sci 3:14–32, 1990; Baughn in Int J Heat Fluid Flow 16:365–375, 1995; Roberts and East in J Spacecr Rockets 33:761–768, 1996; Wozniak et al. in Appl Sci Res 56:145–156, 1996; Behle et al. in Appl Sci Res 56:113–143, 1996; Stasiek in Heat Mass Transf 33:27–39, 1997; Stasiek and Kowalewski in Opto Electron Rev 10:1–10, 2002; Stasiek et al. in Opt Laser Technol 38:243–256, 2006; Smith et al. in Exp Fluids 30:190–201, 2001; Kowalewski et al. in Springer handbook of experimental fluid mechanics, 1st edn. Springer, Berlin, pp 487–561, 2007), the focus of the present review is to provide a relevant discussion of liquid crystals pertinent to DPIT/V. This includes a background on liquid crystals and color theory, a discussion of experimental setup parameters, a description of the methodology's most recent advances and processing methods affecting temperature measurements, and finally an explanation of its various implementations and applications.

Abbreviations

CCD	Charge-coupled device
CIE	Commission International de l'Éclairage
CLC	Cholesteric liquid crystal
CNLC	Chiral nematic liquid crystals
DPIT	Digital particle image thermometry
DPIT/V	Digital particle image thermometry/ velocimetry
DPIV	Digital particle image velocimetry
HWA	Hot wire anemometry
LDA	Laser-Doppler anemometry
MTV&T	Molecular tagging velocimetry and thermometry
LIF	Laser-induced fluorescence
NTSC	National Television Systems Committee
POD	Proper orthogonal decomposition
RTD	Resistance temperature detector
TLC	Thermochromic liquid crystals
PAL	Phase altering line
SECAM	Séquentiel couleur à mémoire
NTSC	National Television Standards Committee
HSI	Hue, saturation, intensity
RGB	Red, green, blue color space

D. Dabiri (✉)
Department of Aeronautics and Astronautics,
University of Washington, Box 352400,
Seattle, WA 98195, USA
e-mail: dabiri@aa.washington.edu

1. Introduction

Convective heat transfer is perhaps one of the most frequently encountered physical processes in applied engineering. It can be a combination of laminar and/or turbulent flows that contain natural and/or forced convective heat transfer, which can be further complicated by the effects of complex geometries in which they occur. While laminar convective heat transfer is well understood, turbulent convective heat transfer is not, making its prediction using numerical methods often difficult and inaccurate. To achieve such an understanding necessitates obtaining knowledge of the three-dimensional turbulent flow fields globally, with very high spatial and temporal resolution. While we are still far from fully achieving this realization, significant progress has been made towards this goal during the last two decades. Early quantitative measurement methods (Pitot tubes, thermistors, thermocouples, RTDs, etc.) and later techniques, such as hot wire anemometry (HWA) and Laser-Doppler anemometry (LDA) were, by their nature, measurement methods that provided instantaneous measurements at single-points through time. Early

emphasis in turbulence research and its theoretical advancement therefore necessitated a statistical description of turbulent flow fields, which relied heavily upon these single-point measurement techniques. Though useful, these statistical single-point descriptions did not provide a clear instantaneous picture of the fluid's global behavior, and how its instantaneous physics ultimately result in the fluid's statistical behavior.

Since the early 1970s, the discovery of the existence of three-dimensional coherent structures within turbulent flows (Brown and Roshko 1974) using qualitative flow visualization methods (i.e. shadowgraphs, Schlieren systems, dye injection, etc.) has provided another viewpoint towards turbulence that has been of significant interest. While flow visualization using tracers have been documented since the days of Prandtl and Tietjens (1934), it is only recently that the advent of modern imaging, laser, and data acquisition technology has allowed for the *qualitative* flow visualization of these coherent structures using such tracers to become *quantitative*. These advances have allowed for the development and advancement of a relatively new measurement technique, digital particle image velocimetry (DPIV) (Adrian 1984, 1988, 1991; Lourenco et al. 1989; Willert and Gharib 1991; Keane and Adrian 1992; Westerweel 1993, 1997; Grant 1994; Melling 1997; Gharib and Dabiri 2000; Mckeon et al. 2007), which allows for the global measurement of two-component velocities within a two-dimensional domain through time. Because of its ability to provide global two-dimensional kinematic information, as well as its ability to map the evolution of coherent structures through time, DPIV has become a powerful and effective tool in studying, understanding, and modeling fluid flow behavior.

Another unique method that has been developed as a consequence of the quantification of flow visualization, and has impacted the thermo-fluid sciences, is digital particle image thermometry/velocimetry (DPIT/V). This technique, which uses thermochromic liquid crystals (TLCs), is capable of simultaneously measuring temperature and velocity. When illuminated with white light, TLCs have the distinctive ability of selectively scattering different colors depending on their surrounding temperature, hence providing a way to measure temperature. Therefore, if microencapsulated TLCs are used to seed the flow, then their motion will provide the velocity content, while their color variations will provide the temperature content (see Fig. 1).

This review paper will therefore discuss in detail the different components that comprise and affect the performance of the DPIT/V method, as well as its various implementations, evolutions, and applications. Specifically, Sect. 2 will discuss the properties of thermochromic liquid crystals, their various phases, and optical properties;
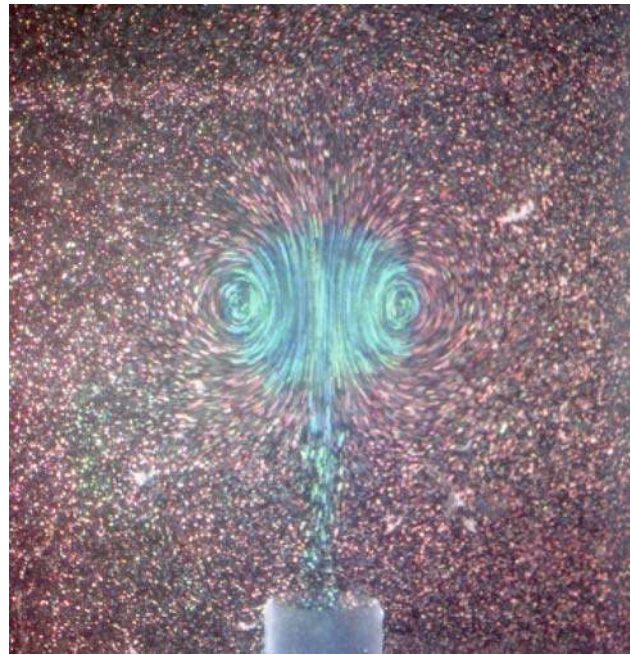
Fig. 1 Qualitative visualization of a heated vortex ring using thermochromic liquid crystals illuminated with a xenon white light source. The local color reflections are a consequence of the local temperatures, red corresponding to the lowest temperature and blue corresponding to the highest temperature

Sect. 3 will describe color theory and its use towards measuring color reflections from the TLCs; Sect. 4 will describe the various components that comprise the DPIT/V technique; Sect. 5 will discuss temperature calibration methods and uncertainty analysis, Sect. 6 will discuss the development of three-dimensional methods, and Sect. 7 will present areas in which the DPIT/V technique has been applied. Finally, Sect. 8 will conclude with a section on future trends.

2. Properties of thermochromic liquid crystals

2.1 General description of liquid crystals

The name 'liquid crystal' is, at first thought, seemingly composed of two contradictory words—a crystal generally defines a highly organized rigid molecular structure, while a liquid generally contains loosely organized, even randomly distributed, molecules that, unlike a solid, cause it to fill to the confines of its container. Yet nature does allow for substances that contain properties of both liquids and solids to exist, hence their given name—'liquid crystals'. Historically, Loebisch (1872) and Rayman (1887) initially observed the characteristic color play of cholesterol derivatives in the late 1800s. However, it was Friedrich Reinitzer (1888), an Austrian botanist, who in 1888 first

noted the appearance of two distinct melting points in what later became known as cholesteryl benzoate at 145°C, the solid melted into a cloudy liquid, and at 179°C, the liquid became clear. After communicating this discovery to Lehmann (1889), Lehmann showed that the liquid is birefringent, which is characteristic of crystals. As this compound exhibited characteristics of both liquids and crystals, he chose the name 'liquid crystals' for this newly discovered state of matter (Fergason 1964; Adams et al. 1969; Kawamoto 2002).

In general, liquid crystals are truly liquids, with viscosities ranging within 10–100 mPa s, but containing long-range order in the orientation of their molecules. This long-range order, which is due to intermolecular forces, is, however, susceptible to environmental changes that can produce dramatic changes in their macroscopic properties (Kahn 1982). Liquid crystals are broadly characterized as, lyotropic, polymeric, or thermotropic (Litster and Birgeneau 1982; Pershan 1982; Samulski 1982). Lyotropic liquid crystal molecules are typically hydrophilic at one end and hydrophobic at the other end (hence amphiphilic), such that when dissolved in a polar solvent, will exhibit liquid crystalline behavior. The concentration of these molecules within the solvent will determine its phase, since its concentration will cause the molecules to self-assemble into different phases.[1] Polymeric liquid crystals refer to polymer molecules that in the liquid phase, similar to the non-polymer molecules, exhibit crystalline behavior. Thermotropic liquid crystals are typically formed of rod or disk-shaped molecules, whereby the temperature determines the liquid crystal's various phases. In the DPIT/V technique, thermotropic liquid crystals are favored since the slight variation of their phase due to temperature directly affects their ability to scatter different colors. Towards this end, we focus below on the different phases and properties of thermotropic liquid crystals.

2.2 Phases of thermotropic liquid crystals

The phases of thermotropic liquid crystals, based on a system proposed by Freidel (1922), are broadly classified as the smectic, nematic and cholesteric phases. Detailed descriptions of these classes as well as their optical properties can be found in the literature (i.e. Mathieu 1911; Fergason 1964, 1966, 1968; Adams et al. 1969; Litster and Birgeneau 1982; Elser and Ennulat 1976; Oseen 1933; McDonnell 1987; Gleeson and Coles 1989; Pohl and Finkenzeller 1990; Demus and Chemie 1990; Sage 1990;

_____

[1] Perhaps the most common example of a lyotropic liquid crystal is soap, where the molecules will line up such that their hydrophobic ends will face the outer side of the soap bubble surface, while the hydrophilic ends will face the inner side of the soap bubble surface.
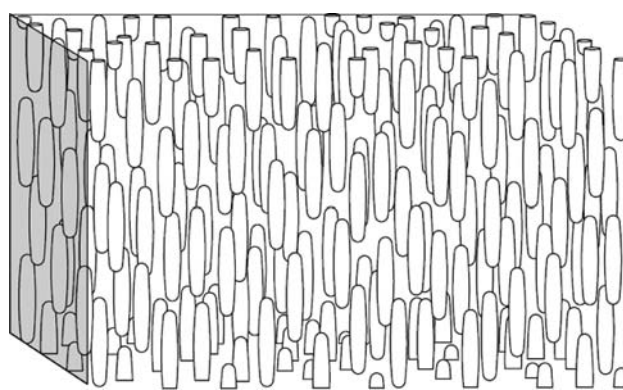
Fig. 2 Schematic of the orientation of nematic liquid crystal molecules (adapted from Mitchell 2004)

Gennes and Prost 1993; Collings 2002). In this and the following sections, the main results of such works relevant to this review are given.

2.2.1 Nematic and smectic phases

In his observation of these materials, Freidel noticed that they contained microscopic threadlike structures that floated freely, or attached to the surface of the container (Fig. 2). Accordingly, he chose to call this phase the *nematic* (meaning *thread*) phase. This is the simplest and least ordered phase of thermotropic liquid crystals, since their long cigar-shaped molecules are only uniaxially oriented.

Freidel also observed another more ordered phase of these liquid crystals. For this phase, the molecules self-arranged side-by-side in a series of layers. In some materials, the molecules within each layer self-arrange in a lattice format (Fig. 3a), while in other compounds the molecules within each layer are randomly distributed (Fig. 3b). The molecular forces are such that the layers freely slide over one another, displaying fluid-like behavior, while appearing as a solid in motions orthogonal to the layers, since the layers do not interpenetrate. Because of this "soapy" property, Freidel called this the *smectic* (meaning *soap*) phase.

2.2.2 Cholesteric phase

Freidel called this phase cholesteric, since when first discovered, these molecules had characteristics of cholesteric compounds. This phase contains aspects of both the nematic and smectic phases. Similar to the smectic phase, the molecules self-arrange into layers. In each layer the molecules randomly self-arrange uniaxially, similar to the nematic phase, though in this case, in the direction of the plane. Instead of being cigar-shaped, the cholesteric liquid crystal (CLC) molecules are flat, with a side chain of
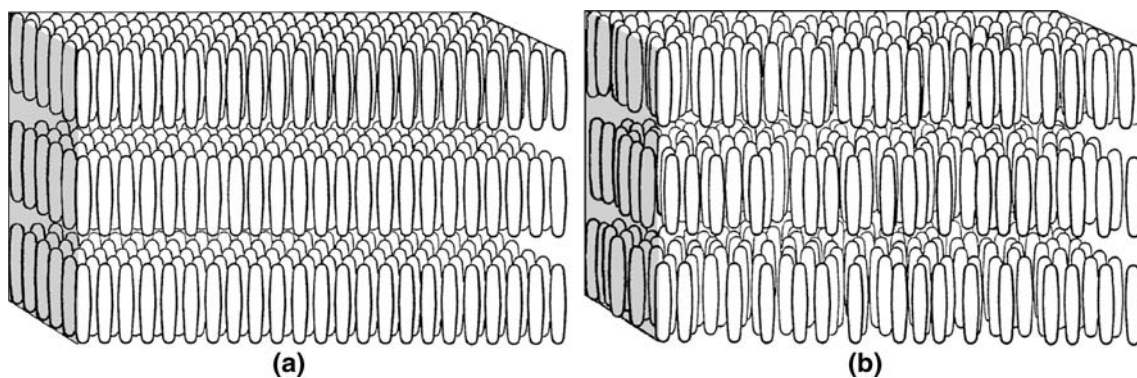
Fig. 3 Schematic of a smectic phase where the liquid crystal molecules are uniaxially aligned in layers. Variations of the smectic phase where in each layer **a** the molecules are further organized, **b** the molecules are randomly distributed (adapted from and Mitchell 2004)

methyl groups (CH$_3$) and other parts of the molecule that project out-of-plane (shown in gray) from the main part of the molecule (shown in black) (see Fig. 4). Because of this asymmetric tilting of the molecule, the directions of the long axes of the molecules in each layer are slightly displaced from those in adjacent layers. This displacement, shown in Fig. 4, averaging about 15 arc minutes per layer, accumulates from one layer to the next, tracing out a helical path that defines a pitch for the liquid crystal (Oseen

1933). The direction in which the molecules are aligned in each layer, or sheet, is referred to as the *director*.

2.3 Optical properties

In order to understand the color scattering properties of the liquid crystals used in DPIT/V, it is important to first understand how light interacts with its physical structure. Below, relevant optical properties are reviewed.

Fig. 4 *Left* schematic showing the cholesteric phase, where the molecules are arranged in layers, where within each layer, the molecules are uniaxially aligned parallel to the layer's plane, but in a different direction than the molecules' alignments in adjacent planes. *Right* chemical description of a cholesterol molecule. The components shown in *gray* are out-of-plane with respect to the rest of the molecule, shown in *black* [adapted from Mitchell (2004) and Javitt (2002)]
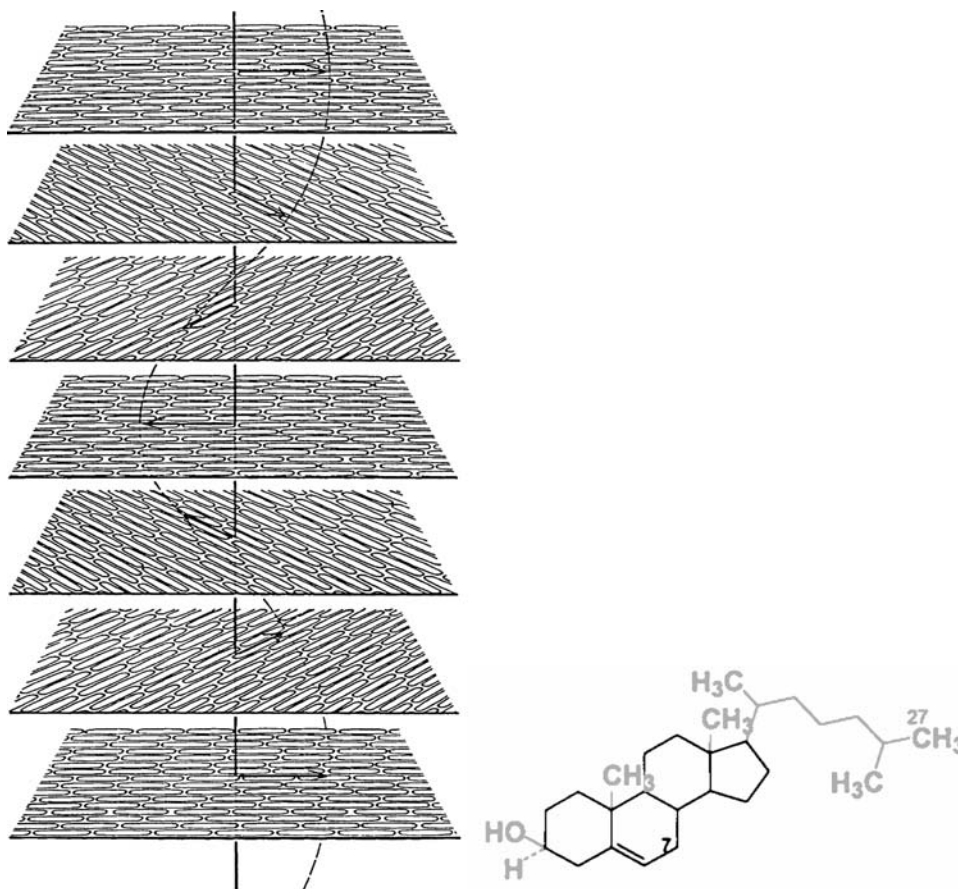
2.3.1 Nematic and smectic phases

Because of the anisotropic structure of these phases, light travels faster in a direction parallel to the layers than in a direction orthogonal to the layers, and these phases are therefore *optically positive*. Consequently, different refraction indices can be defined, where n_o and n_e are the indices for polarizations perpendicular and parallel to the axis of the liquid crystal molecules, respectively. Because of the different refraction indices, these liquid crystals are known to demonstrate strong birefringence (defined as $\Delta n = n_e - n_o$) behavior.

2.3.2 Cholesteric phase

Unlike the nematic and smectic phases, the anisotropy of the cholesteric phase causes light to travel faster in a direction orthogonal to the layers than in a direction parallel to the layers, making it *optically negative*. Likewise, due to their directional molecular arrangement, the anisotropy within each sheet (see Fig. 4) creates two refractive indices: n_c, which is parallel to the direction of the molecules, and n_o, which is orthogonal to the direction of the molecules. In addition, the helical alignment of the liquid crystal molecules within the layers in combination with its anisotropic molecular arrangement causes the CLCs to have interesting optical properties. When illuminated with nonpolarized light, due to their birefringence characteristics and their ability to create a relative phase shift between the resulting polarized orthogonal components, the two orthogonally transmitting polarized components become circularly polarized; one to the right, the other to the left. The component that twists in the same sense as the helix of the liquid crystal completely transmits since it does not see any variation in the refractive index. The other component, however, will experience a sinusoidal variation in the refractive index at every $p/2$ location (see Fig. 5). Therefore, the circularly polarized component of wavelengths of light, initially polarized with their plane of polarization parallel to the director, will be selectively scattered when $\lambda_2 = n_e p$. Likewise, the circularly polarized component of wavelengths of light, initially polarized with their plane of polarization orthogonal to the director, will be selectively scattered when $\lambda_2 = n_o p$ Consequently, when unpolarized white light illuminates CLCs, all wavelengths between λ_1 and λ_2 are reflected, thereby determining a reflection bandwidth

$$\Delta\lambda = p(n_e - n_o) = p\Delta n. \tag{1}$$

All other wavelengths outside of this range are completely transmitted through the liquid crystal. Specifically, first postulated by de Vries (1951), Fergason (1966) proposed an optical model that predicted the structure of the
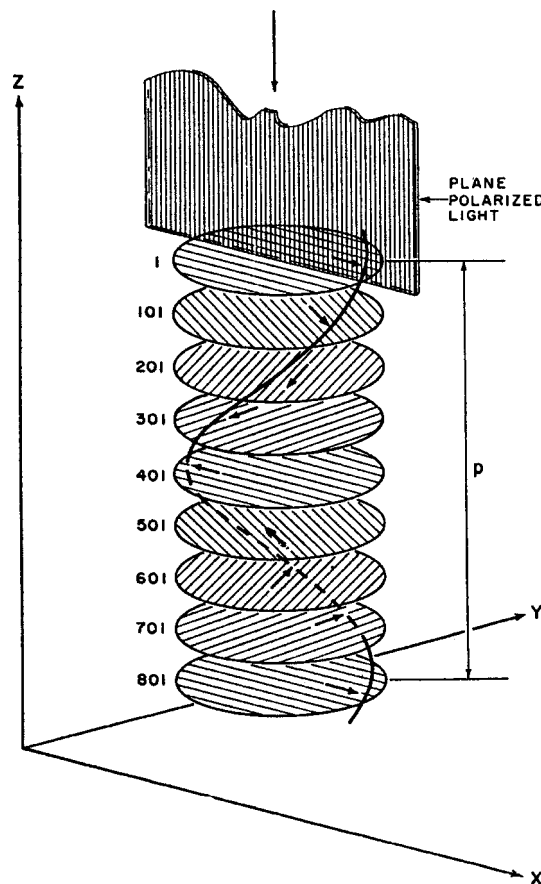
Fig. 5 Model of the cholesteric liquid crystal (*CLC*). The disks marked 1–801 represent molecular layers with the shading indicating the average direction of the long axis of the rod-like molecules. The spacing p between the layers corresponds to the rotation of 360° of the long axes and is called the pitch p (Makow 1991)

CLC necessary for a standing wave to occur. However, since only one of the two circularly polarized components is reflected, the maximum reflectance of this bandwidth is 50%. An example of a typical reflection spectrum is shown in Fig. 6.

Fergason (1966) further observed that the scattered wavelength was a function of both incidence and scatter angle. In his observations, Fergason suggested that the reflections were similar to first-order Bragg scattering. However, McDonnell (1987) points out the inaccuracies of this analogy, citing that first-order reflections occur at normal incidence, and that the dependence of the reflected wavelengths on the incidence angle does not obey Bragg's law. Since CLCs rotate the polarization plane, they are called *optically active*. While crystals such as quartz rotate the polarization plane on the order of 20° (0.056 turns) per millimeter, CLCs typically rotate the polarization plane as much as 18,000°–36,000° (50–100 turns) per millimeter (Fergason 1964).
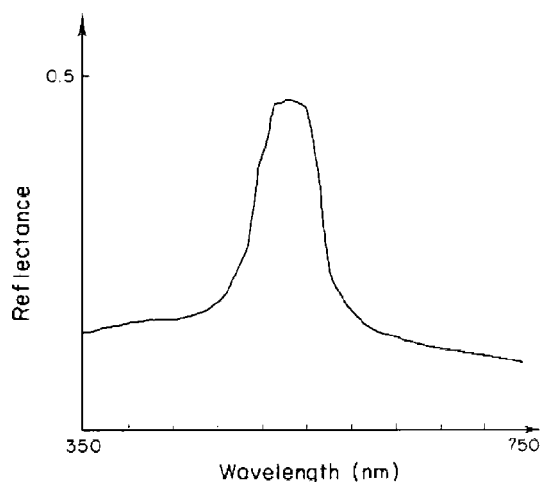
Fig. 6 Typical reflectance spectrum of CLC (McDonnell 1987). Reproduced with permission

While the pitch length determines the reflected wavelength, the pitch length itself varies inversely with temperature.[2] The pitch length can change either by varying the distance between layers, or by changing the rotation angle of the molecules between adjacent layers; the latter being the more dominant effect. Therefore, as the liquid crystal material is cooled from its isotropic phase where its reflection is colorless, rotation between the molecules sets in, thereby transitioning the liquid crystal to its cholesteric phase. When the pitch first corresponds to reflections in the visible spectrum, the liquid crystal will reflect violet. Upon further cooling, the pitch length continues to increase, causing the liquid crystal to reflect blue, green, yellow, orange, and finally red. Further cooling will transition the liquid crystal to its smectic phase, which is also colorless since its pitch length becomes infinite.

Not all CLCs demonstrate such a wide range of reflections or the same response to temperature. Some, for example, will change from red to green, others from green to red, etc. Therefore by mixing various portions of CLCs, it is possible to obtain the desired color play in the desired temperature range. Furthermore, non-cholesteric-based substances have been discovered that also exhibit liquid crystalline behavior. These substances have been termed *chiral nematic,* to distinguish them from the cholesteric-based liquid crystals. Though similar in principle, chiral nematic liquid crystals (CNLC) show improved color play compared with CLCs (Makow 1991). For example, while CLCs are photochemically unstable when illuminated with UV light and chemically unstable in the presence of oxygen (Parsley 1991; Parsley M, LCR/Hallcrest, 1820

Pickwick Lane, Glenview, IL 60026, USA; Scala and Dixon 1969), CNLC are 10–20 times more stable. In addition, while CLCs are natural products where their purity depends on their source, CNLCs can be synthesized to up to 99.9% purity. Furthermore, while CLCs have a more limited range of temperatures that exhibit color reflection, CNLCs can be synthesized to exhibit color reflection as low as −30°C and as high as 150°C, with temperatures ranging from 0.5 to 20°C (Scala and Dixon 1970). To prevent degradation, both CLCs and CNLCs can be microencapsulated in a thin polymer coating made of any combination of gelatin/gum acacia, polyvinyl alcohol, or resorcinol formaldehyde.
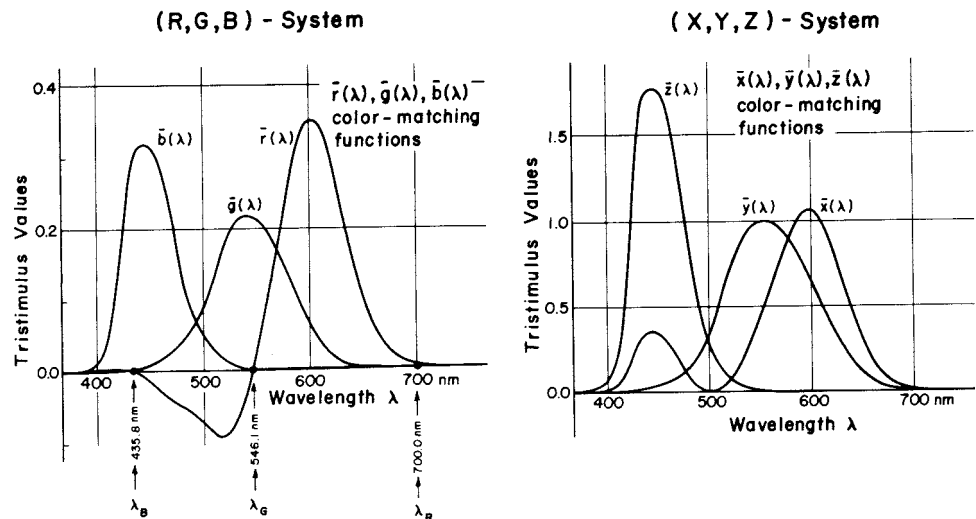
3. Colorimetry

As previously described and shown in Fig. 1 the CNLCs' wavelength reflection is a function of the local temperature that is perceived as colors. Therefore, to derive temperature fields from similar color images requires color measurements, which in turn require a rudimentary understanding of color science. Below, a description of the science of color measurement, or *colorimetry* (P. Hess, Thermochromic liquid crystals, LCR/Hallcrest, 1820 Pickwick Lane, Glenview, IL 60026, USA; Berger-Schunn 1994; Wyszecki and Stiles 1982; Pratt 1991), relevant to understanding DPIT/V, is summarized.

3.1 Color-matching functions

In 1802, Thomas Young (Berns 2000) proposed a trichromatic model color vision model, stating that the eye has three types of sensors, each sensitive over a different band of wavelengths.[3] Maxwell (1855, 1965) found that many colors could also be created by mixing lights from three *primary* colors, orange–red, green, and blue–violet (Young 1802; Rossotti 1983). It was not until the 1920s that such experiments were quantified by Guild (1931) and Wright (1928–1929). For these experiments, one part of a screen

---

[2] High pressure can also cause variations in the pitch length, for example see Keyes et al. (1973), Pollmann and Stegemeyer (1974); however for DLCPT/V applications, the pressure variations have negligible effects on the pitch of CLCs.

[3] Interestingly, experimental evidence of this was found in the late 1950s and early 1960s, where it was determined that the retina within the human eye had two different light-sensitive receptors called rods and cones, loosely named after the shape of the receptors. Rods, being more sensitive to light, are mostly responsible for twilight and night vision. Cones exist in three types, each type being sensitive to a different wavelength band within the visible spectrum, are responsible for day and color vision. Overall, the human retina contains about 6.5 million cones and 100 million rods. Their distribution, however, is not uniform. A small part of the retina called the fovea, for example, contains only cones. When looking at any scene, its center always focuses onto the fovea, which subtends an angle no larger than 4°. Outside of the fovea, there are both rods and cones, with rods outnumbering cones.

was illuminated by a monochromatic wavelength, and the other part was simultaneously illuminated with three different monochromatic wavelengths, or *primaries*, at 700, 546.1 and 435.8 nm. A number of subjects were then asked to vary the intensities of the primaries, until a color match was obtained between the mixed primaries on one part of the screen and the monochromatic wavelength on the other part of the screen. Furthermore, the experiments were setup such that upon observation of the screen, only the subjects fovea would be illuminated, thereby subtending a 2° viewing angle. The results were then adjusted to allow for an equal energy per wavelength spectrum. This resulted in the tristimulus spectral color-matching functions $\bar{r}(\lambda), \bar{g}(\lambda), \bar{b}(\lambda)$, for the standard observer, where "$^-$" indicates an average for the 17 subjects tested (see Fig. 7, left). Power ratios of the primaries in the amount of 72.1:1.4:1.0 were selected such that equal units of their tristimulus values, when mixed, would produce an equal energy per wavelength white. For objects/surfaces emitting light, each of the tristimulus values is an integral function of the spectral power of the light source, P_λ, and the color-matching functions,

$$R = \int P_\lambda \bar{r}(\lambda) \mathrm{d}\lambda \quad G = \int P_\lambda \bar{g}(\lambda) \mathrm{d}\lambda \quad B = \int P_\lambda \bar{b}(\lambda) \mathrm{d}\lambda, \tag{2}$$

and for surfaces reflecting light, the tristimulus values are additionally a function of the spectral reflectance, R_λ,

$$R = \int R_\lambda P_\lambda \bar{r}(\lambda) \mathrm{d}\lambda \quad G = \int R_\lambda P_\lambda \bar{g}(\lambda) \mathrm{d}\lambda$$
$$B = \int R_\lambda P_\lambda \bar{b}(\lambda) \mathrm{d}\lambda. \tag{3}$$

These became known as the Commission International de l'Éclairage (CIE) 1931 standard observer color-

matching functions for the R, G, B system. The negative values in this figure indicate that a match could only be obtained if one of the primaries was added to the single monochromatic wavelength. To avoid such negative values and other practical issues, a new color space was defined that was a transform of the R, G, B color space, known as the X, Y, Z system, with color-matching functions $\bar{x}(\lambda), \bar{y}(\lambda), \bar{z}(\lambda)$(see Fig. 7, right). Similar to the R, G, B color space, the tristimulus values for objects/surfaces emitting light are

$$X = \int P_\lambda \bar{x}(\lambda) \mathrm{d}\lambda \quad Y = \int P_\lambda \bar{y}(\lambda) \mathrm{d}\lambda \quad Z = \int P_\lambda \bar{z}(\lambda) \mathrm{d}\lambda, \tag{4}$$

while for surfaces reflecting light, the tristimulus values are

$$X = \int R_\lambda P_\lambda \bar{x}(\lambda) \mathrm{d}\lambda \quad Y = \int R_\lambda P_\lambda \bar{y}(\lambda) \mathrm{d}\lambda$$
$$Z = \int R_\lambda P_\lambda \bar{z}(\lambda) \mathrm{d}\lambda. \tag{5}$$

Many applications required viewing angles larger than 2°. This meant that an area larger than the fovea would be illuminated within the retina (i.e. stimulating not only cones, but rods as well), necessitating further experiments in order to determine the appropriate color-matching functions. These experiments, performed with a 10° field of view, resulted in similarly shaped profiles that came to be known as the 1964 CIE standard (10°) observer color-matching functions (Wyszecki and Stiles 1982).

3.2 Chromaticity diagrams

If one was interested in the color information independent of its how bright the color appeared to be, then the color's

chromaticities (i.e. *hue* and *saturation*) could be obtained by normalizing its color-matching values by their sum:

$$r = \frac{R}{R+G+B} \qquad x = \frac{X}{X+Y+Z}$$
$$g = \frac{G}{R+G+B} \quad \text{and} \quad y = \frac{Y}{X+Y+Z}, \qquad (6)$$
$$b = \frac{B}{R+G+B} \qquad z = \frac{Z}{X+Y+Z}$$

where

$$r + g + b = 1 \quad \text{and} \quad x + y + z = 1. \qquad (7)$$

Because of Eqs. 7, only two of the three chromaticity values (i.e. *r*, *b* and *x*, *y*) became necessary, thus resulting in the *chromaticity diagrams* (see Fig. 8). The horse-shoe-shaped line is the *spectrum locus* that contains all of the

chromaticities of the visible spectrum wavelengths. The line connecting 380 with 700 nm, the *purple line*, represents various mixtures of these two frequencies, whose color cannot be duplicated by any single monochromatic wavelength. The point *E* shown in Fig. 8 represents a white light that contains an equal energy per wavelength spectrum. The transformation between the two systems is given as

$$\begin{bmatrix} X \\ Y \\ Z \end{bmatrix} = \begin{bmatrix} 0.49 & 0.31 & 0.2 \\ 0.177 & 0.8124 & 0.01063 \\ 0.0 & 0.01 & 0.99 \end{bmatrix} \begin{bmatrix} R \\ G \\ B \end{bmatrix}. \qquad (8)$$

In the CIE 1931 (x, y) chromaticity diagram, the X, Y, Z primaries are at points $(1, 0)$, $(0, 1)$, and $(0, 0)$, respectively.

Fig. 8 The CIE 1931 chromaticity diagrams. *Left* (r, g) diagram (Wyszecki and Stiles 1982) "This material is reproduced with permission of John Wiley & Sons, Inc." *Right* (x, y) diagram
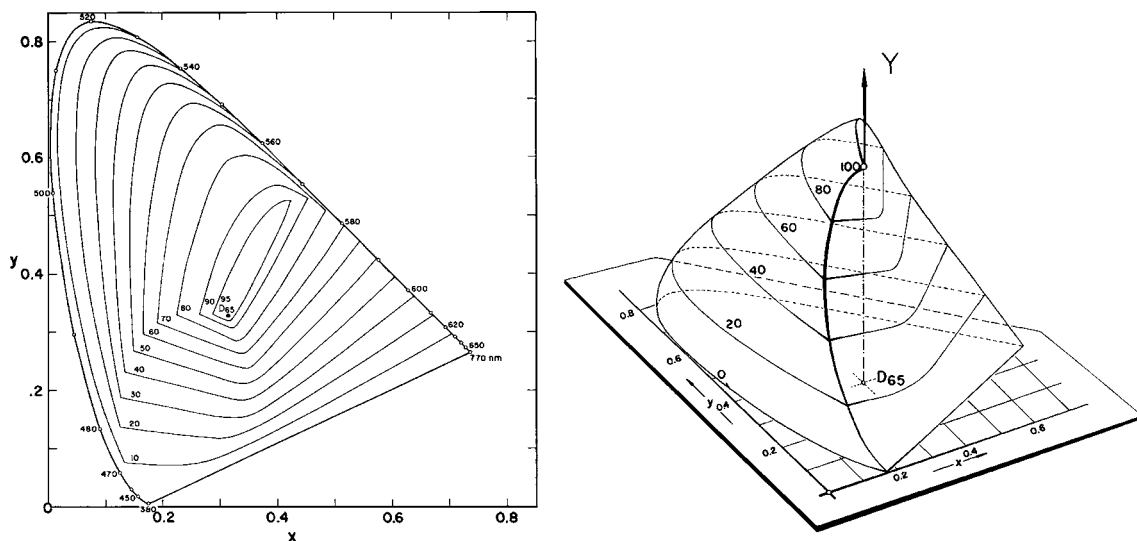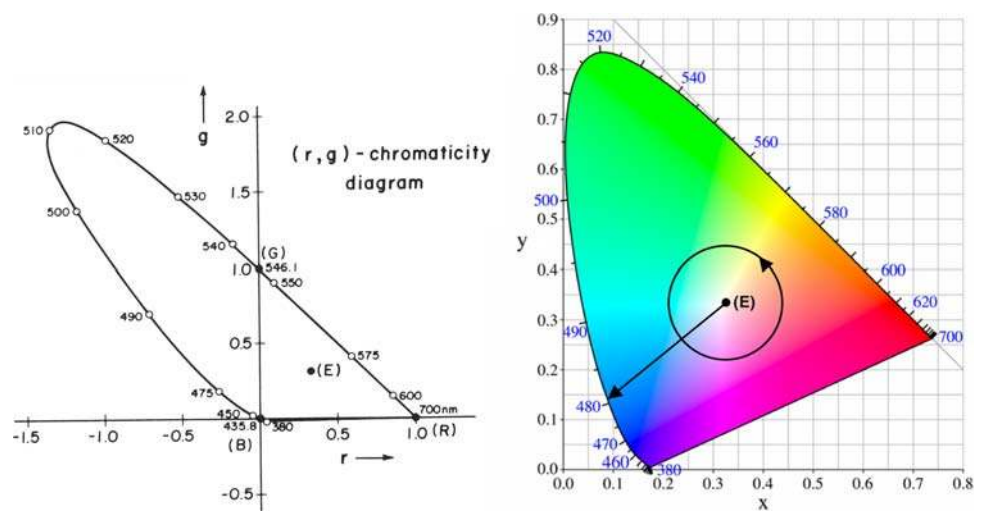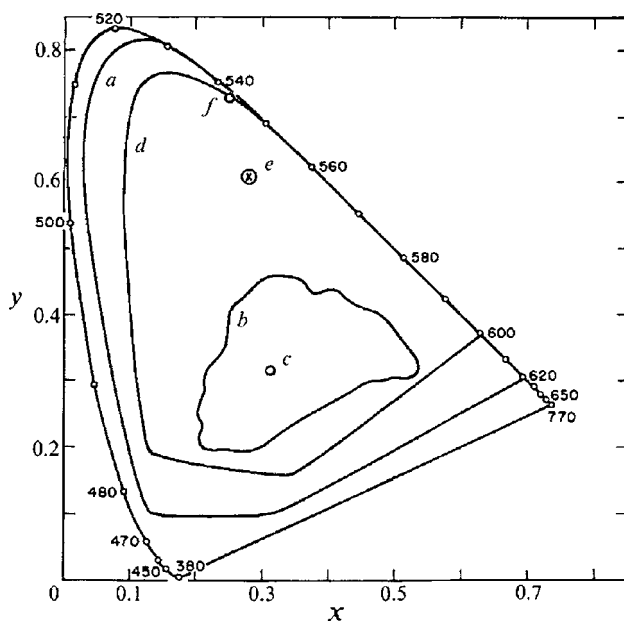

Fig. 9 *Left* chromaticity loci as a function of *Y*, based on the CIE 1931 observer and the CIE standard illuminant D_{65}. *Right* the *Rösch color solid*, an object-color solid of the chromaticity loci as a function of *Y* (Wyszecki and Stiles 1982). "This material is reproduced with permission of John Wiley & Sons, Inc."

All points outside of the spectrum locus and bound by the X, Y, Z primaries are imaginary colors. The CIE diagrams therefore fully describe and characterize all visible colors.

Qualitatively, *hue* is the attribute of color that allows one to distinguish between different colors, for example red, green, etc., hence identifying the dominant wavelength associated with a color. *Saturation* is the attribute of color indicating how much white is mixed with a vivid color, i.e. dominant wavelength, thereby describing its "whiteness". Figure 8 (right) shows the CIE 1931 (x, y) chromaticity diagram in color. From this figure, it can be seen that saturation is the radial distance from the reference white to any pure color (e.g. from 480 nm on the spectrum locus to the white reference, E, and hue is the azimuthal angle around the white reference, in this case, the white reference, E.

Given a color's description in the chromaticity diagram, to obtain total color information, the *luminance factor, Y*, or *intensity*, must also be specified. By definition, the value of $Y = 100$ defines the ideal white color, which emits/reflects 100% of all wavelengths. If this white color contains a spectral radiant power distribution as found in natural daylight, corresponding to a color temperature of 6,500 K, it is referred to as the *CIE standard illuminant* D_{65}. While other CIE standard illuminants can be defined, the CIE standard illuminant D_{65} is the most widely used. In plotting the CIE chromaticity diagram as a three-dimensional plot with Y as the vertical axis (see Fig. 9) one can see that the lighter colors associated with the increasing luminance are more restricted in their range of chromaticities. Black, however, is not well defined, since X, Y, and Z must equal zero, thereby placing its location anywhere on the chromaticity diagram.

While the CIE chromaticity diagrams fully describe and characterize color, specific applications necessitate only a description of a subset of these colors, or *color gamut*. Figure 10, for example, shows several color gamuts, including the large color gamut, curve d, provided by CLCs. Few researchers have used the XYZ color space for characterizing the color play of CNLCs (Akino et al. 1986a; Sun et al. 1997).

3.3 The $R_N G_N B_N$ and HSI color spaces

Since not all applications require a full color description provided by the CIE diagrams, other color spaces have been developed and frequently used to address specific color gamuts or other specific color needs. One such space is the $R_N G_N B_N$ color space, which was designed by the National Television Systems Committee (NTSC) in the United States to define the colors that could be generated with the phosphors used in commercial televisions, and is one of the most frequently used color spaces with image acquisition and recording systems. Its color gamut is shown in Fig. 11. The transformation between the $R_N G_N B_N$ and the *RGB* systems is given as (Pratt 1991)
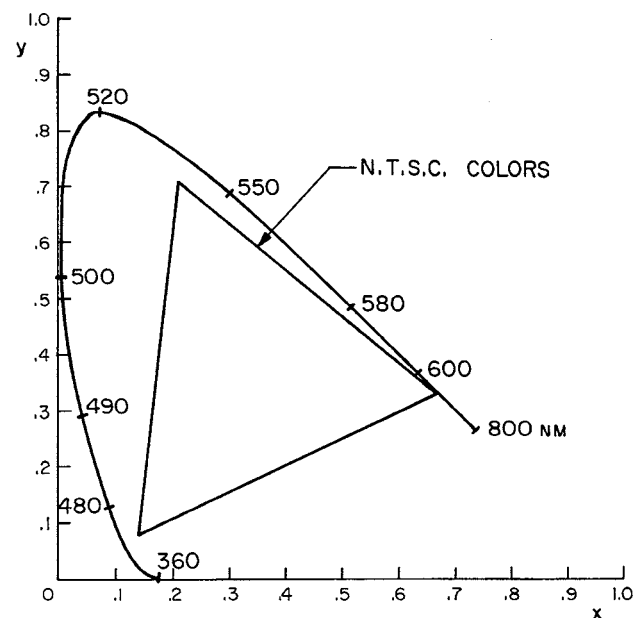

Fig. 10 Chromaticity loci of colors at a luminous reflectance of 0.165 on the basis of the 1931 CIE standard observer and source C illuminant (color temperature of 6,774 K). *a* Optimal colors, *b* Munsell color standards, *c* location of illuminant C, *d* optimum CLC colors. Reprinted by permission from Macmillan Publishers Ltd [Nature] (Makow and Sanders), copyright (1978)

Fig. 11 N.T.S.C. color gamut within the 1931 CIE chromaticity diagram (Pratt 1991)
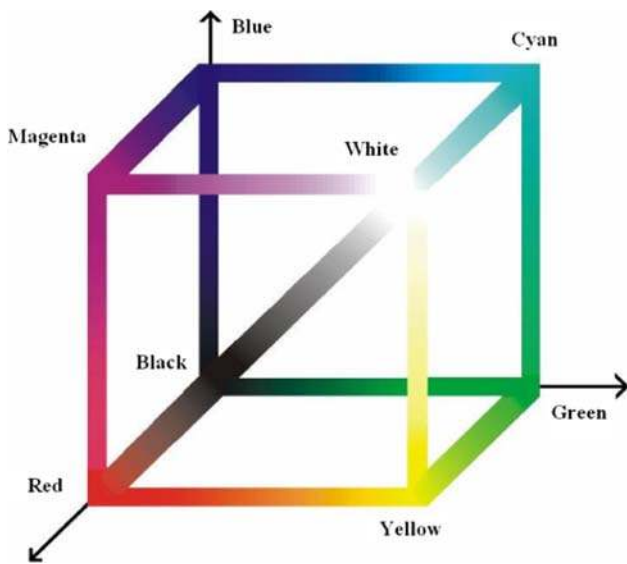
Fig. 12 Graphical representation of the color transformation between the $R_N G_N B_N$ and the *HSI* color spaces

$$\begin{bmatrix} R_N \\ G_N \\ B_N \end{bmatrix} = \begin{bmatrix} 1.167 & -0.146 & -0.151 \\ 0.114 & 0.753 & 0.159 \\ -0.001 & 0.059 & 1.128 \end{bmatrix} \begin{bmatrix} R \\ G \\ B \end{bmatrix}. \quad (9)$$

An alternative perspective on color that is more intuitive to human perception, known as the HSI (Hue, Saturation, Intensity), can also be defined within the $R_N G_N B_N$ color space. For example, an individual is more inclined to describe color as being a particular hue (e.g. red, green, yellow, etc.), either darker or lighter (a reference to the intensity of the color), or faded or more pure in color (a reference to its saturation). Figure 12 shows the graphical transformation between the $R_N G_N B_N$ and the *HSI* color spaces. The Intensity, or Luminance, is the axis that stretches diagonally across the $R_N G_N B_N$ color space, connecting the black coordinate with the white coordinate; the saturation is the radial orthogonal distance from the intensity axis to the color in question; the hue is the azimuthal angle about the intensity axis of the color in question.

Mathematically, the transformation can be done several ways. Pratt (1991), for example, shows a transformation defined as

$$\begin{bmatrix} I \\ V_1 \\ V_2 \end{bmatrix} = \begin{bmatrix} \frac{1}{3} & \frac{1}{3} & \frac{1}{3} \\ \frac{2}{\sqrt{6}} & \frac{-1}{\sqrt{6}} & \frac{-1}{\sqrt{6}} \\ 0 & \frac{1}{\sqrt{6}} & \frac{-1}{\sqrt{6}} \end{bmatrix} \begin{bmatrix} R_N \\ G_N \\ B_N \end{bmatrix} \quad (10a)$$

where

$$H = \arctan\left(\frac{V_2}{V_1}\right) \quad (10b)$$

$$S = \left[(V_1)^2 + (V_2)^2\right]^{1/2};$$

Kimura et al. 1989a) shows a transformation defined as

$$I = R_N + G_N + B_N$$

$$C = \text{chroma} = \sqrt{(r - 1/3)^2 + (g - 1/3)^2 + (b - 1/3)^2}$$

$$H = \begin{cases} \theta & g \geq b \\ 2\pi\theta & g < b \end{cases}$$

$$\theta = \cos^{-1}(2r - g - b)/\sqrt{6C}$$

$$r = R/I; \quad g = G/I; \quad b = B/I \quad (11)$$

Russ (2002) shows a transformation defined as

$$I = (R + G + B)/3$$

$$S = [I - \min(R, G, B)]/I$$

$$H = \begin{cases} \cos^{-1}\left(\frac{(2B - G - R)/2}{\sqrt{(B-G)^2 + (B-R)/(G-R)}}\right) & \text{if} \quad (G \geq R) \\ 2\pi - \cos^{-1}\left(\frac{(2B - G - R)/2}{\sqrt{(B-G)^2 + (B-R)/(G-R)}}\right) & \text{if} \quad (G \leq R) \end{cases} \quad (12)$$

and Hay and Hollingsworth(1996, 1998) defined new chromaticity coordinates

$$x = \sqrt{2/3}(r - g/2 - b/2) \quad y = (g - b)/\sqrt{2}, \quad (13a)$$

such that hue was defined as

$$H = \arctan\left(\frac{y}{x}\right) = \arctan\left(\frac{\sqrt{3}(g - b)}{2r - g - b}\right)$$

$$= \arctan\left(\frac{\sqrt{3}(G - B)}{2R - G - B}\right). \quad (13b)$$

Though not specified by Hay and Hollingsworth (1996), saturation and intensity can be defined as

$$S = \sqrt{x^2 + y^2} = \sqrt{2/3(r^2 + g^2 + b^2) - 1/3(bg + rg + br)}$$

$$I = (R + G + B)/3. \quad (13c)$$

Due to its popularity, the RGB and its associated HSI color spaces has been used extensively for calibrating CNLCs for temperature measurements (Behle et al. 1996; Park et al. 2001; Akino et al. 1986a, 1987, 1989; Dabiri and Gharib 1991a, b, 1995, 1996; Dabiri 1992; Farina et al. 1994; Fujisawa and Funatani 2000; Fujisawa and Hashizume 2001; Fujisawa et al. 2004, 2005; Funatani and Fujisawa 2002; Funatani et al. 2000; Günther and Rudolf von Rohr 2002a; Hay and Hollingsworth 1996, 1998; Hiller and Kowalewski 1986; Hiller et al. 1989a, b, 1991, 1993; Kimura et al. 1989b; Kowalewski and Rebow 1999; Kowalewski 1999, 2001, 2002; Lutjen et al. 2001; Ma et al. 2002, 2003; Mishra et al. 2000; Ozawa et al. 1992; Park and Gharib 2001; Park 1998; Pottebaum and Gharib 2006; Sun et al.1997; Wiberg and Lior 2004). Variations of the HSI color space, such as the HSV and the HLS color spaces have also be defined (Foley et al. 1996),

and used towards CNLC calibration (Anderson and Baughn 2005a, b; Baughn et al. 1999). Lastly, other color spaces, such as the *YIQ*, *UVW*, *U*V*W**, *L*a*b**, and *L*u*v** color spaces, have also been used with CNLC thermometry (Pratt 1991; Wyszecki and Stiles 1982; Hay and Hollingsworth 1996; Jain 1989; Akino et al. 1986a).

4. Description of DPIT/V's experimental components and setup

4.1 General experimental setup

Figure 13 shows schematic layouts for typical experimental setups. The setup shown in Figure 13 (left) allows for simultaneous velocity and temperature measurements within the same plane (configuration A). Conceptually, this DPIT/V setup is similar to those typically used with DPIV. The flow is seeded with microencapsulated CNLC particles, and a cross-section of the flow (typically 2–3 mm thick) is illuminated with either a pulsed (to prevent streaking if the flow is fast moving) or continuous (if the flow is sufficiently slow moving that negligible streaking occurs) white light sheet. Since the sheet needs to be asynchronously pulsed to allow for measurements of velocities, two white light sources and sheet-forming optics can be used, similar to DPIV, where two lasers are used to asynchronously illuminate the flow. The color scattering and motions of the CNLC particles are acquired using a color video camera, typically at 30 frames/s, digitized and stored onto a data acquisition system. Once acquired, the color content of the images, most often the hue variable, is used to extract the temperature field, while the intensity variable is used to extract the velocity field using cross-correlation methods. The setup shown in Fig. 13 (right) allows for surface temperature/heat transfer measurements on a two-dimensional plane that is different from the two-dimensional plane within the bulk of the fluid in which the

PIV measurements are taken (configuration B) (Praisner et al. 2001). In the latter case, for the temperature measurements, the surface of interest is first painted with a thin layer of gloss-black enamel paint (∼15 μm thick), followed by a thin coating of CNLC using an airbrush (∼40 μm thick). The CNLC coating can then be covered with a transparent coating for protection against aging and deterioration of the CNLC. Unlike the former case, this surface is then illuminated with a single white light source. For the velocity measurements, a second plane of interest is simultaneously and synchronously imaged with a PIV system. In the case shown, the PIV imaging plane is orthogonal to the surface from which temperature measurements are made. For both cases, images are acquired with a color video camera and stored onto a data acquisition system.

4.2 Seeding particles

For configuration A, a DPIT/V image is generated from imaging the seeded CNLC particles in the flow field. Ideally, CNLC particles added to the flow should have a controlled range over their size, distribution, and concentration. They should also be small enough to be good flow tracers, yet large enough to scatter sufficient light for imaging (Hjelmfelt and Mockros 1966; Mei 1996; Adrian 1983; Maxey and Riley 1983; Maxey 1987; Auton et al. 1988; Melling 1997; Rangel and Coimbra 1998). Table 1 shows a comparison of CNLC parameters used by various researchers. In addition to the fluid response time, the temperature response time of the CNLC is important in order to ensure accurate temperature measurements. This response time is at present not well established. Ireland and Jones (1987) evaluated the response time of encapsulated CNLCs, 10 μm in diameter, by screen-printing a thin layer of approximately 10 μm onto a flat surface. Then, after generating temperature increases greater than 2,000°C/s, delays between the time where the surface reached the

Fig. 13 *Left* typical layout of DPIT/V system for typical wind or water tunnel applications where temperature and velocity are measured in the same plane. *Right* typical layout of for surface temperature and bulk fluid velocity measurements for typical wind or water tunnel applications where temperature/heat transfer and velocity are measured in different planes (Praisner et al. 2001)
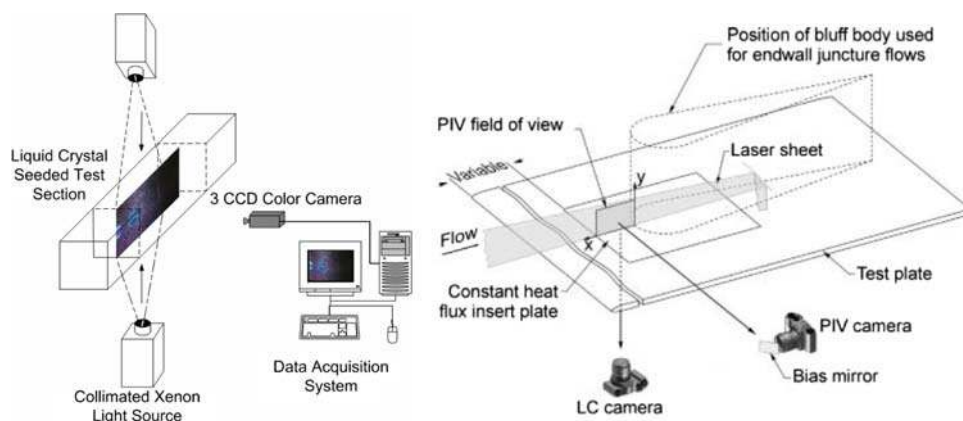
Table 1 Comparison of CNLC parameters, illumination sources and light sheet thicknesses

	Mean diameter (μm)	Temperature response time (ms)	Fluid	Manufacturer	Temperature range (°C)	Particle density (kg/m³)	Illumination source	Light sheet thickness (mm)
Kimura et al. (1989a, b, 1998)	100 20	–	Silicon oil	R-20 Japan Capsular	27.5–29.5 14.9–18.1	–	Halogen lamp	4 7
Hiller et al. (1989a, b), Dabiri and Gharib (1996), Pehl et al. (2000)	10–50	–	Water/glycerol	RW28, TM107, TM317 BDH Chemical Limited	27–30 20–24	–	1 KW Xenon arc flashlamp	Adjustable: 2–10
Dabiri and Gharib (1991a, b, 1996)	150	60	Water/glycerol				Short arc Xenon source	
Ozawa et al. (1992)	10–20	Order of milliseconds	Silicon oil	R-30 Japan Capsular	28–30	–	Halogen lamp	–
Wozniak et al. (1996)	12	50	Silicon oil	TCC1001 BDH Chemical Ltd	26.6–27.7	1,003	–	–
Stasiek (1997)	50–80	–	Glycerol	TM256 BDH Chemical Ltd	30.7–33.3	–	800 W Xenon flashlamp	2–3
Lutjen et al. (2001)	40	40	Glycerol					
Fujisawa and Adrian (1999), Fujisawa and Funatani (2000), Fujisawa et al. (2005)	10	Order of milliseconds	Water	Hallcrest, Inc. R32C2 W R29C4 W	27.7–30	–	4 J/pulse Xenon	2
Fujisawa et al. (2004, 2005)	10	–	Water	Japan Capsular	29.5–35 28–30	1,000–1,020	2 J/pulse Xenon 250 W metal halide lamps	5 3
Park et al. (2001)	40	4	Water	Hallcrest, Inc. BM/R40C26W20	26–29	–	8 J/pulse Xenon flashlamp	2–3
Günther and Rudolf von Rohr (2002a, b)	19.75	1	Water/glycerol	Hallcrest, Inc. BM/R35C20 W	Water: 33.8–35 Glycerol: 34.7–37	1,000–1,020	90 W metal halide (Volpi)	1
Pottebaum and Gharib (2006)	40	4	Water	Hallcrest, Inc. BM/R26C20 W/S33	25.4–27.4	–	Xenon flashlamp	5
Ciofalo et al. (2003)	20–50	–	Glycerol	BN/R20C12 W	18.65–21	–	300 J flashlamp	3.5–6
Mishra et al. (2000) Lutjen et al. (2001)	20–80	4	Water/glycerol	Hallcrest, Inc. BM40/R24C5 W/S-33	24–29	1,000–1,100	1 kW Xenon	0.64–1.14

steady-state color temperature and the occurrence of the color was measured. This delay, the temperature response time of the CNLC thin film, was measured to be approximately 3 ms. Using numerical simulations that consider both the CNLC as well as the encapsulation shell, Kobayashi et al. (1998) have calculated the response time to be as large at 150 ms.

It is also important to know whether the liquid crystals absorb any radiation from the illumination source. Fergason (1966) experimentally determined that no measurable radiation from the illumination source (within $\pm 1\%$) was absorbed in the visible spectrum, thereby negating any uncertainties due to erroneous color reflections.

For proper use, microencapsulated CNLC particles must first be suspended in the desired medium (water, water/glycerol mixture, etc.) for about a day in order to allow for the gel encapsulation to absorb water. In this manner, the index of refraction of the gel encapsulation will better match that of the fluid medium, allowing for purer color transmissions to be observed (Dabiri 1992). An added benefit of using microencapsulated CNLC particles is that they are essentially neutrally buoyant when used in water (see Table 1). Once calibrated, the experiment should be conducted within 6–8 h, since beyond this time, the calibration curve will change (Park et al. 2001). It is also important for the illumination source have a UV filter to prevent any damage to the CNLCs as well as an IR filter to prevent any unnecessary heat absorption within the test facility (see Fig. 14). Beyond UV damage, degradation can occur from microbiological contamination, as the gelatin and gum acacia are an ideal food for micro-organisms. To minimize this contamination, the liquid crystal slurries should be stored in a refrigerator when not used (Parsley, private communications).

4.3 Light source

Since the liquid crystals selectively scatter a temperature-dependent narrow bandwidth of the visible light that is incident upon them, it is most desirable to illuminate them with a light sheet that contains a spectrally uniform energy distribution within the visible spectrum. The white light source that can most closely achieve this requirement is a xenon flashlamp (see Fig. 14), and is therefore recommended as the light source to use to illuminate liquid crystals.

For configuration A, a two flashlamp system can be used to illuminate the flow asynchronously, similar to a DPIV system (see Fig. 13, left). In this manner, both sequentially obtained images provide the velocity field, while either or both of the images can provide the temperature field. A single illumination assembly, however, can be achieved by placing two linear flashlamps inside a cylindrical
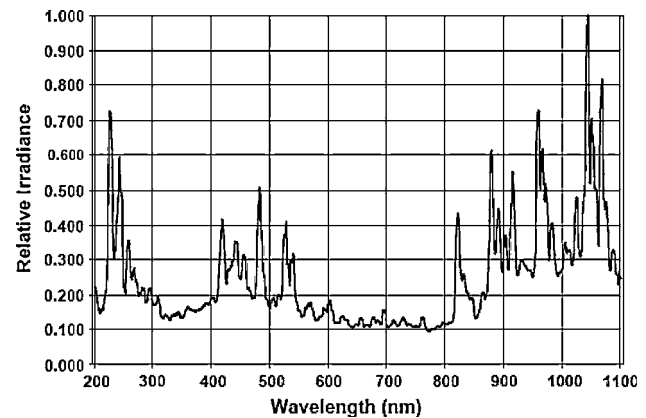
Fig. 14 Typical xenon spectral output illustrates wide spectral distribution. ©2001–2008 PerkinElmer, Inc. All rights reserved. Printed with permission(http://optoelectronics.perkinelmer.com/content/whitepapers/mvs-article.pdf)
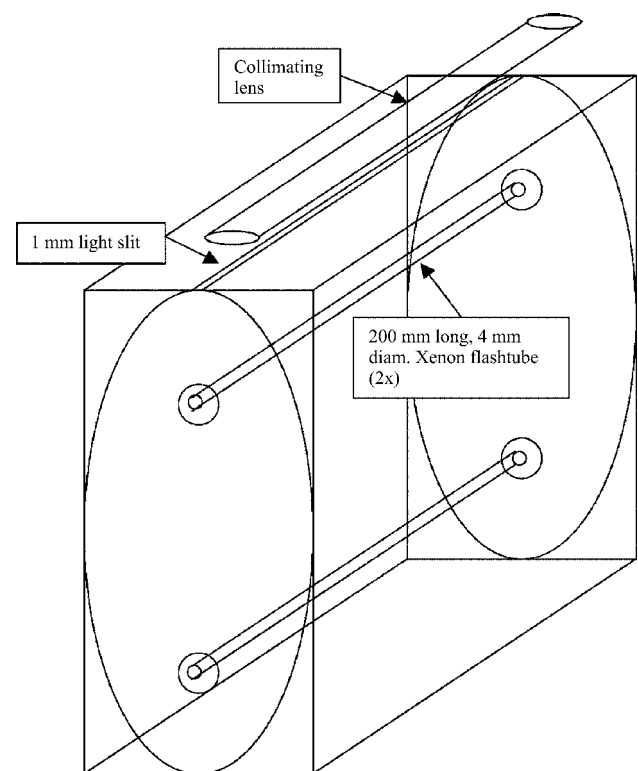
Fig. 15 Elliptical xenon light illumination assembly (Park et al. 2001)

elliptical cavity with a thin slit at one of the ends of its major axis, where each of the flashlamps are placed at each foci as shown in Fig. 15 (Park et al. 2001). The light exiting from the thin slit is then be collimated into thin light sheet with an appropriate lens. In this manner, the elliptical cavity allows for both flashlamps to fire asynchronously while allowing the two light sheets to be

Fig. 16 Timing diagram showing synchronization of DPIV illumination system with the liquid crystal illumination system
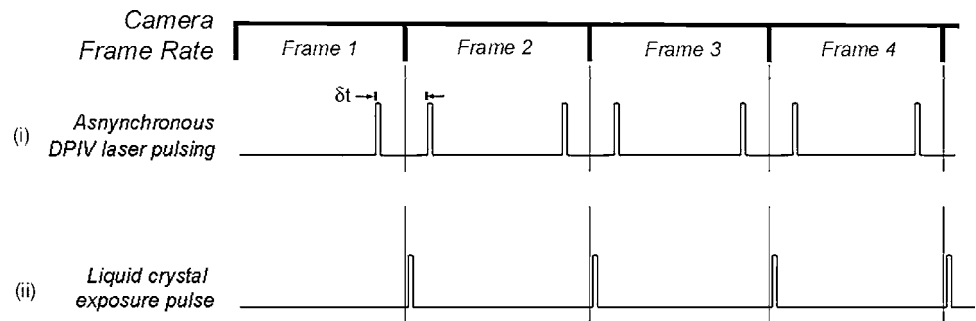
superimposed. Table 1 also shows a comparison of the light sources and the light sheet thicknesses used by various researchers. For configuration B, the illumination systems to obtain the velocity and temperature fields are separate, and must therefore be synchronized. One method that can be used to achieve this synchronization is to place the liquid crystal illumination directly in the middle of the two DPIV exposures, as shown in Fig. 16.

4.4 Image acquisition CCD

While color films can be used for color image acquisition, 3-CCD color video cameras are most often the preferred method of acquiring images, since they will allow for time-evolving flow studies. In general, the 3-CCD color camera is constructed such that a prism splits an incoming image into three optical channels, where each of these channels is coated with an appropriate red, green, and blue spectral filter. Lastly, a CCD is glued at the end of each *R*, *G*, and *B* channel to allow for image acquisition of each of these channels.[4] Also, 3-CCD color video cameras are preferred to the 1-CCD color video cameras that use color stripe filters (such as the Bayer color filter). This is because the former, due to its construction, results in true color values per pixel, while the latter produces color values per pixel due to a spatial averaging algorithm involving the color stripe filters.[5] This spatial averaging algorithm could potentially result in a lower resolution color image. Since the color measurement of the liquid crystals is most important in being able to accurately calibrate temperature, 3-CCD cameras are typically used in studies involving liquid crystal thermometry.

For configuration A (see Sect. 4.1), since the 3-CCD color camera must also provide sequential image pairs that can be processed using cross-correlation DPIV algorithms, the CCDs of the color camera must be interline frame

transfer CCDs in order to allow for image acquisition from asynchronous illumination pulsing (Raffel et al. 1998). For configuration B, this requirement is not necessary, since the DPIV and liquid crystal imaging systems are separate.

5. Temperature calibration and uncertainty analysis

One of the first approaches to quantitatively calibrate liquid crystals sought to identify isothermal lines by selectively identifying narrow color bands. Kasagi et al. (1981), who were interested in studying film-cooling heat transfer, illuminated their liquid crystal coated surface with a monochromatic 589 nm light source to isolate liquid crystal color reflection corresponding to 589 nm. This method was improved by Akino et al. (1986a, 1989), who illuminated their liquid crystal coated surface with a 100 W Tungsten-halogen lamp, and sequentially imaged this surface with a CCD, each time with up to 18 different interferential bandpass filters to identify 18 corresponding isothermal lines. These methods, while useful, did not allow for transient temperature measurements of surfaces or within turbulent flows. Such transient temperature measurements became possible with the development of two other calibration methods. The first and most widely used approach calibrates the temperature changes with the variation of the hue color component, while the second approach calibrates the temperature changes against all three color-defining variables (i.e. HSI, RGB, etc.). In the sections below, each approach is discussed separately. Since both calibration approaches have been used for surface temperatures studies using liquid crystal paint as well as bulk fluid temperature studies using liquid crystals particles, calibration results from both of these types of studies that are relevant to DPIT/V are presented.

5.1 Temperature calibration based on hue

Many researchers have investigated the use of hue for calibrating temperature (Akino et al. 1987; Anderson and Baughn 2005a, b; Grewal et al. 2006; Camci et al. 1992; Dabiri and Gharib 1991a, b, 1995; Farina et al. 1994; Hay

---

and Hollingsworth 1996; Hay and Hollingsworth 1998; Kimura et al. 1989a; Kowalewski 1999, 2001; Lee et al. 2000; Park et al. 2001; Roesgen and Totaro 2002; Sabatino et al. 2000; Sun et al. 1997; Wiberg and Lior 2004). For temperature measurements within fluid flow (see Fig. 13, left), microencapsulated CNLC particles are suspended within the desired fluid flow, and are illuminated by a thin sheet of white light. To eliminate background illumination during data acquisition, the laboratory facility is kept dark such that the only illumination source is due to the white light illumination source.

Typical calibration curves and uncertainty results, shown in Fig. 17 for surface-coated CNLCs, and Fig. 18 for suspended microencapsulated CNLC particles, indicate that both methodologies behave similarly. Here it can be seen that for the lower temperatures, the hue variation is very sensitive to small temperature changes. Conversely, for the larger temperatures, the hue varies rather slowly with temperature. It can also be seen that the uncertainties tend to be smaller for lower temperatures and larger for higher temperatures. Experimental and theoretical research on suspended microencapsulated CNLCs investigating their selective scattering properties has also been reported (Zharkova et al. 1999a, b). As the hue-temperature calibration data shows a highly non-linear behavior, various methods of obtaining curves have been used. Due to ease of use, the linear portion of this behavior has been calibrated

and used (Camci et al. 1992; Moffat 1990). Since this limits the useful temperature range, best fit polynomials have been used to curve fit the calibration data to further extend the useful temperature range (Dabiri and Gharib 1991a, b, 1995; Hay and Hollingsworth, 1998; Hollingsworth et al. 1989). Most recently, neural networks have been used to achieve the calibration curves (Park et al. 2001; Grewal et al. 2006; Lee et al. 2000; Kimura et al. 1998; Fujisawa and Adrian 1999; Yoon and Kim 2002).

While obtaining such calibration and uncertainty curves may seem simple, several experimental setup parameters and data processing methods can affect the accuracy of the measurements. Following Wiberg and Lior's (2004) approach and expanding upon it, each of these parameters and methods are discussed below.

5.1.1 Effect of incident illumination angle and viewing angle

As shown by Fergason (1966), the selectively scattered wavelength is a function of both the incident illumination angle and the viewing angle. While several researchers have documented this effect (Behle et al. 1996; Camci et al. 1992; Günther and Rudolf von Rohr 2002a; Matsuda et al. 2000), Farina et al. (1994) have detailed these effects on the full range of their CNLC calibration curve. Figure 19 (left) shows that the hue-temperature calibration

Fig. 17 *Left* typical hue versus temperature calibration curve. *Right* uncertainty measurements for surface-coated liquid crystals (Sabatino et al. 2000)
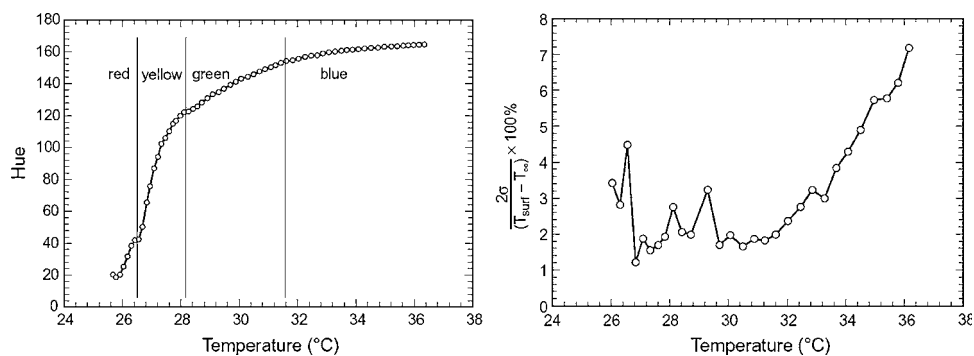
Fig. 18 *Left* typical hue versus temperature calibration curve. *Right* uncertainty measurements for suspended microencapsulated CNLC particles (Park et al. 2001)
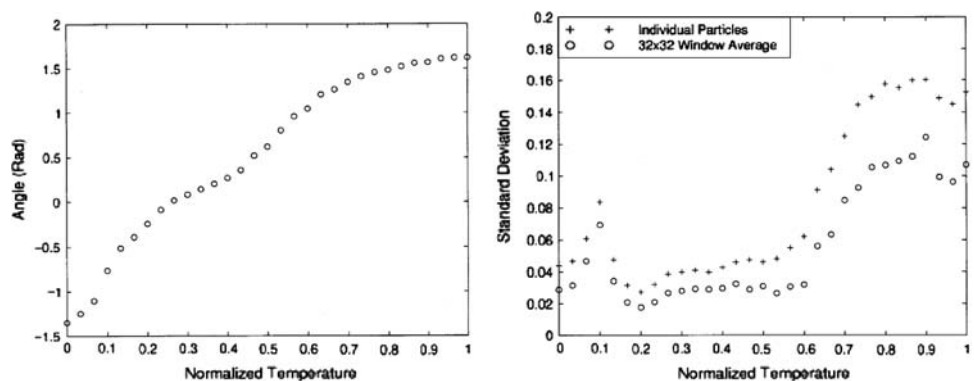
Fig. 19 *Left* off-axis hue-temperature calibration. *Right* on-axis temperature calibration (Farina et al. 1994)
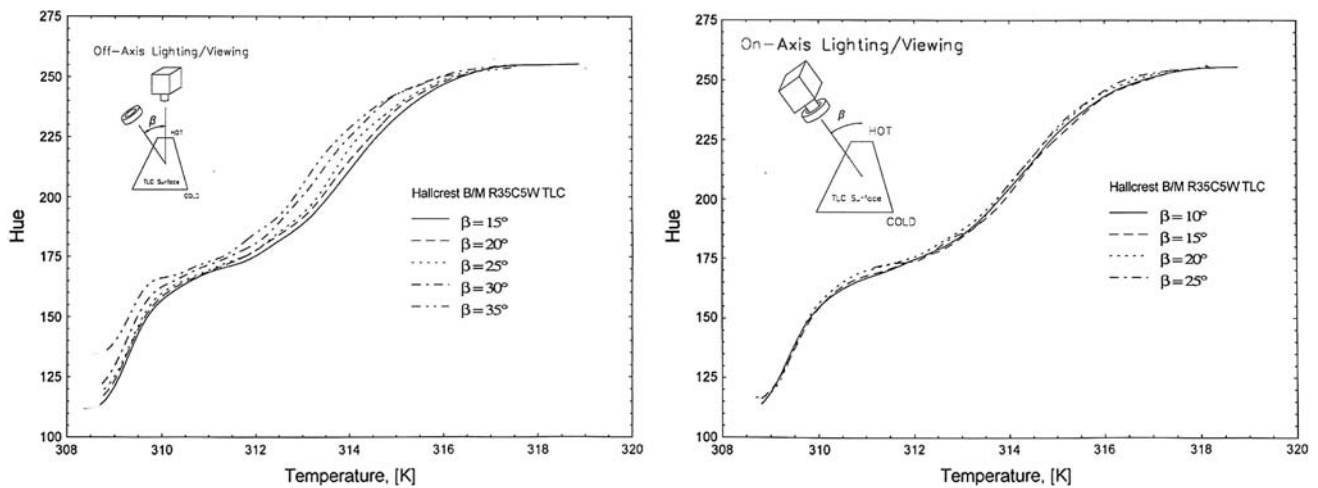
curve varies significantly as a function of the viewing angle, in some areas as much as 0.65°C for a given hue value. Clearly, it is important to maintain the included angle between the incident illumination and viewing angles during both calibration and experimentation. Figure 19 (right) clearly shows that when this included angle is preserved, regardless of what angle the system illuminates and views the area of interest, the calibration curves for different system angles collapse, and at most vary 0.28°C for a given hue value, thereby reducing this type of uncertainty by at least a factor of 2.

5.1.2 Effect of global calibration versus local calibration

Initially, for a given experimental setup with a fixed included incidence/viewing angle, only a single hue-temperature calibration curve, such as those shown in Fig. 19, were used for temperature measurements throughout the fully imaged area. This, however, is not fully accurate, since even for such fixed setups, different areas within the imaged area will be imaged from different viewing angles. Consequently, when using only a single hue-temperature calibration curve, the uncertainty in the temperature measurements will be unnecessarily large. To correct for this, local regions within the imaged area can be defined within which local calibration curves can be defined (Dabiri and Gharib 1991a, b, 1995, Hollingsworth et al. 1989; Funatani et al. 2000). Using this approach, uncertainties have been shown to be reduced by a factor of 2 (Dabiri and Gharib 1991a).

Taking this approach to its extreme, point-wise calibration can be performed to completely eliminate the effect of the viewing angle on the uncertainty of the calibration curve. Using this approach, Sabatino et al.

(2000) generated approximately 185,000 point-wise calibration curves from 60 calibration images. The benefit of this approach is immediately seen when comparing Fig. 20a, which shows the temperature field of a uniform temperature surface using a single-point calibration curve and its resulting artificial temperature variation of ∼2.5°C (the calibrated temperature range is 10°C), with Fig. 20b, which shows a temperature variation of 0.077°C (1.4% of their temperature range) using the point-wise calibration method. Using this approach, the uncertainties ranged from 0.3 to 7.9% of the calibrated temperature range.

In another equally effective approach, Günther and Rudolf von Rohr (2002a) imaged the selective CNLC color scatter over a temperature range of 1.32°C with a telecentric lens to eliminate any angular dependence of these color reflections. With this approach, the uncertainties ranged from negligible values to 6.3% of the calibrated temperature range.

5.1.3 Effect of background light

While the variation of the included angle between the illumination and the viewing angle (Sect. 5.1.1) and the finite viewing angle itself (Sect. 5.1.2) can affect the uncertainty of the calibration curve, background lighting that contaminates the viewing area can also impact the calibration curve. Farina et al. (1994) showed that illuminating the area of interest with various background lighting significantly alters the perceived color reflections of the CNLCs. By plotting the resulting calibration curves for these conditions (see Fig. 21, left), Farina et al. showed that using any such curve for non-identical conditions can result in as much as 2.0°C (∼20%) uncertainties. To

Fig. 20 Temperature fields generated from a liquid crystal image of a constant temperature surface (31.69°C) utilizing **a** a single-point calibration routine and **b** a point-wise calibration routine. A typical single-point calibration curve for this experiment is shown in Fig. 17 (Sabatino et al. 2000)
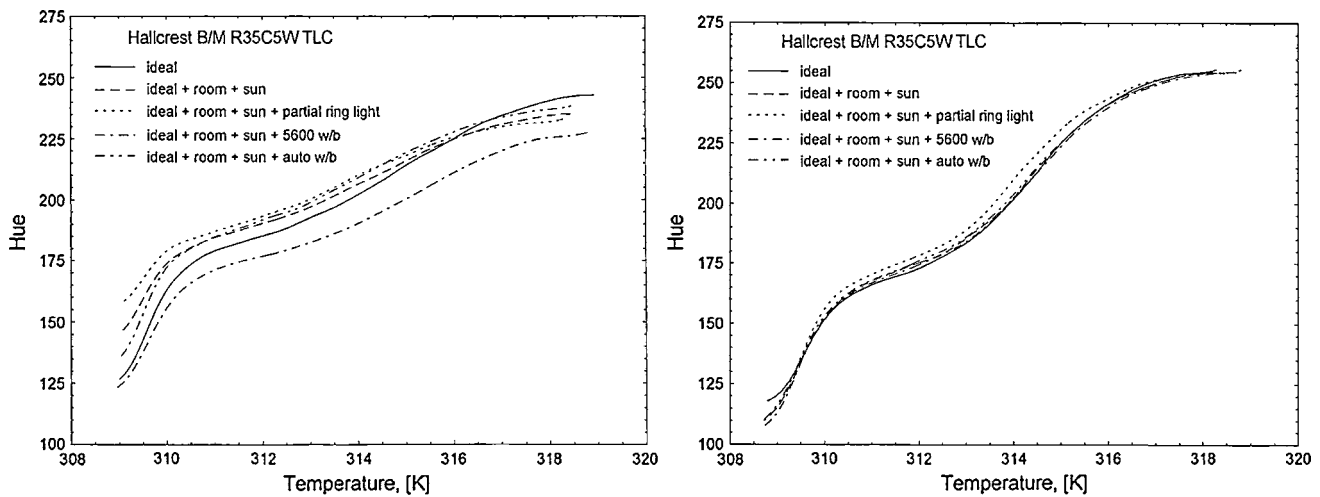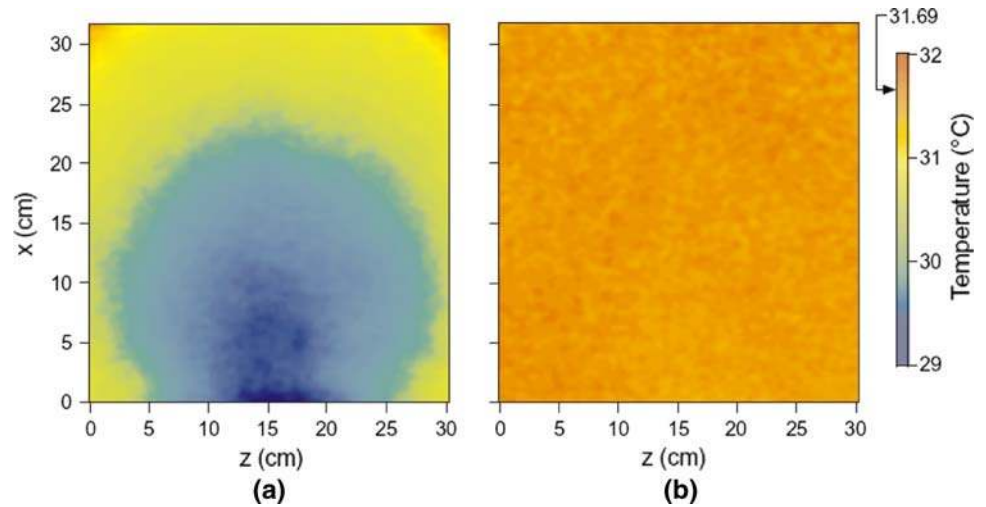
Fig. 21 *Left* hue-temperature calibration under different lighting conditions *without* system color calibration. The maximum error is 2.0°C. *Right* hue-temperature calibration under different lighting conditions *with* system color calibration. The maximum error is ±0.25°C about the mean (Farina et al. 1994)

correct for this, Farina et al. devised a color calibration scheme based on Pratt (1991) that corrects the observed color using the following transformation

$$[r_c] = [A][r_o + b], \tag{14}$$

where r denotes the color vector, the subscripts c and o denote corrected and observed respectively, A is the transformation matrix and b allows for the black offset correction. In implementation, they used 22 of the 24 colors from the MacBeth color chart (the two brightest whites were not used). They first roughly adjusted the white offset using the MacBeth white #21 such that A had approximately equal diagonal elements. They then iteratively adjusted their digitizer black offset until a least-squares solution of the above equation resulted in it being approximately zero. Assuming that this eliminated vector

b, they then solved the above equation for the matrix A. This approach, when combined with the use of cross-polarizers (one at the light source and the other at the camera lens), effectively eliminates any effects of background lighting on the calibration curve (see Fig. 21, right).

Sun et al. (1997) point out that prior to this correction method, the hue origin used to calculate the hue does not result in values that are distributed equally around the origin (see Fig. 22, left). In using this correction method, the resulting hues are more equally distributed about the origin, as shown in Fig. 22 (right). For their experiments, rather than using 22 MacBeth colors, they used Labsphere's red, green and blue colors (referenced to illuminant D_{65}) and two diffuse reflectance plates (with 99 and 2% reflection) to adjust the black-and-white offset of

Fig. 22 *Left* characteristic crystal colors before color correction. *Right* characteristic crystal colors after color correction (Sun et al. 1997)
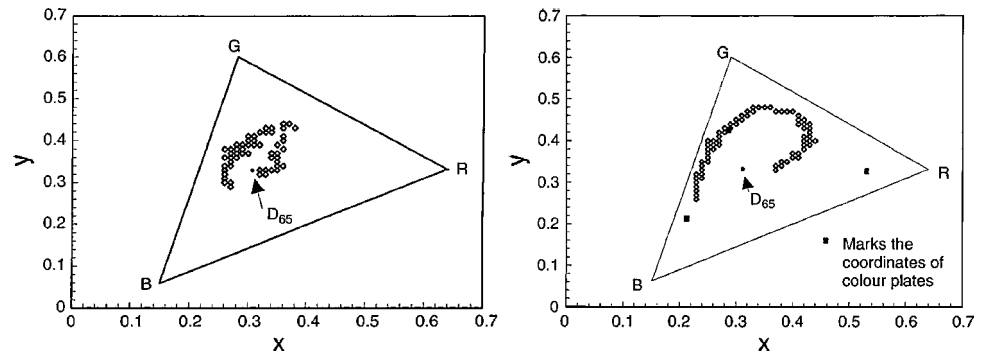
the camera. In addition, the resulting hue values are more saturated, which was found to affect the hue-temperature calibration curve.

5.1.4 Effect of illumination source

The choice of the light source used to illuminate the CNLCs can also affect the perceived color scatter of the CNLCs. Chan (2001) suggests using a Tungsten-Halogen light source as its light does not pulsate due to flicker, its spectral distribution results in good CNLC perceived colors, and its spectral distribution does not deteriorate over time. In a study specifically aimed at determining the effect of different illumination sources, Anderson and Baughn (2005a) showed that the flatter spectrum sources produced the lowest uncertainties and the broadest useful temperature ranges, due to their higher saturation and intensity values. They were also able to show that background subtraction and white balancing methods reduced uncertainties, and collapsed the calibration curves of the various illumination sources, thereby complimenting the results of Farina et al. Anderson and Baughn (2005b) also developed a theoretical model to explain these experimental results. Lastly, Camci et al. (1992), Behle et al. (1996) and Wiberg and Lior (2004) found that variations of the light source intensity produced a 4% change in the hue value, thereby having a relatively minimal effect on the calibration curve.

5.1.5 Effect of CNLC film thickness

Based on light transmittance calculations within CNLCs, Fergason (1968) calculated that a film thickness of 20 μm was sufficient to produce consistent color reflections. Further investigations tested the performance of different film thickness of 14, 23, and 30 μm (Behle et al. 1996); and film thicknesses varying from 9 to 38 μm (Wiberg and Lior 2004). Both of these studies have shown that thinner films result in larger uncertainties in the measurements and thicker films result in smaller uncertainties, and that the calibration curves for thicker films have smaller maximum temperature deviations than thinner films (Behle et al.

1996; Wiberg and Lior 2004). This would suggest that the appropriate CNLC particle diameter should be 20 μm though researchers have also used smaller diameter CNLC particles (see Table 1).

5.1.6 Effect of temperature gradient within CNLC layer

Wiberg and Lior (2004) identify the temperature gradients within the CNLC as a source of error. With temperature gradients within the CNLC, different colors corresponding to these different temperatures can reflect, which when imaged by a camera, will result in an integrated temperature rather than the surface temperature. Though this error is expected to be smaller than other sources of error, they point out that it can be reduced if thermal analyses can be used to correct for these errors.

5.1.7 Effect of digital resolution

The images are most often acquired with a three-chip RGB color camera, where each of the red, green, and blue channels is digitized with an 8-bit digitizer for a total of 24-bits. Regarding uncertainties due to digital resolution, per Behle et al. (1996), the question is: "how is the 24-bit color resolution distributed over the three components hue, saturation, and intensity"? Frey (1988) suggested that the resolution in hue, saturation, and intensity can be given by

$$\mathrm{res}(H, S, I) = \log_2\left(\frac{256}{\Delta(H, S, I)_{\min}}\right) \qquad (15)$$

where $\mathrm{res}(H, S, I)$ is the resolution of H, S, or I in bits, $\Delta(H, S, I)_{\min}$ is the smallest change of H, S, or I for variation of R, G, or B by one binary amplitude, and 256 is the valid range of R, G, B, and H, S, I. Figure 23 shows the implementation of Frey's formulation, clearly showing that the resolution is 8-bits or higher except for the highest temperatures, which correspond to the dark blue reflections. Figure 23 (inset) shows the corresponding uncertainties, which correctly mirror this behavior in that

Fig. 23 Resolution of the hue values and *inset* the relative standard deviations (95% confidence interval) plotted versus temperature (over calibrated temperature range) (Behle et al. 1996)
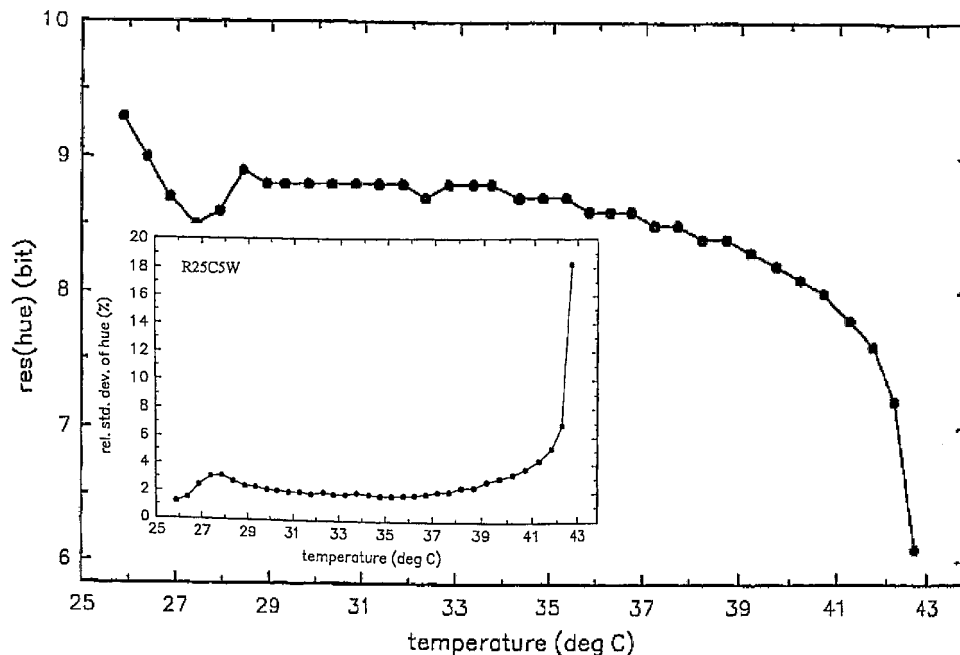
the higher resolution region has low uncertainties while for the lower resolution region, the uncertainties rise quite high. These uncertainties can be reduced further by increasing the digitization resolution (Wiberg and Lior 2004).

5.1.8 Effect of measurement noise

Signal noise can also affect measurement uncertainties. Two approaches have been used to reduce this source of uncertainty: spatial filtering and temporal averaging (Behle et al. 1996; Farina et al. 1994). The spatial filters should be chosen carefully, since their low-pass characteristics will cause smoothing of temperature gradients. Sun et al. (1997), for example, used a Gaussian smoothing kernel that averaged over a 2 mm^2 area. This was justified by observing that the maximum temperature difference across such an area was less than 0.2°C, which was within their measurement accuracy. Temporal averaging assumes that the noise statistics are distributed in time, and have the advantage of not smoothing temperature gradients. Working with CNLC sheets, Behle et al. (1996) show that either spatially averaging with a 5×5 kernel or temporally averaging at least ten isothermal images reduces the hue uncertainty by a factor of ~ 2 (~ 5 to $\sim 10\%$ in the highest temperature that correspond to deep blue reflections and ~ 1 to $\sim 2\%$ elsewhere), and that their combined use reduces the uncertainties by a factor of ~ 4 (see Fig. 24). While spatial averaging may reduce uncertainties for general experimental results, for the specific case of periodic experiments, it may also be possible to reduce uncertainties by temporal phase averaging.
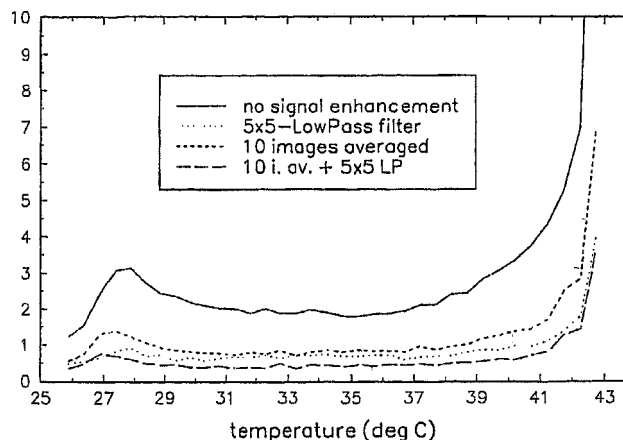
Fig. 24 Noise reduction techniques and their influence on the relative standard deviation of hue over the entire temperature range of a R25C5 W CNLC sheet 9 (Behle et al. 1996)

5.1.9 Effect of hysteresis

While the selective color scatter of CNLCs have been assumed to be repeatable and reversible with respect to heating/cooling, studies have suggested that they exhibit hysteresis (Anderson and Baughn 2005b; Baughn et al. 1999). After studying five different CNLCs with different temperature ranges (narrow-band: manufacturer bandwidth given as 1°C, and broad-band: manufacturer bandwidths given as 5 and 10°C), Anderson and Baughn have shown that the broad-band CNLCs show maximum biases over 20% of their useful calibration ranges, while the two narrow-band CNLCs tested have shown maximum biases of 38 and 62% of their useful calibration ranges. This effect, however,

decreases when the peak temperatures during a heating or cooling cycle decrease. Increasing the temperature sufficiently large beyond the largest temperature of the CNLCs' range, however, causes a permanent decrease in reflectivity, the magnitude of which decreases as the active temperature range increases. It was also found that when the CNLCs were first cooled to below their active range, then calibrated through a heating cycle, the resulting "heating" calibration curves were repeatable. However, when heated to just above their active range and then calibrated through a cooling cycle, the resulting "cooling" calibration curves were not as repeatable. Therefore to avoid uncertainties due to hysteresis, it is recommended that the temperature range experienced by the CNLCs within the experimental facility should be within its active temperature range, and that the CNLC first be '"reset" to below their active temperature range before obtaining a heated calibration curve. This calibration curve can then be used as long as the CNLCs' temperature cycles stay within their active temperature range. Matsuda et al. (2000) have also shown that when operating within the active CNLC temperature range, that hysteresis is negligible.

5.1.10 Effect of CNLC aging

Wiberg and Lior (2004) tested the effect of CNLC aging using a halogen lamp with a built-in UV and IR filter in order to ensure no damage to the CNLC from UV radiation. They held two sample films, 9 and 38 μm, at 55°C, and obtained calibration curves for both after 70 and 275 min. Figure 25 indicates that the thinner film shows at most a
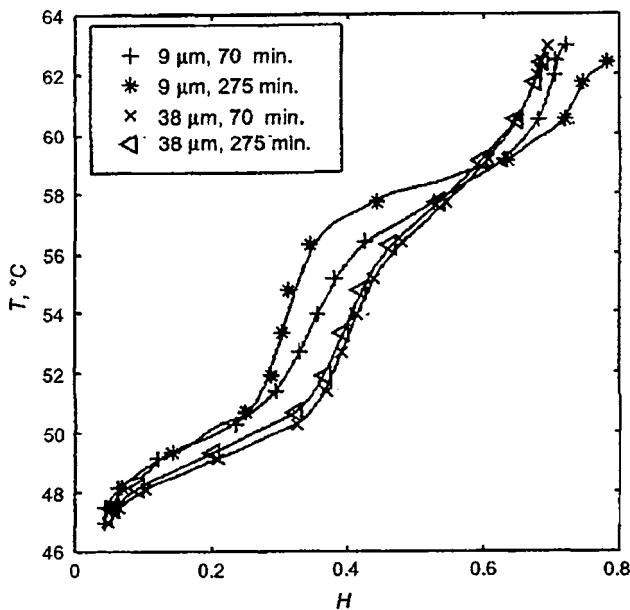

Fig. 25 Temperature–hue relations for the CNLC R45C10, measured after two different aging periods at 55°C, and for two different CNLC layer thicknesses (Wiberg and Lior 2004)

13% variation, while the thicker film shows only a maximum 4% variation. Also, after 275 min, the selective color scatter of the CNLC decreased by 25%.

5.1.11 Effect of hue calculation from color space considerations

The effect of calculating the hue using different color spaces was studied by Hay and Hollingsworth (1996). In this study, the hue was calculated from the *UVW* and *rgb* color spaces, and from an unusual hue definition provided by their Matrox IM-1280 framegrabber (Farina et al. 1994)

$$
\begin{bmatrix} Z_1 \\ Z_2 \\ I \end{bmatrix} = \begin{bmatrix} -0.25 & -0.25 & 0.5 \\ 0.25 & -0.5 & 0.0 \\ 0.33 & -0.33 & 0.33 \end{bmatrix} \begin{bmatrix} R_N \\ G_N \\ B_N \end{bmatrix}, \tag{16a}
$$

where

$$
H = \arctan(Z_2/Z_1). \tag{16b}
$$

They found that the hue values based on the *UVW* and *rgb* color spaces resulted in larger hue ranges, with uncertainties slightly larger than those resulting from the hue defined by Matrox. Though the lower uncertainties due to the Matrox definition may seem advantageous, Hay and Hollingsworth (1996) point out that the resulting relative error due to the *UVW* and *rgb* color spaces was lower and therefore preferable.

5.1.12 Uncertainty analysis

For polynomial curve fits to hue-temperature calibration curves, Hay and Hollingsworth (1996, 1998) show that the uncertainty is

$$
\delta T = \left[\left(\frac{\mathrm{d}T}{\mathrm{d}h} \delta h \right)^2 + (2\mathrm{SEE})^2 \right]^{1/2}, \tag{17a}
$$

where $\mathrm{d}T/\mathrm{d}h$ is the slope of the curve fit, the standard estimate of error (SEE) is

$$
\mathrm{SEE} = \left[\frac{\sum_{i=1}^{k} \left[T_i(h) - T_{fit,i}(h) \right]^2}{k - j - 1} \right], \tag{17b}
$$

k is the number of data points, and j is the order of the curve fit. They have also defined a non-dimensional temperature, and used it to develop non-dimensional calibration curves, which allows for different calibration curves to collapse, though at the expense of a $\sim 4\%$ increase in the measurement uncertainties.

5.2 Multi-variable temperature calibration

If one component of color can be satisfactorily calibrated to temperature, the question arises as to whether calibrating
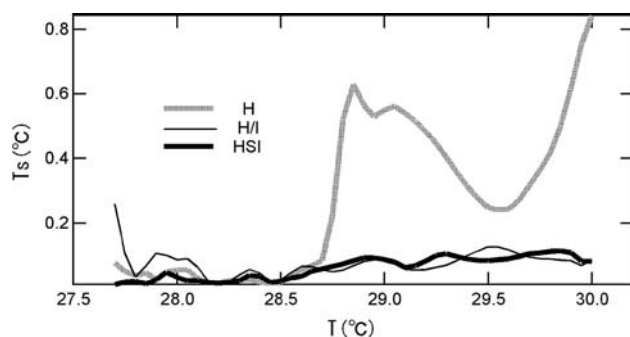
Fig. 26 Evaluation of temperature errors for various calibration techniques. The hue-temperature calibration curve shows a maximum/average relative uncertainty of 35.6/11.7%, the hue/saturation-temperature calibration *curve* shows a maximum/average relative uncertainty of 6.5/3.5%, and the hue/saturation/intensity-temperature calibration curve shows a maximum/average relative uncertainty of 6.5/2.6% with respect to the active CNLC temperature range (Fujisawa and Hashizume 2001)

temperature to two or more color variables will provide better accuracy. Fujisawa and Hashizume (2001) and Funatani et al. (2000) have investigated calibrating temperature against hue, hue and saturation, and hue, saturation and intensity. Numerical simulations generated artificial temperature fields of Rayleigh–Benard flow (Rayleigh number was 1.06×10^6), and experimental results were used to reproduce experimental conditions in these temperature fields. Figure 26 shows the increase in accuracy achieved by multi-variable temperature calibration. Figure 27 shows the same temperature fields resulting from the use of the three different calibration curves, clearly showing the benefits of using a multi-variable calibration curve within the HSI color space. Other such studies have yielded similar results (Fujisawa and Adrian 1999; Fujisawa and Funatani 2000; Fujisawa et al. 2005; Vejrazka and Marty 2007).

Multi-variable calibration curves within the *rgb* color space have also been studied by Matsuda et al. (2000) and Park et al. (2001) Unlike the previous results, Park et al. (2001) found that their *rgb*-temperature calibration curve produced larger uncertainties than their hue-temperature calibration curve. They attributed this to the fact that the training vectors to their neural network represented only a narrow set of input values, which when combined with the large uncertainties in their individual *r*-, *g*-, *b*-temperature curves, produced larger uncertainties.

Realizing the dependence of the temperature on the tri-color values, Roesgen and Totaro (2002) have suggested an alternative coordinate transform to decorrelate the data. To measure the degree of correlation, a covariance matrix is defined as

$$
\begin{aligned}
\underline{\underline{C}} &= \mathrm{Cov}(r, g, b) \\
&= \begin{bmatrix}
\overline{(r - \bar{r})^2} & \overline{(r - \bar{r})(g - \bar{g})} & \overline{(r - \bar{r})(b - \bar{b})} \\
\overline{(r - \bar{r})(g - \bar{g})} & \overline{(g - \bar{g})^2} & \overline{(g - \bar{g})(b - \bar{b})} \\
\overline{(r - \bar{r})(b - \bar{b})} & \overline{(g - \bar{g})(b - \bar{b})} & \overline{(b - \bar{b})^2}
\end{bmatrix}.
\end{aligned}
\tag{18}
$$

The linear transformation

$$
\begin{bmatrix} x_1 \\ x_2 \\ x_3 \end{bmatrix} = \underline{\underline{T}} \begin{bmatrix} r - \bar{r} \\ g - \bar{g} \\ b - \bar{b} \end{bmatrix}.
\tag{19}
$$

can be applied to transform the data into a decorrelated domain. The matrix T is determined such that the new covariance matrix should be diagonal, leading to an eigenvalue problem

$$
\underline{\underline{C}}\vec{t} = \lambda \vec{t},
\tag{20}
$$

where the matrix C is the old covariance matrix. Solving the above equation results in three real eigenvalues ($\lambda_1 > \lambda_2 > \lambda_3$) that form the matrix T. Applying this to
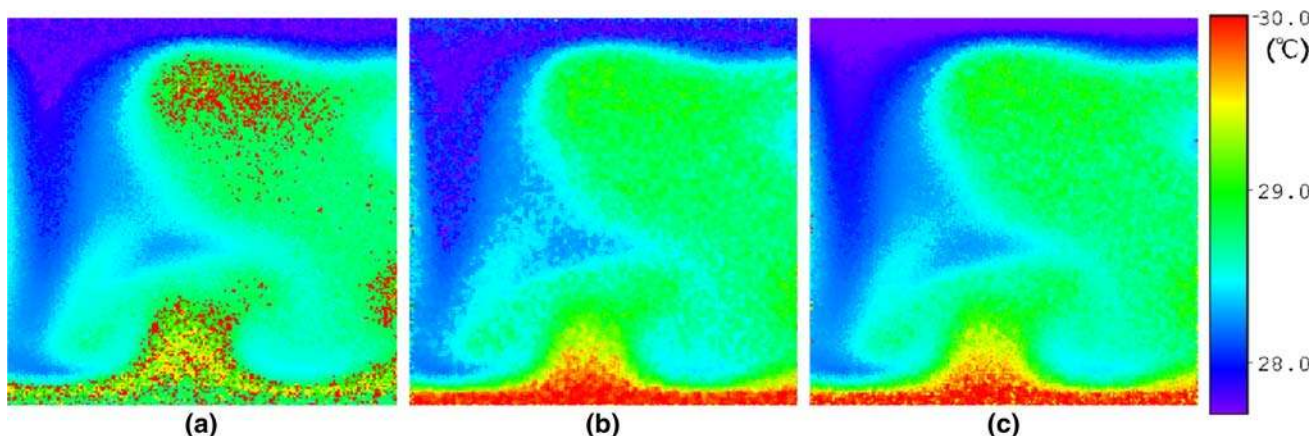
Fig. 27 Temperature distributions reconstructed by various calibration techniques: **a** *H*, **b** *H/I* and **c** *H–S–I* (Fujisawa and Hashizume 2001)

data from Park et al., the original *rgb* and *HSI* covariance matrices,

$$\text{Cov}(r,g,b) = 10^{-4} \times \begin{bmatrix} 65.1755 & 10.2678 & -75.4434 \\ 10.2678 & 33.5754 & -43.8433 \\ -75.4434 & -43.8433 & 119.2866 \end{bmatrix}$$

$$\text{Cov}(H,S,I) = 10^{-4} \times \begin{bmatrix} 220.4466 & -6.0049 & 0 \\ -6.0049 & 8.1037 & 0 \\ 0 & 0 & 0 \end{bmatrix} \quad (21)$$

after transformation become

$$\text{Cov}(r,g,b) = \begin{bmatrix} 0.0184 & 0 & 0 \\ 0 & 0.0034 & 0 \\ 0 & 0 & 0 \end{bmatrix}$$

$$\text{Cov}(H,S,I) = \begin{bmatrix} 0.0221 & 0 & 0 \\ 0 & 0.0008 & 0 \\ 0 & 0 & 0 \end{bmatrix}. \quad (22)$$

Note that the original covariance matrix for the HSI color space shows that the data is only weakly correlated, which might indicate why the hue-temperature calibrations and the multi-variable calibrations in the HSI color space work well.

6. Three-dimensional methods

While quite a bit of effort has gone into developing DPIT/V, its extension towards three-dimensional measurement methods has been underdeveloped. To date, two approaches have been taken. First, two-dimensional temperature fields obtained from scanning methods are used to construct three-dimensional temperature fields (Fujisawa and Funatani 2000; Fujisawa et al. 2005; Mishra et al. 2000; Lutjen et al. 2001). Second, stereo-DPIV has been combined with DPIT/V to provide stereo-liquid crystal thermometry/velocimetry (stereo-DPIT/V) (Funatani and Fujisawa 2002; Fujisawa et al. 2005).

6.1 Scanning methods

The experimental setup for the three-dimensional scanning DPIT method can be set up in several ways. Fujisawa and Funatani (2000), for example, have devised a system whereby two separate and parallel strobe lights illuminate cross-sections of their flow (see Fig. 28). The strobe lights are mounted onto a translation stage, which is synchronized with the data acquisition system. The translation speed is coordinated with the strobe lights' pulsing such that their sequential pulsing simultaneously provides the time difference for velocity calculations while illuminating the
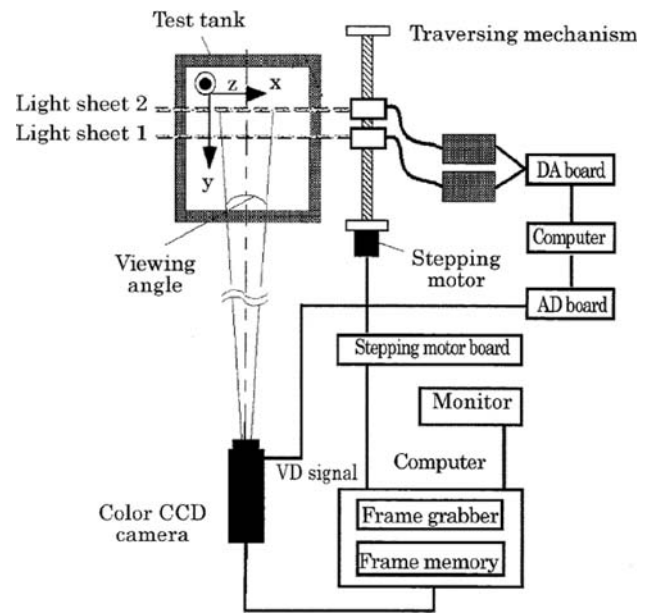

Fig. 28 Experimental apparatus and imaging system (Fujisawa and Funatani 2000)

same cross-section of the flow. Once images are acquired, the temperature fields were extracted using an HSI-temperature calibration curve (Fujisawa and Hashizume 2001), which were then used to reconstruct three-dimensional temperature fields. Uncertainties within a 95% confidence level are shown to be within 5%.

In another implementation, one translation stage contains a mirror that reflects the light sheet into the area of interest, and another translation stage contains the imaging camera. Both translation stages are synchronized to allow for the acquired images to remain in focus as shown in Fig. 29 (Mishra et al. 2000; Lutjen et al. 2001). Once images are acquired, a hue-temperature calibration curve is used to extract two-dimensional temperature fields, which are then used to reconstruct three-dimensional temperature
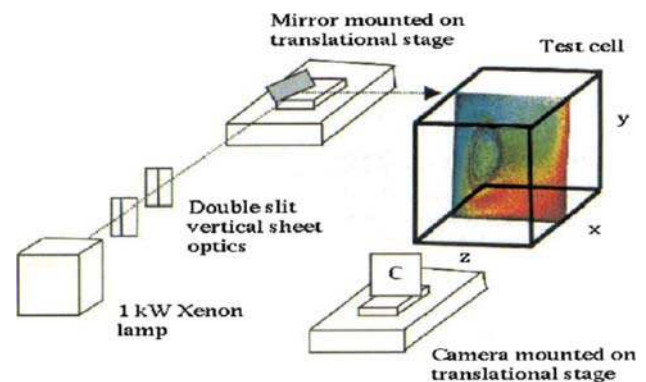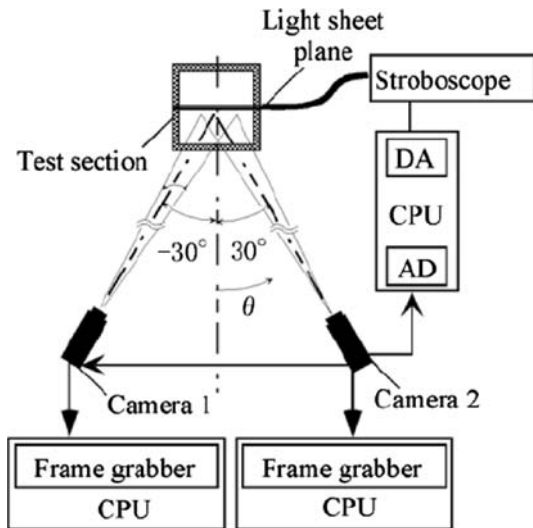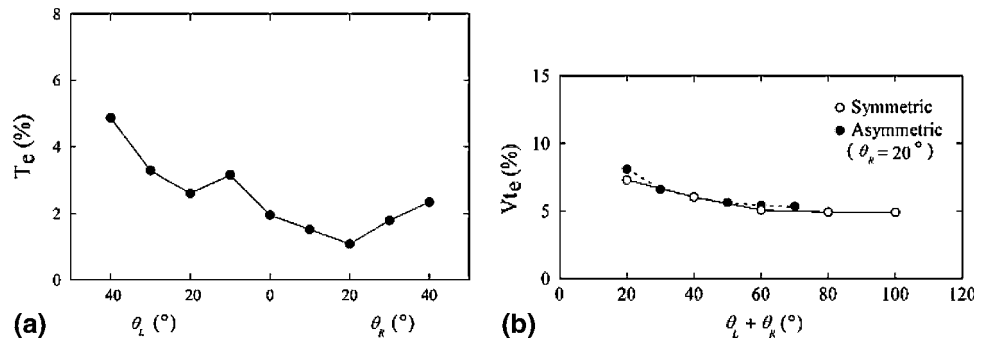

Fig. 29 Experimental apparatus and imaging system (Mishra et al. 2000, Taylor & Franci Ltd, http://www.informaworld.com)

fields using tomographic techniques. Simulations show that uncertainties of noiseless high-resolution reconstruction results are 1.5%, while uncertainties of low-resolution reconstruction results with 5% RMS noise are 4.97%.
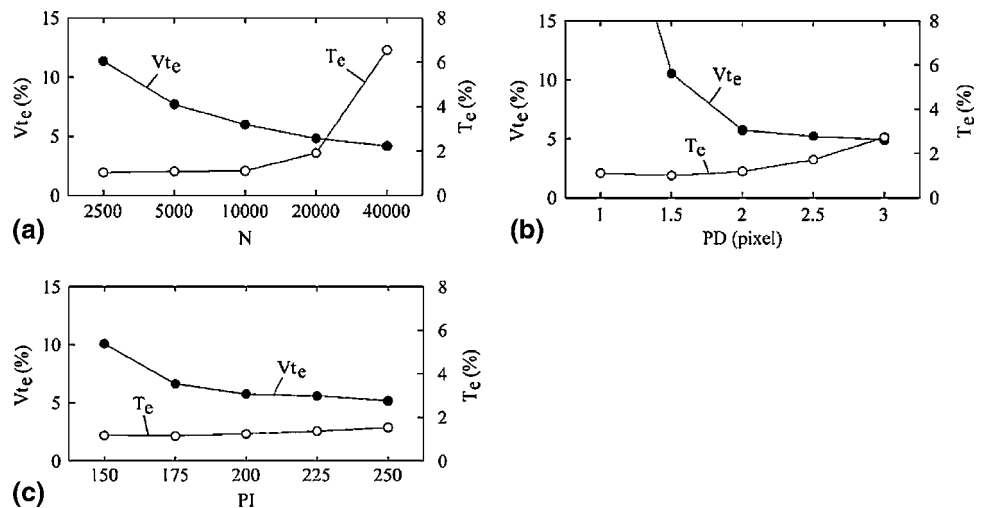

Fig. 30 Stereo-DPIT/V system setup (Funatani and Fujisawa 2002)

6.2 Stereoscopic methods

Funatani and Fujisawa (2002) have been able to successfully combine stereo-DPIV with DPIT/V. They have achieved this by arranging two color cameras with an angular displacement configuration, though without enforcing the Scheimpflug condition (Prasad 2000). Light sheets were generated from stroboscopes, which were used to illuminate the desired cross-section of the flow that was filled with CNLCs (see Fig. 30). To allow for acquisition of both velocity and temperature, the flow was seeded with both CNLCs and PIV particles (nylon spheres). First, grids are used to determine the mapping function between the image plane and the 3D physical space for both cameras. Then both calibration and experimental data are acquired. The calibration data, after conversion to the HSI domain, is used to create a multi-variable calibration curve (Fujisawa and Hashizume 2001; Funatani et al. 2000), which is then used to generate planar temperature fields. For measuring the velocity, the intensity field of camera 2 is used with the intensity field of camera 1 to generate three-component velocities within a plane using the method proposed by Soloff et al. (1997).

Further error analysis of this approach using artificial stereo-color images show interesting results (Fujisawa

Fig. 31 *Left* temperature uncertainty versus viewing angles of camera (10,000 particles, 2 pixel particle diameter, 200 peak intensity). *Right* velocity uncertainty versus viewing angle of camera. **a** Symmetrical arrangement; **b** asymmetrical arrangement ($\theta_R = 20°$) (Fujisawa et al. 2004)

Fig. 32 Uncertainties of temperature and velocity measurements **a** number of tracer particles N (PD = 2 pixels, PI = 200), **b** PD of tracers ($N = 10,000$, PI = 200), **c** peak tracer intensity PI ($N = 10,000$, PD = 2 pixels) (Fujisawa et al. 2004)

Table 2 References for measurements of surface temperature and heat transfer rates categorized for fluid flows

Applications	References	Temperature ranges (°C) or shear stress (N/m²)	Characteristic fluid velocity	Characteristic length scale	Liquid crystal thickness
General, review, and techniques papers	Woodmansee ([1966](#), [1968](#)), Cooper et al. ([1975](#)), Camci and Kim ([1992](#)), Ogden and Hendricks ([1984](#)), Platzer et al.([1992](#)), Baughn ([1995](#)), Ireland et al. ([1999](#)), Ireland and Jones ([2000](#)), Saniei ([2002](#)), Mikhailov ([2003](#)), Ling et al. ([2004](#)), Grassi et al. ([2007](#)), Kodzwa and Eaton ([2007](#)), Wagner and Stephan ([2007](#))	N/A	N/A	N/A	N/A
Aerodynamic and hypersonic flows	Klein ([1968a, b](#)), Lemburg ([1971](#)), Ardasheva and Ryzhkova ([1978](#)), Holmes and Obara ([1987](#)), Schöler ([1990](#)), Reda and Aeschliman ([1992](#)), Babinsky and Edwards ([1996](#)), Roberts and East ([1996](#))	Starting temperatures range from −30 to 75°C Temperature width between 1 and 16°C	0.805–5.07 Ma	50 mm	10–20 μm
Impinging cooling	Metzger et al. ([1991](#)), Kim and Camci ([1995a, b](#)), Yan and Saniei ([1996](#), [1997](#)); Ashforth-Frost and Jambunathan ([1996a, b](#)); Ashforth-Frost et al. ([1997](#)), Huang et al. ([1998](#)), Ekkad et al. ([1999](#)), Lee and Lee ([1999](#), [2000](#)), Azad et al. ([2000](#)), Arjocu and Liburdy ([2000](#)), Saniei and Yan ([2000](#)), Hwang and Cheng ([2001](#)), Kaiser ([2001](#)), Dano et al. ([2005](#)), El-Gabry and Kaminski ([2005](#)), Geers et al. ([2006](#)), Facchini and Surace ([2006](#)), Chan et al. ([2001](#)), Dukle and Hollingsworth ([1996a, b](#))	Starting temperatures range from 25 to 45°C Temperature width between 0.5 and 7°C	0.6–43.2 m/s	0.635–12.5 cm	15–100 μm
Duct flows with various wall conditions	Baughn et al. ([1989](#)), Zhang et al. ([1995](#)), Sillekens et al. ([1998](#)), Meinders et al. ([1998](#)), Kukreja and Lau ([1998](#)), Chyu et al. ([1999](#)), Hwang and Cheng ([1999](#)), Hwang and Lui ([1999](#)), Liou et al. ([2000a, b](#)), Ekkad et al. ([2000](#)), Liou et al. ([2001](#)), Gao and Sundén ([2001](#)); Cavallero and Tanda ([2002](#)), Wierzbowski and Stasiek ([2002](#)), Liou et al. ([2003](#)), Tariq et al. ([2003](#)), Moon et al. ([2003](#)), Jeng et al. ([2004](#)), Wang and Sundén ([2004](#)), Tanda ([2004](#)), Tariq et al. ([2004](#)), Uzol and Camci ([2005](#)), Ahn et al. ([2005](#)), Facchini et al. ([2006](#))	Starting temperature range from 27.7 to 47°C Temperature width between 1 and 38°C	0.6–150 m/s	0.3–25 cm	0.15 mm
Internal combustion engines	Neely et al. ([1997](#)), Maier et al. ([2000a, b](#)), Son et al. ([2001](#))	Starting temperatures range from 25 to 30°C Temperature width between 1 and 7.5°C	0.1–83.3 m/s	12.39–20 cm	
Turbine blades and film-cooling	Kasagi et al. ([1981](#)), Martinez-Botas et al. ([1995](#)), Spencer et al. ([1996](#)), Hoffs et al. ([1997](#)), Ekkad et al. ([1997](#), [1999](#)), Du et al. ([1997](#), [1999](#)), Ekkad et al. ([1998](#)), Kukreja and Lau ([1998](#)), Drost and Bolcs ([1999](#)), Ekkad et al. ([1999](#)), Hwang and Cheng ([1999](#)), Ekkad and Han ([1999](#), [2000a, b](#)), Ekkad et al. ([2000](#)), Teng et al. ([2000](#)), Hwang and Chang ([2000](#)), Jung and Lee ([2000](#)), Azad et al. ([2000a, b](#)), Ai et al. ([2001](#)), Chen et al. ([2001](#)), Engels et al. ([2001](#)), Lee et al. ([2002](#)), Mayhew et al. ([2003](#)), Ahn et al. ([2003](#)), Lock et al. ([2005a, b](#)) Yuen and Martinez-Botas ([2005](#)), Sargison et al. ([2005](#)), Newton et al. ([2006](#)), Wagner et al. ([2007](#)), Kodzwa et al. ([2007](#))	Starting temperatures range from 20 to 38.275°C Temperature width between 1 and 35°C	5 m/s–1.5 Ma	0.013 mm –38 cm	50–240 μm
Droplets	Hu et al. ([1994](#)), Nozaki et al. ([1995](#)), Richards and Richards ([1998](#)), Richards and Richards ([1998](#)), Mochizuki et al. ([1999](#))	Starting temperatures range from 30 to 58.4°C Temperature width between 3.2 and 12°C	0–5 m/s	300 μm–8 mm	

Table 2 continued

| Applications	References	Temperature ranges (°C) or shear stress (N/m²)	Characteristic fluid velocity	Characteristic length scale	Liquid crystal thickness
Microchannel flows	Csendes et al. (1996), Chaudhari et al. (1998), Noh et al. (2005), Iles et al. (2005), Muwanga and Hassan (2006a, b)	Starting temperatures range from 40 to 94°C Temperature width between 1 and 10°C	Motionless fluid 290 ml/min	150 μm	
Flow over curved surfaces	Camci et al. (1993), Chan et al. (2001), Chan (2001)	Starting temperatures range from 30 to 37°C Temperature width between 2 and 6.5°C	97.5 m/s	0.625–43.7 cm	10–30 μm
Natural convection	Kitamura and Kimura (1995), Jeschke et al. (2000), Trautman and Glezer (2002), Onbasioglu and Onbasioglu (2003)	Starting temperatures range from 29 to 35°C Temperature width between 5 and 20°C		0.12–150 cm	
Boiling convection	Dukle and Hollingsworth (1996a, b); Kenning and Yan (1996), Kenning et al. (2001), Lakshminarasimhan et al. (2005), Muwanga and Hassan (2007)	Starting temperatures range from 40 to 104°C Temperature width between 5 and 25°C	0.695–1.7 m/s	1.067–8 mm	35 μm
Narrow-band thermochromic liquid crystal thermometry	Simonich and Moffat (1982), Akino et al. (1986b), Kassab et al. (2001)	28.7–33			
Shear stress measurements	Klein and Margozzi (1970), Reda and Wilder (1992), Reda and Muratore (1994), Reda et al. (1994), Reda and Muratore (1994), Aeschliman et al. (1995), Reda et al. (1997b), Reda et al. (1997a), Reda et al. (1998), Buttsworth et al. (1998), Toy et al. (1999), Reda and Wilder (2001), Savory et al. (2000), Buttsworth et al. (2000), Reda and Wilder (2001), O'Brien and Zhong (2001), Fujisawa et al. (2003), Pradeep and Sullerey (2004), Nakano and Fujisawa (2006)	0–2,000 Pa	3.34 m/s–8 Ma	0.5–30.48 cm	5–100 μm
Transient heat transfer	Baughn et al.(1989), Camci et al. (1993), Wang et al. (1996), Barlow et al. (1997), Chyu et al. (1998), Critoph et al. (1999), Ekkad and Han (2000a, b), Chen et al. (2001), Yan and Owen (2002), Newton et al. (2003a, b), Owen et al. (2003), Tariq et al. (2003), Abu Talib et al. (2004), Chambers et al. (2003), Das et al. (2005), Kingsley-Rowe et al. (2005), Ochoa et al. (2005), von Wolfersdorf (2007)	Starting temperatures range from 30 to 48°C Temperature width between 2 and 11°C	0.46–97.5 m/s	0.56–43.7 cm	10 μm
Boundary layer, separated, and wake flows	Ekkad and Han (1996), Hacker and Eaton (1996), Zhong et al. (1999), Buttsworth et al. (2000), Praisner et al. (2001), Sabatino and Smith (2002), Kim et al. (2005); Praisner and Smith (2006a, b)	Starting temperatures range from 17 to 32°C Temperature width between 5 and 10.2°C	0.147–7.4 m/s	0.5–33.4 cm	1–55 μm

et al. 2004). Figure 31 (left) shows that in general, the right camera has lower errors than the left camera, and that the optimum angle for the right camera should be 20°, which results in an uncertainty of 1.1%. The velocity uncertainties, shown in Fig. 31 (right), show that both symmetric and asymmetric setups result in the same velocity uncertainty curves. Here, it can be seen that for total camera angles between 60° and 100°, the uncertainties are 5%, though at a lower total angle of 40°, the uncertainties increase to only 6%. A most interesting discovery was that while an increase in the number of PIV particles decreased the velocity uncertainties, it increased the temperature uncertainty (see Fig. 32a). The authors attribute this to the modification of the color characteristics of the CNLCs due to the PIV particles. Increasing the particle diameters also shows similar trends, larger particle diameters increase the temperature uncertainties while decreasing the velocity uncertainties (see Fig. 32b). The authors also attribute this to the corruption of the CNLCs color content due to the increased presence of the PIV tracer particles. Lastly,

making the particles brighter by increasing their peak intensity reduces both the uncertainties in the velocity and temperature (see Fig. 32c). Furthermore, it can be seen that beyond peak intensities of 200, the uncertainties for both velocity and temperature almost flatten to values of ~ 5 and $\sim 1\%$, respectively.

7. Applications: temperature and velocity measurements within fluid flow

Perhaps the first application of CNLCs towards fluid dynamics research was the work of Klein (1968a, b) in 1968, who showed the potential for using CNLCs to determine heat transfer rates by qualitatively observing the color play of a thin layer of CNLCs coated on a supersonic model within a Mach 1.98 flow. Since then, countless research has been done to measure surface temperature and heat transfer rates for various fluid flows, which have been categorized in Table 2. In the present review, the focus will

Fig. 33 *Top left* state of heat conduction, $\Delta T = 3$ K, $\upsilon = 20$ cSt, $Pr = 205$, $Re = 9.7 \times 10^5$. *Top right* steady, four-vortex convection, $\Delta T = 9$ K, $\upsilon = 3$ cSt, $Pr = 39$, $Re = 2.7 \times 10^7$. *Bottom row* steady, four-vortex convection: *left* $\Delta T = 8$ K, $\upsilon = 20$ cSt, $Pr = 20^5$, $Re = 2.6 \times 10^7$, *right* $\Delta T = 6$ K, $\upsilon = 20$ cSt, $Pr = 205$, $Re = 1.9 \times 10^7$ (Ozawa et al. 1992)
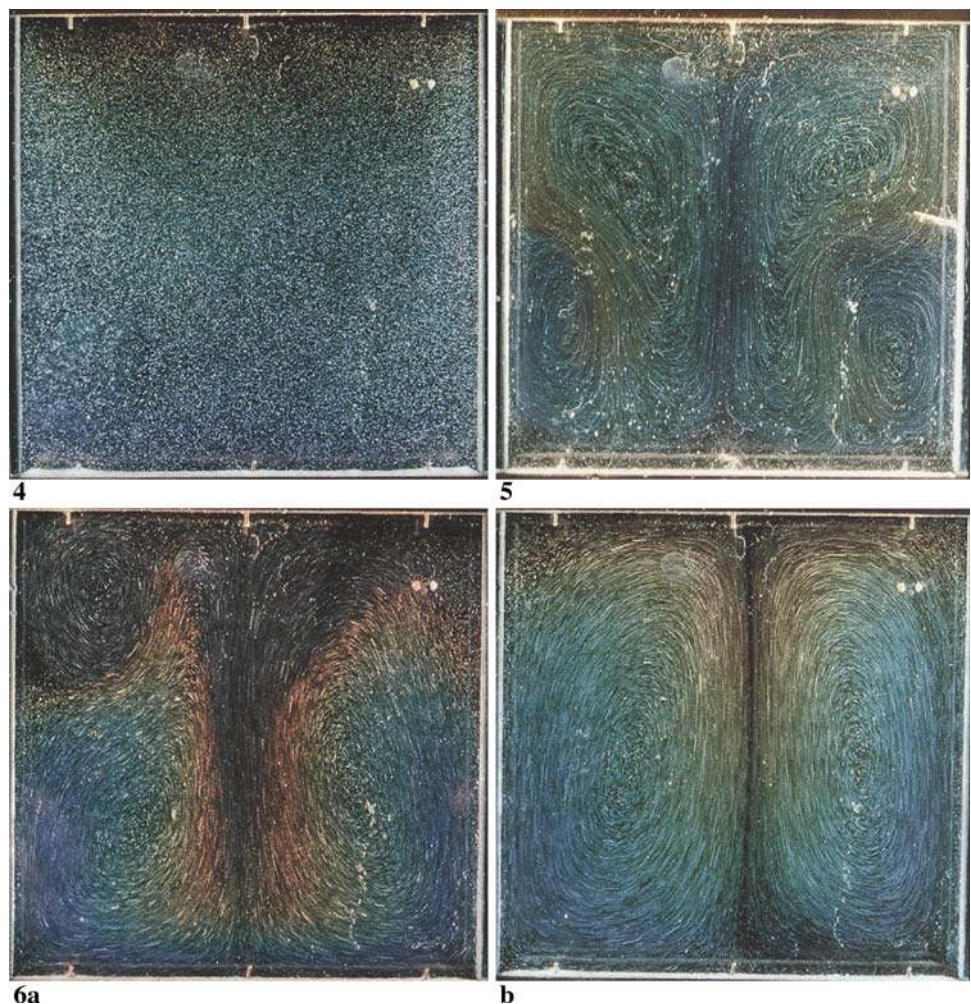
be on applications towards measurements of temperature and velocity within fluid bulk, as this is an area that has not been as developed or explored as the former.

7.1 Two-dimensional DPIT/V applications

Two-dimensional DPIT/V has been used mostly to study convective flows within confined cavities and vortex flows. Below, these applications, as well as others, will be described.

7.1.1 Convective flows within confined cavities

Kimura et al. (1989a, b) were perhaps the first to perform simultaneous temperature and velocity measurements within a fluid flow. The hue was derived using Eqs. 11 and used to obtain the temperature distribution within a $50 \times 100 \times 6$ mm^3 cavity. The upper and lower copper walls were kept at a constant temperature of 25 and 30°C,

respectively, and the side walls, being transparent acrylic, had low thermal conductivity and were therefore considered adiabatic. The velocities were obtained by performing cross-correlation routines on the intensity buffers of the images. The working fluid was silicon oil, and the CNLCs' mean diameter was 200 µm. In these studies, they were able to show the development of two side-by-side rollers, where the flow moved up the side walls, and dropped down the middle of the cavity.

Ozawa et al. (1992) have performed experiments on a Hele-Shaw cell for varying Rayleigh numbers. In this study, the CNLCs' mean diameter was 10–20 µm. Using a $40 \times 40 \times 6$ mm^3 test facility, various flow patterns were visualized. Figure 33 (top left) shows no flow patterns, only a state of heat conduction, Fig. 33 (top right, bottom left and right) show three different steady, four-vortex convection patterns, and Fig. 34 shows four oscillatory, four-vortex convection patterns, which corresponded quite well to previous interferometry visualizations performed

Fig. 34 Oscillatory, four-vortex convection, $\Delta T = 10$ K, $\upsilon = 20$ cSt, $Pr = 205$, $Re = 3.2 \times 10^6$ (Ozawa et al. 1992)
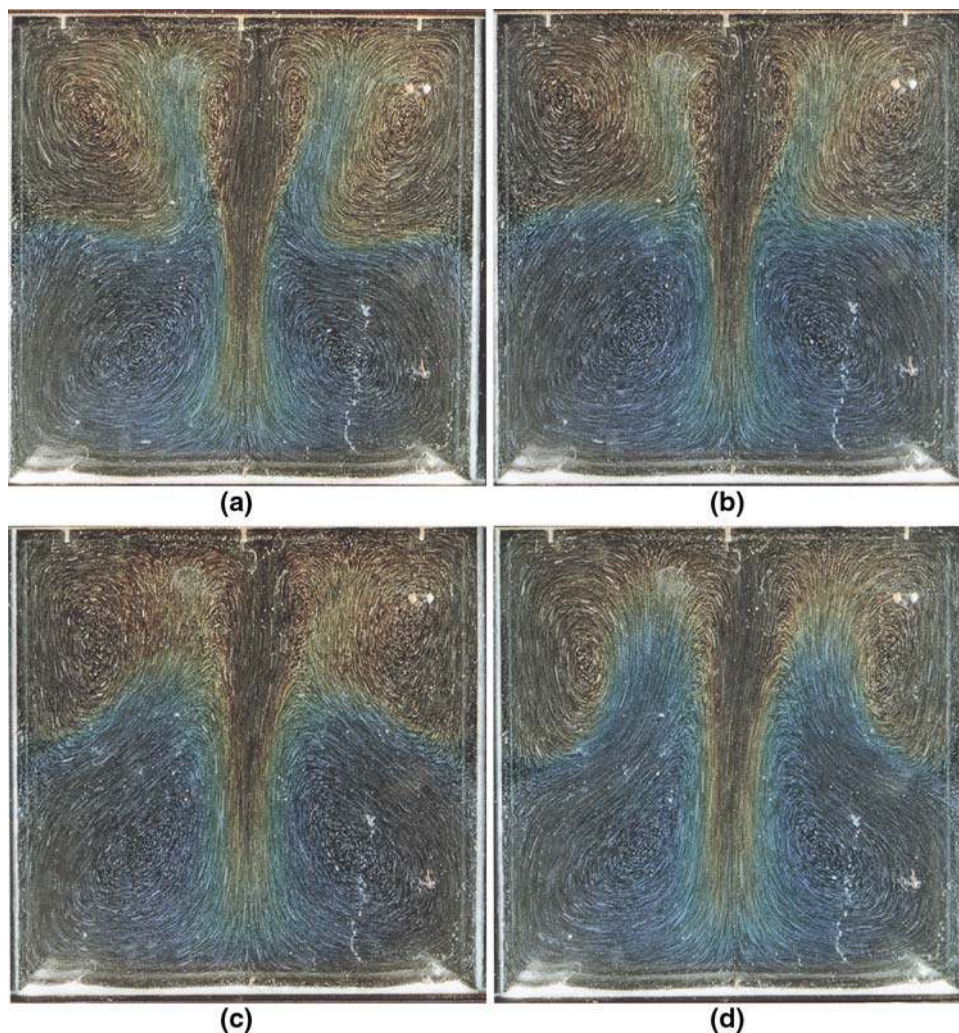
Fig. 35 Temperature and velocity distribution, oscillatory, four-vortex convection, $\Delta T = 5.7$ K, $\upsilon = 100$ cSt, $Pr = 900$, $Re = 2.55 \times 10^6$. The oscillation period is about 360 s (Ozawa et al. 1992)
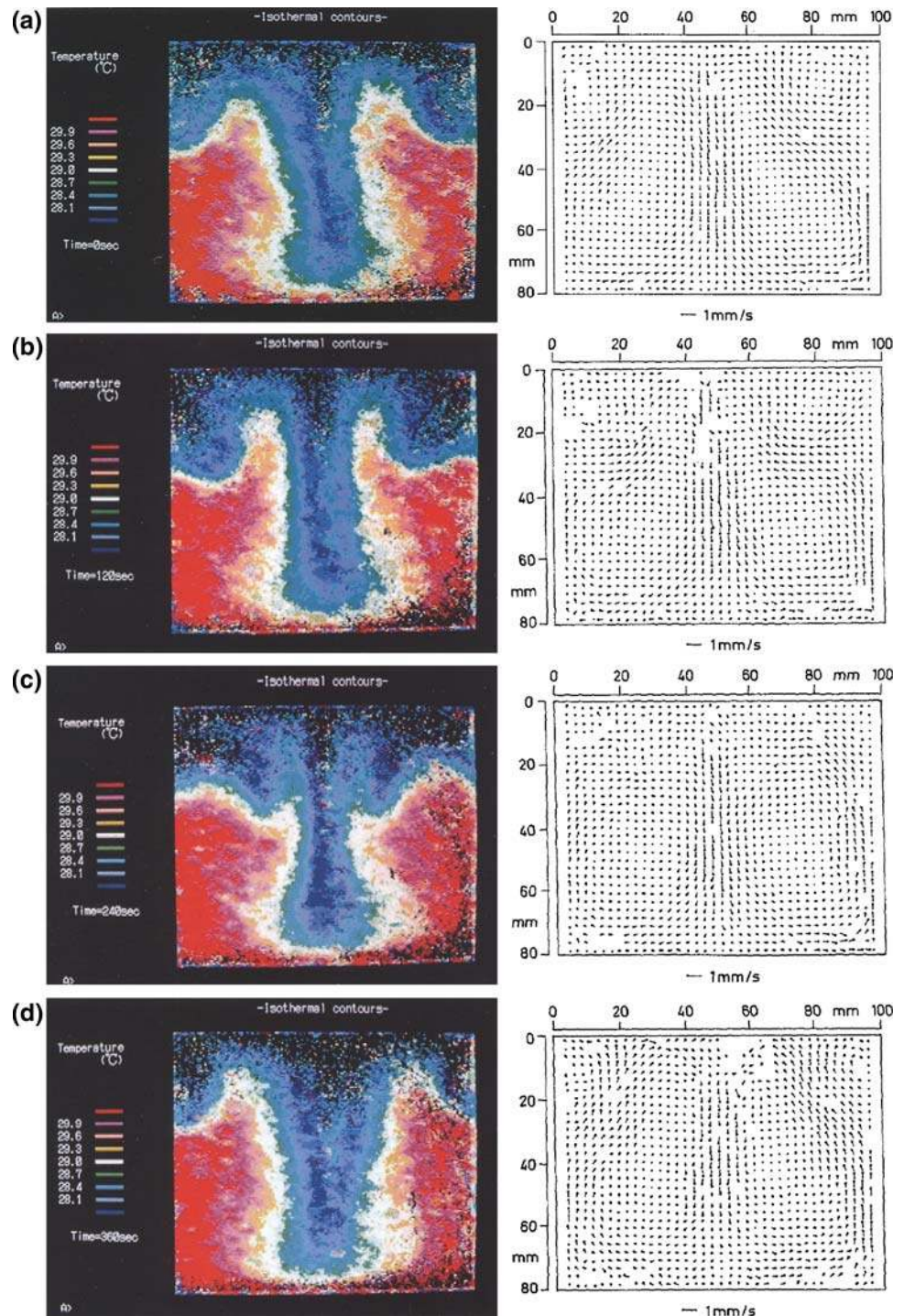

by Bühler et al. (1987). Figure 35 shows the temperature and velocity fields for the oscillatory four-vortex convection pattern shown in Fig. 34.

Hiller and Kowalewski (1986) and Hiller et al. 1989a, b, 1991, 1993, have studied natural convection within a cubic cavity, $38 \times 38 \times 38$ mm^3, in order to determine its flow structures in steady state as well as its transient development. The mid-plane was chosen as the region of interest,

in order to avoid the strongly three-dimensionalities that were observed outside this area. Rather than using micro-encapsulated CNLCs, unencapsulated CNLCs with mean 50 μm diameters were used, since their selective color scatter were reported to be brighter and purer. A glycerine–water mixture was used as the working fluid. A hue-temperature calibration was also used to convert color information to temperature. Figure 36 shows that the flow

Fig. 36 Multi-exposed color photograph of the convective flow in glycerol seeded with liquid crystal tracers in a differentially heated cavity. Tracers change color from blue to red following the clock-wise flow. *Left Ra* = 1.1×10^4, *Pr* = 6,900, *right Ra* = 8×10^4 (Kowalewski 1999)
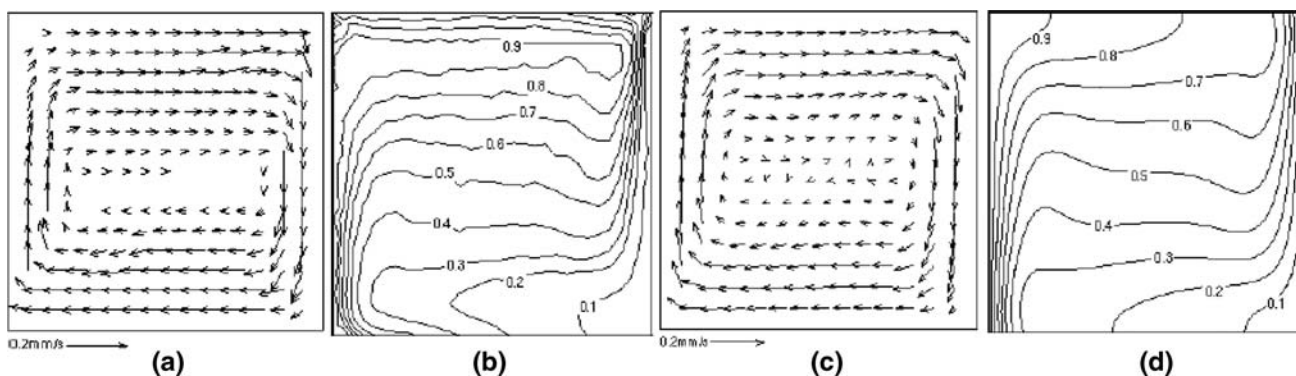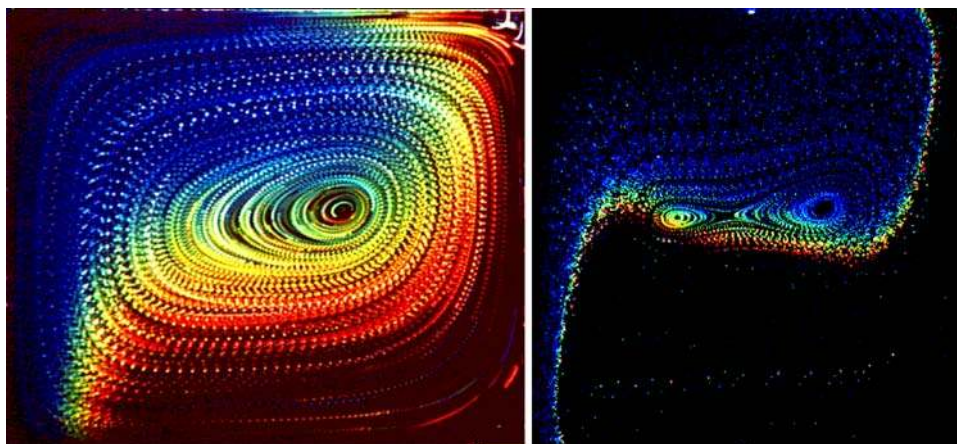
Fig. 37 a, **b** DPIT/V measured velocity and temperature fields for natural convection in the centre plane of a differentially heated cavity; numerical counterparts **c** and **d**. $Ra = 1.7 \times 10^5$, $Pr = 1,109$ (Kowalewski 1999)

Fig. 38 Steady-state *left* vorticity plot (*dashed/solid lines*) superimposed over the temperature plot (*color contours*). *Right* streamline plot (Dabiri and Gharib 1996). *Dashed/solid lines* are negative/ positive values, respectively
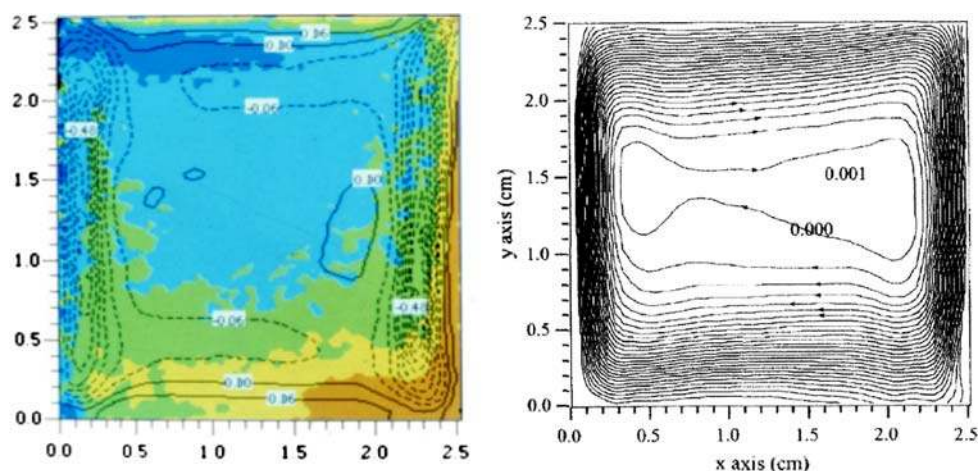

for a Rayleigh number of 1.1×10^4 contains a single vortex flow; however, for an increased Rayleigh number of 8×10^4, the flow develops two vortices at mid-plane. The onset of convection was also studied in this geometry, where the heating and cooling of the side walls was "jump started". The results were found to accurately portray the temperature and velocity fields when compared with simulations (see Fig. 37).

Similar experiments were also performed by Dabiri and Gharib (1996) who studied the effects of steady and oscillating heating and cooling of the side walls on mixing within the cubic cavity. A hue-temperature calibration curve was used to convert color information to temperature. A glycerine-water mixture was used as the working fluid. The steady-state results (see Fig. 38) show that most of the fluid motion is confined near the walls, allowing for

Fig. 39 Phase shift of 0°. *Left* vorticity plot (*dashed/solid lines*) superimposed over the temperature plot (*color contours*). *Right* streamline plot (Dabiri and Gharib 1996). *Dashed/solid lines* are negative/ positive values, respectively
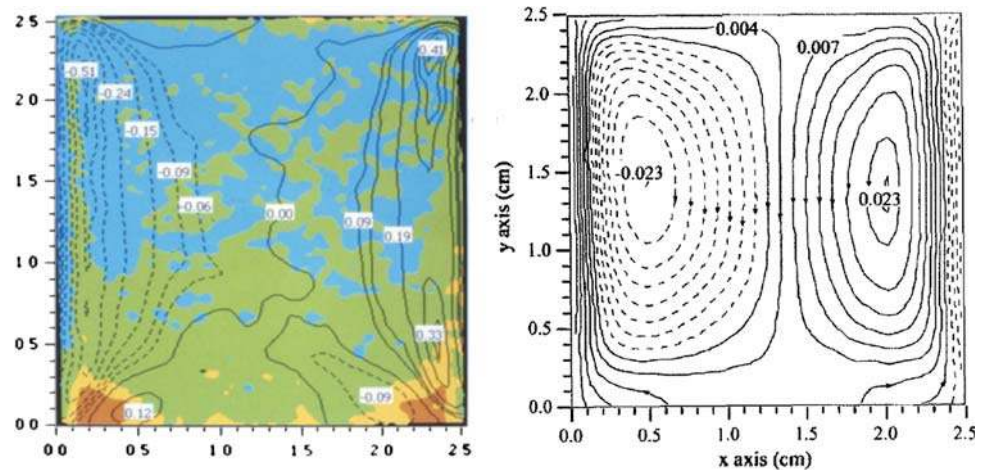
Fig. 40 Phase shift of 90°. *Left* temperature contours. *Right* streamline plot (Dabiri and Gharib 1996). *Dashed/solid lines* are negative/positive values, respectively
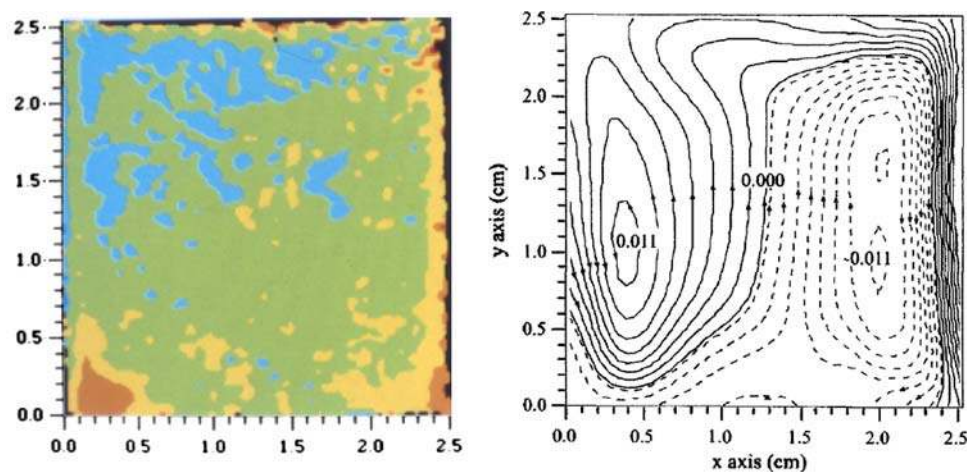
Fig. 41 Phase shift of 180°. *Left* temperature contours. *Right* streamline plot (Dabiri and Gharib 1996). *Dashed/solid lines* are negative/positive values, respectively
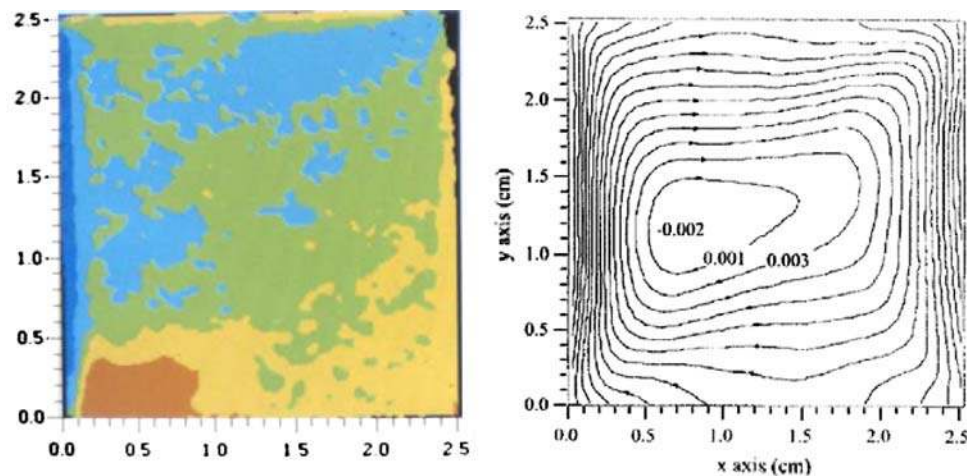
temperature stratification to build up within the central cavity region. However, by sinusoidally oscillating the heating and cooling of the side walls at the Brunt-Väisälä frequency (Lighthill 1978; Turner 1973), with phase shifts of 0°, 90°, and 180° between them, the resulting vortex structures encompass the whole of the cavity chamber, thus

allowing for more effective mixing. This can be seen in Fig. 39 through Fig. 40, where the temperature stratification within the central cavity region is comparatively less (Fig. 41).

An interesting variation has been the study of the freezing process of water in a differentially heated cubic

cavity by Kowalewski (1999, 2001, 2002). The side walls were suddenly heated and cooled to 10 and −10°C, respectively, causing the fluid at the cold wall to continually freeze and the ice boundary to continually move towards the center of the cavity. Distilled water was used as the working fluid, and CNLCs with 50 μm mean diameters were used to seed the flow. An example of the transient development of the thermal flow field is shown in Fig. 42, where the top/bottom rows show the results after 500/3,000 s, and the left/right columns show the velocity and temperature fields. Most interesting is the development of the smaller counterclockwise-rotating vortex that resides below the larger clockwise-rotating vortex. The authors attribute its existence the fact that at 4°C, the density of water is a local maximum, such that increasing or decreasing temperature causes a reduction in the density of water. Because the heat transfer is stronger in the upper right part of the cavity, the growth of the ice boundary is fairly slow at that region. After transferring most of its heat at the upper right corner region, the fluid flow down the

face of the ice cannot prevent the growth of the ice as effectively, allowing the ice on the middle to lower portions of the cold (right) boundary to grow more rapidly. Figure 43 shows the qualitative visualizations for this flow. Figure 44 shows a second configuration, the top wall was kept at −10°C, while the other walls were non-adiabatic.

Natural convection within a cubic cavity with a baffle at mid-height has also been studied both experimentally and numerically by Li et al. (2007). The baffle contains a circular hole in its middle, such that when the bottom is heated and the top is cooled, flow moves from the lower and upper chamber to the upper and lower chamber, respectively, creating vortex-ring structures, as shown in Fig. 45, which impinge on their respective walls creating regions of high heat transfer. The authors also point out that the two streams touching each other at the baffle opening exchange heat, and that the mixing and heat exchange between the incoming flow and the vortex-ring structure in each of the chambers are weak.


Fig. 42 DPIT/V **a** and **b** measured velocity and temperature fields for natural convection in centre plane of differentially heated cavity at 500 s (*top*) and 3,000 s (*bottom*). $T_h = 10$°C, $T_c = -10$°C; $Ra = 1.5.10^6$, $Pr = 13.3$ (Kowalewski 2001)
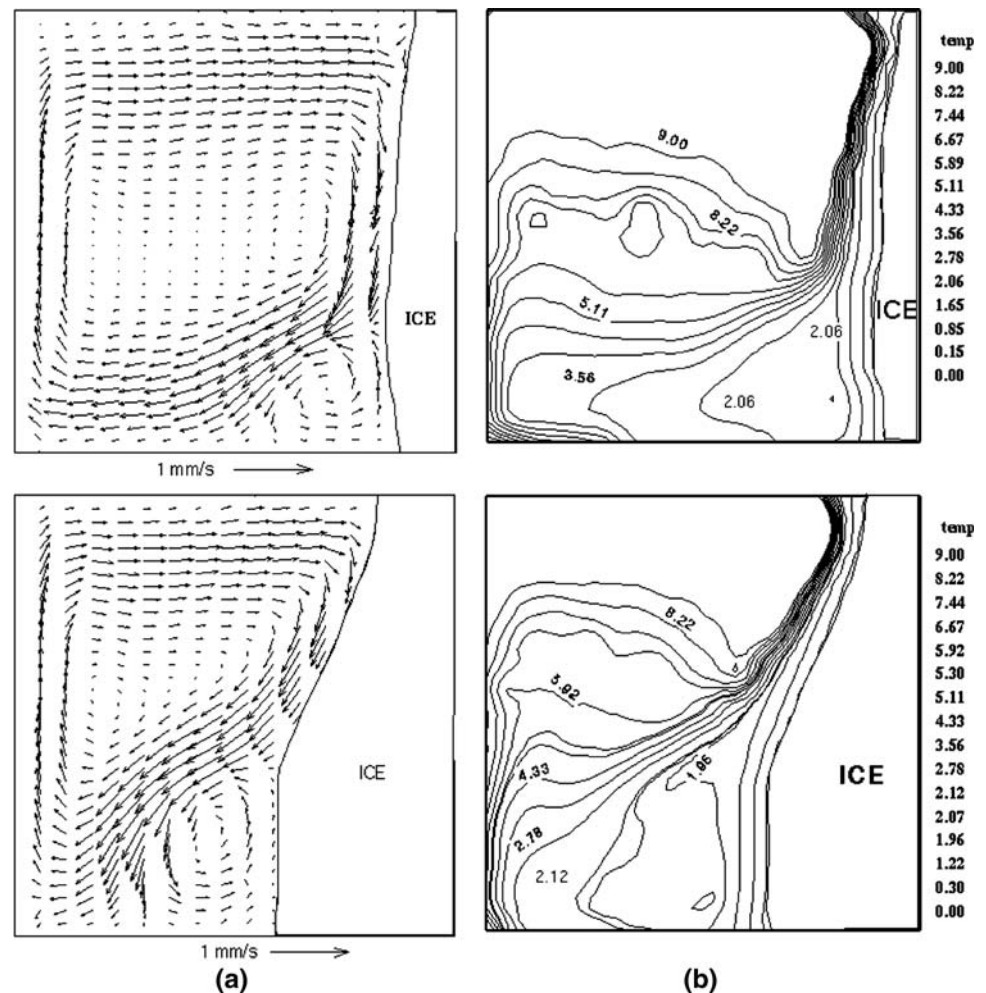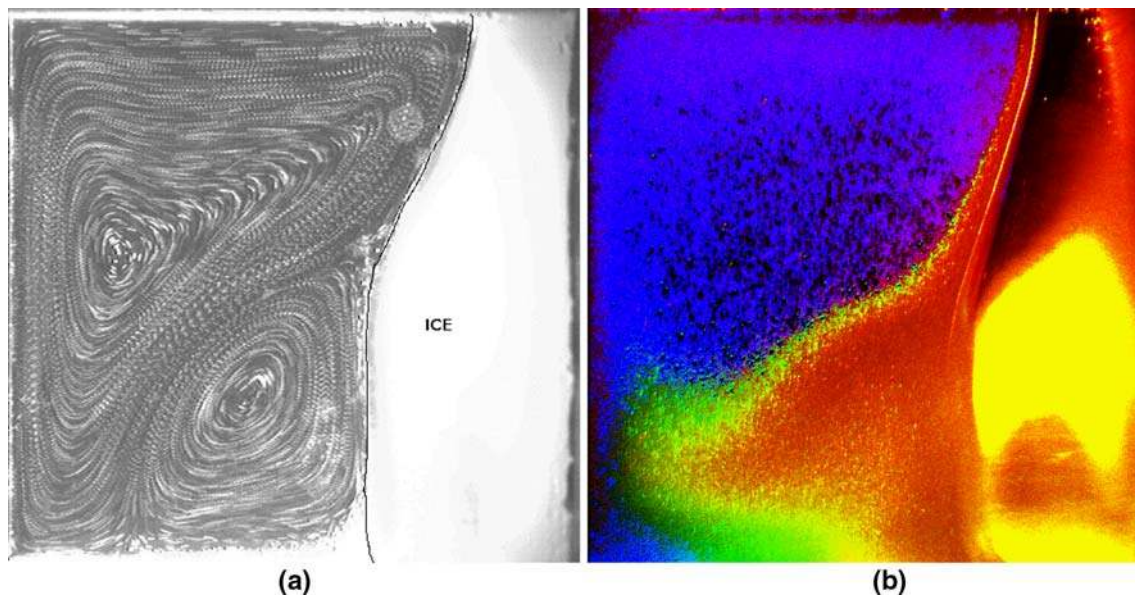
Fig. 43 Visualization of natural convection in freezing water. **a** Particle tracks showing flow structure, **b** liquid crystal tracers indicating variation of temperature. $T_h = 10°C$, $T_c = -10°C$ (Kowalewski 2001)
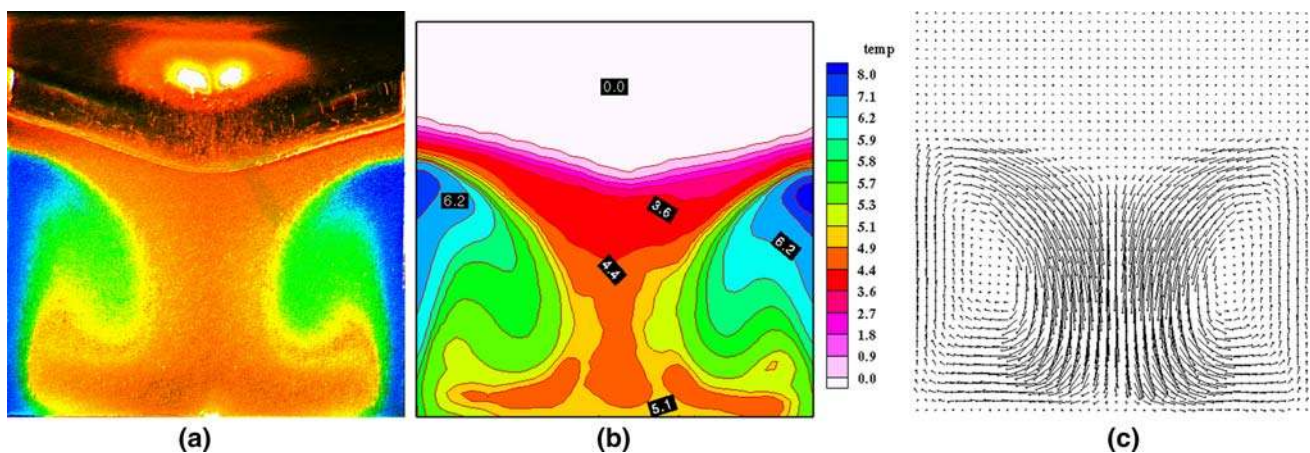
Fig. 44 Freezing of water from the top in the lid cooled cavity. **a** Recorded image of CNLC tracers, evaluated **b** temperature, and **c** velocity fields. Time step is 3,600 s after cooling starts; $T_c = -10°C$, text $= 20°C$, $Ra = 3.106$, $Pr = 13.3$ (Kowalewski 2001)

7.1.2 Vortex flows

Towards the development of the thermometry and velocimetry technique using liquid crystals, Dabiri and Gharib (1991a), Dabiri and Gharib (1991b) and Dabiri and Gharib (1995) have extracted the temperature and velocity field at the center-plane of a vortex ring. A hue-temperature calibration curve was used to convert color information to temperature. The working fluid was water seeded with 150 µm mean diameter CNLCs. Figure 46 shows processed images from the vortex ring at ~ 1.5 diameters and ~ 3 diameters downstream. The color contours in these images reflect the color play of the liquid crystals, where

red is the coldest temperature, 22.5°C, and blue is the hottest temperature, 25.5°C. Figure 46 clearly shows the entrainment of the warmed ambient fluid (green contours) into heated vortex ring (blue contours).

Park (1998), Park et al. (2001), and Park and Gharib (2001) have investigated the wake of a heated cylinder using DPIT/V. A hue-temperature calibration curve was used to convert color information to temperature. The working fluid was water seeded with 40 µm mean diameter CNLCs. A sample raw image is shown in Fig. 47. By phase averaging their results, they were able to isolate and calculate the incoherent turbulent heat flux vector. In comparison with the molecular heat flux vector (see

Fig. 45 Experimental (*left*) and numerical (*right*) visualization of the temperature field at the vertical mid-plane of the cubic cavity. The streaking of the liquid crystal particles (*left*) provide a qualitative measure of the velocity field (Li et al. 2007)
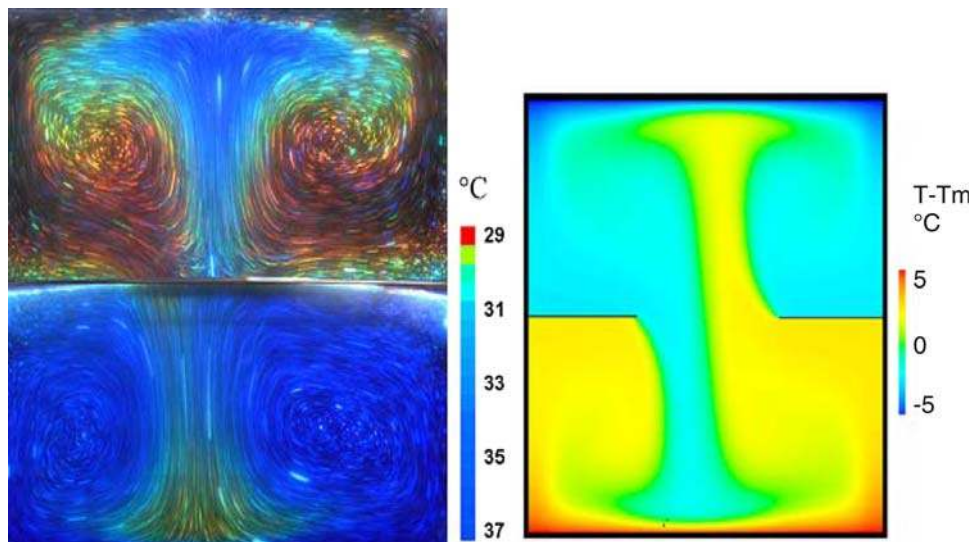
Fig. 46 Contours of temperature plot of a heated vortex ring at: *left* ∼1.5 nozzle diameters downstream of jet exit (Dabiri and Gharib 1991a), *right* ∼3 nozzle diameters downstream of jet exit (Dabiri and Gharib 1991b)
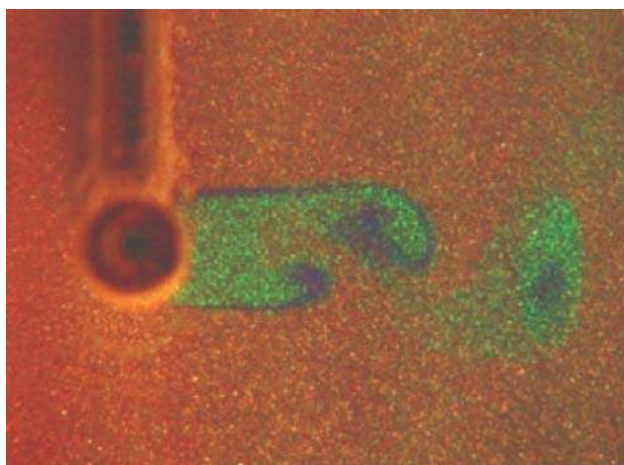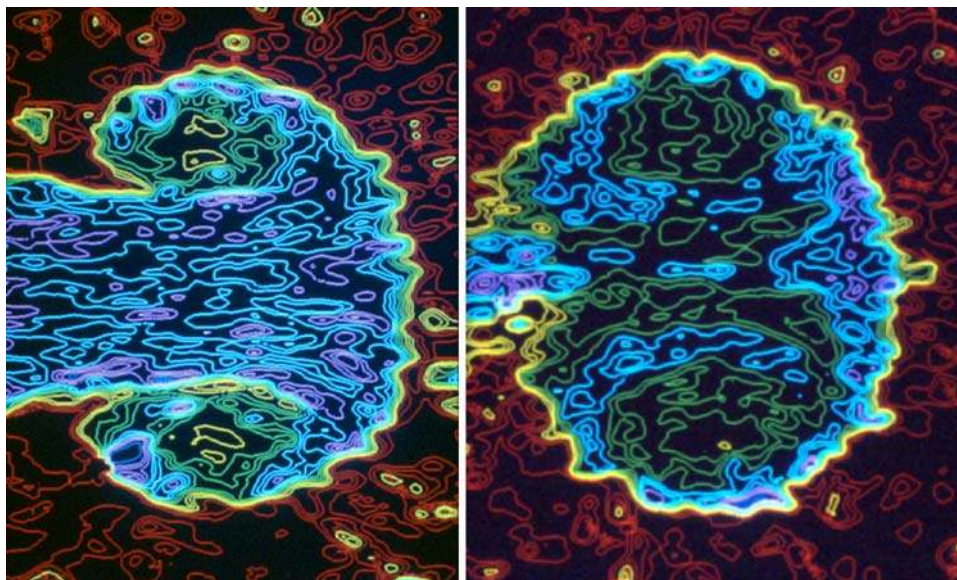
Fig. 47 Instantaneous view of the flow behind a heated circular cylinder (Park 1998; Park and Gharib 2001)

Fig. 48), the author has shown that within the vortical structures, the molecular heat flux vector was most often nearer to being orthogonal to the incoherent turbulent heat flux vector rather than co-linear, implying that originally suggested gradient transport models are inappropriate for modeling the turbulent heat transport in the near wake of a circular cylinder.

Park (1998) and Park et al. (2001) have also investigated the effect of transverse oscillations on the heat transfer from a heated cylinder. Their observations, for example, have shown that for a Strouhal frequency of 0.21, the heat transfer increases by 50% for oscillation amplitude ratios (amplitude-to-diameter) of 0.1 and 0.2. Upon interrogation, they found that for a stationary cylinder, a wake bubble containing mostly stagnant fluid existed behind the cylinder, which did not convect heat away from the cylinder's base
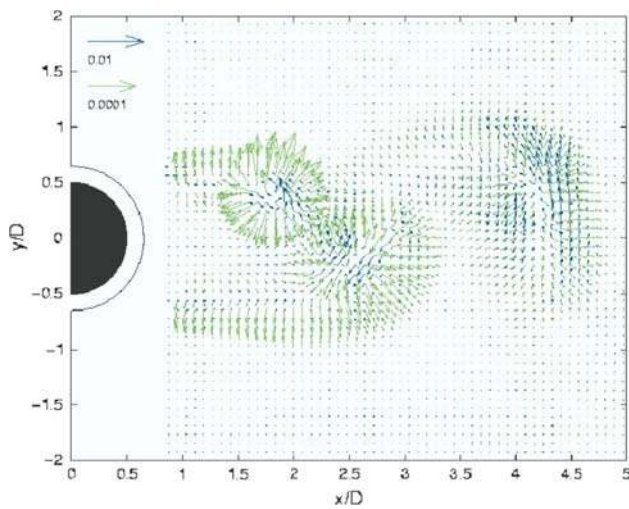
Fig. 48 Comparison of the direction of the phase averaged molecular (*green vectors*) and incoherent heat flux vectors (*blue vectors*) in the wake of a stationary cylinder (Park 1998)

(see Fig. 49, left). Upon introducing oscillation, however, the vortex roll-up becomes sufficiently close to the base of the cylinder to convect heat away from the cylinder's base (see Fig. 49, right). The authors also show that the heat transfer correlates with the flux of the out-of-plane vorticity, explaining the correlation in the decrease of the bubble wake's length with increasing vorticity flux, which is consistent with Roshko's cavity theory (Roshko 1993).

Motivated by these results, using DPIT/V, Pottebaum and Gharib (2006) performed a parametric investigation to determine the effects of oscillation frequency and amplitude, Reynolds number, aspect ratio and Prandtl number on heat transfer from a heated cylinder. The authors found that the heat transfer enhancements seen at the Strouhal frequency and its harmonics was limited to amplitude ratios less than 0.5, and the heat transfer coefficient was significantly affected by the details of the vortex roll-up process in the cylinder's wake and the transverse cylinder velocity.
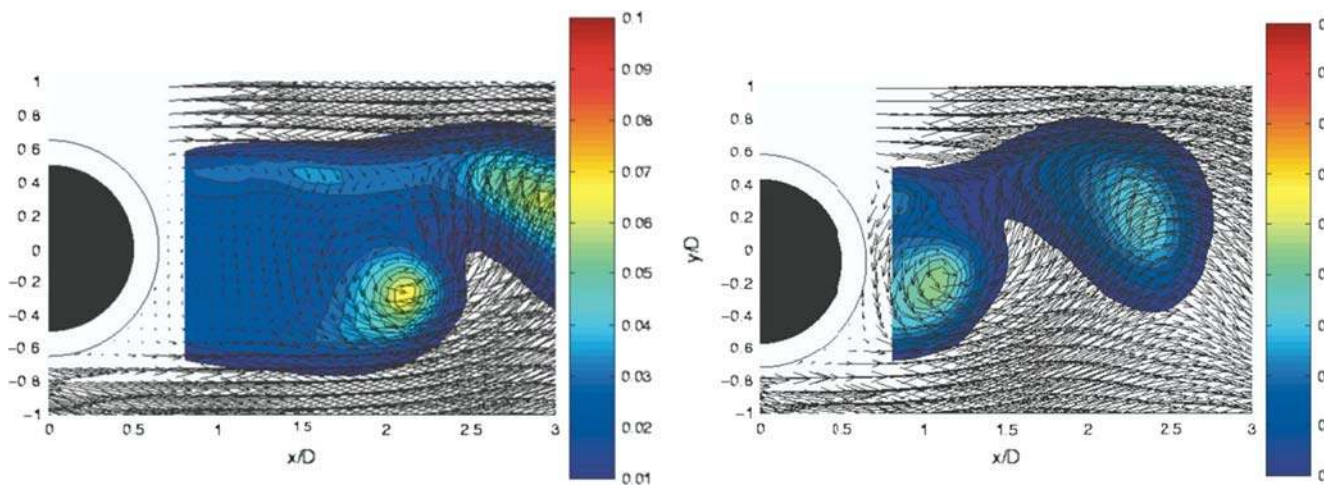
Fig. 49 $Re = 550$. *Left* flow about stationary cylinder shows a bubble region behind the cylinder with relatively stagnant fluid. *Right* $St = 0.21$ flow about oscillating cylinder shows that vortices form immediately behind the cylinder, eliminating the bubble region (Park 1998)
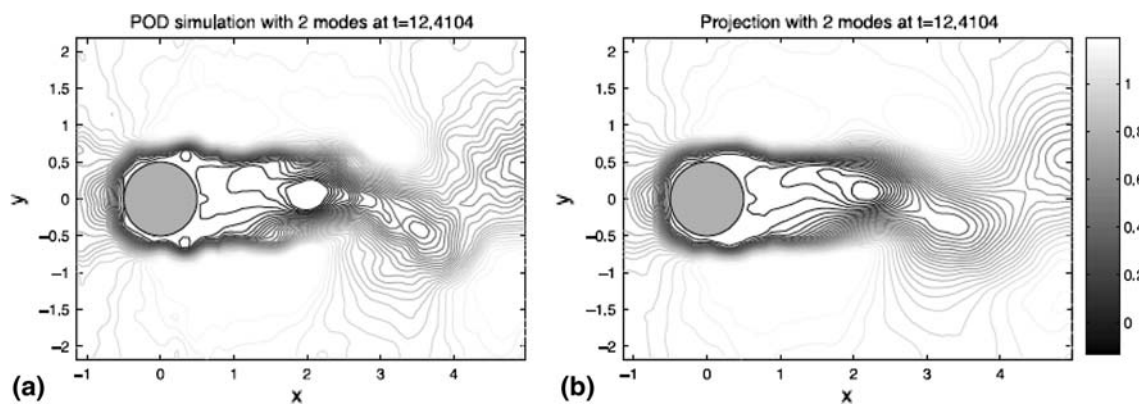
Fig. 50 Comparison of streamwise velocity contours of **a** POD simulation and **b** projected experimental data (Ma et al. 2002)
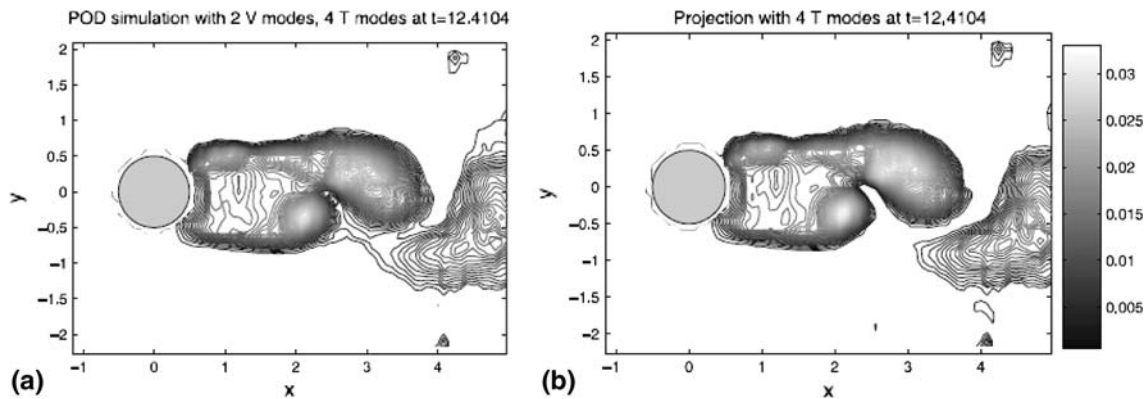
Fig. 51 Comparison of temperature contours of **a** POD simulation and **b** projected experimental data (Ma et al. 2002)

The development of DPIT/V has also brought about the interaction between computational methods and experimental methods. Ma et al. (2002) and Ma et al. (2003) have shown, for example, that a low-dimensional Galerkin approximation of the Navier–Stokes and energy equations can be used to simulate short-term convective heat transfer in flow past a heated cylinder using hierarchical empirical eigenfunctions extracted from an ensemble of velocity and temperature snapshots using DPIT/V. The authors indicate that for $Re = 610$, only two velocity and four temperature proper orthogonal decomposition (POD) (Lumley 1970; Berkooz et al. 1994; Poje and Lumley 1995; Delville and Bonnet 2001; Boree 2003) modes are necessary to reasonably describe its short-term flow dynamics (see Figs. 50, 51). Further investigations by these authors, however, have shown that nonlinear Galerkin approximations must be used to more effectively capture both the short- and long-term flow dynamics.

Günther and Rudolf von Rohr (2002b) studied the structure of the temperature field within a water channel facility with a heated sinusoidal bottom wall. A uniform surface heat flux was maintained at the sinusoidal wall, and encapsulated CNLC particles with a mean diameter of 19.75 μm were used as temperature sensors. Using DPIT, the authors obtained characteristic scales from two-point correlations and from POD analysis for mixed and forced convection, $Re = 725$ and 3,300, respectively, based on the half-height of the channel, with $Pr = 4.82$. Figure 52 shows instantaneous raw images of the flow seeded with encapsulated CNLCs for both the mixed and forced convection cases. Figure 53 show the two-point correlation, $R_{TT}(y_1, y_1', \Delta z)$, at $y_1'/\Lambda = 0.3$, where Λ is the wavelength of the sinusoidal wall, and y_1 is the vertical axis at 143° from the positive x-axis, for $Re = 725$ (mixed convection, left), and $Re = 3,300$ (forced convection, right). Though these flows are different types of convective flows, both plots show similar contours. Figures 54 and 55 show the first four eigenfunctions from the first four dominant POD

modes for a decomposition of the temperature fluctuation from 317 realizations in the tilted cross-plane, for $Re = 725$ and 3,300, respectively. These figures clearly show that the eigenfunctions show more insights on the flow structures than the two-point correlations. First, though the spanwise characteristic scale is similar for both cases, the extension in the y_1-direction is noticeably different. Second, the extrema of the eigenfunctions for $Re = 3,300$ are close to the location of the maximum Reynolds shear stress (not shown in figures). Third, the existence of the eigenfunctions throughout the domain for $Re = 725$, and its existence nearer to the wall for $Re = 3,300$ indicates the influence of natural convection in the former case.

In furthering the understanding of vortex-ring formation, Pottebaum and Gharib (2004) have studied the vortex-ring formation process for a buoyant plume. A water/glycerol mixture was used as the working fluid, which was seeded with 100 μm mean diameter CNLCs. An applied voltage and time interval was applied to the flush-mounted thermofoil heater at the bottom of the tank to generate a starting plume. A series of images showing the generation of the thermal plume and its vortex-ring pinch-off, along with their vorticity and temperature contours, is shown in Fig. 56. Using DPIT/V, the authors were able to show that the non-dimensional pinch-off time was between 4.4 and 4.9, which was consistent with previous predictions (Shusser and Gharib 2000).

7.1.3 Other flows

One of the more interesting applications of DPIT/V has been towards the investigation of thermocapillary flow in drops under low gravity. Towards this end, Treuner et al. (1995) developed a facility that held a drop in place using two vertically oriented tubes; the first tube held the drop at its top while heating it and the second tube held the drop at its bottom while cooling it. The drop sizes ranged

Fig. 52 Instantaneous RGB intensities for a flow over heated waves seeded with encapsulated CNLC particles (*left*) $Re = 725$ (mixed convection), $Pr = 4.82$ (*right*) $Re = 3,300$ (forced convection), $Pr = 4.82$ (Günther and Rudolf von Rohr 2002b)
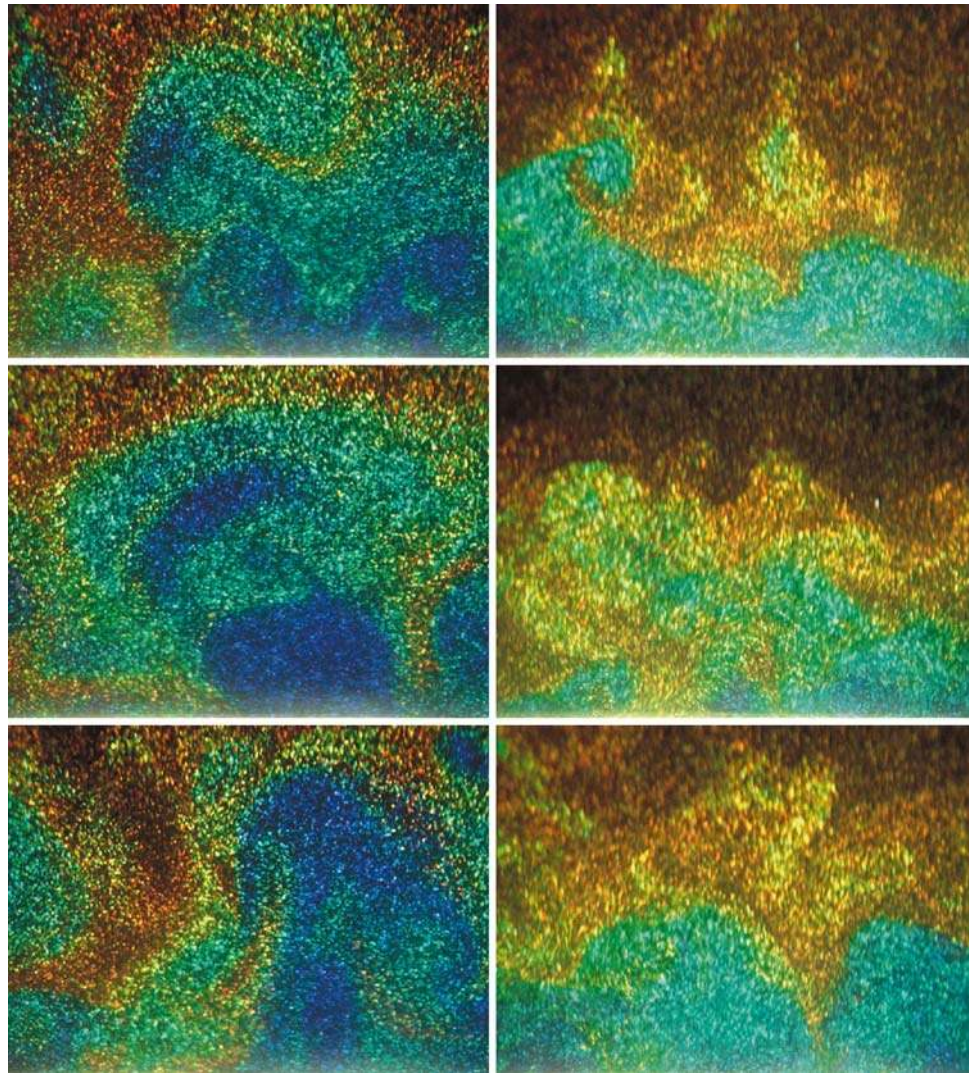
Fig. 53 Contours of the two-point correlation function in the vertical cross-plane, evaluated for $y_1'/\Lambda = 0.3$ at (*left*) $Re = 725$ (mixed convection) and (*right*) $Re = 3,300$ (forced convection). *Solid lines* represent positive values; *broken lines* indicate negative values. $Pr = 4.82$ for both cases (Günther and Rudolf von Rohr 2002b)
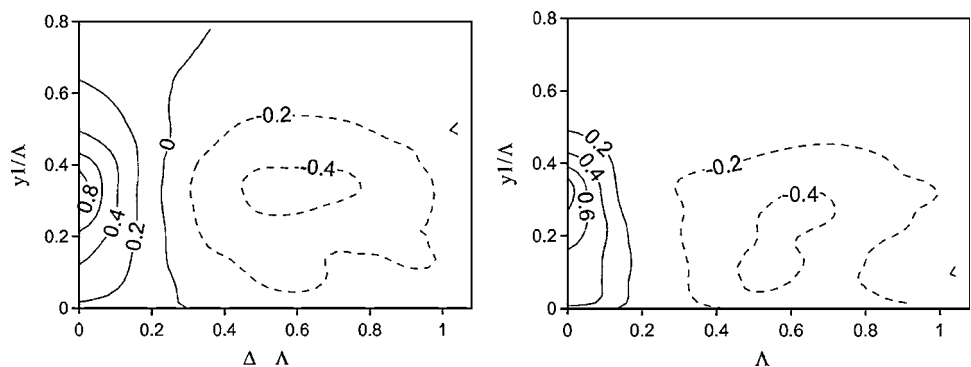
in size from 9 to 15 mm, and low gravity was achieved by performing the experiments during KC-135 parabolic flights, achieving average acceleration levels of 10^{-2} g. A glycerol/water mixture was used as the working fluid, and a hue-temperature curve was used to calibrate and extract the temperature field within the drops. The drops were observed orthogonally with respect to the light sheet that illuminated the diameter of the drops. The curvature of the drops was also taken into account in deriving a transformation of the real coordinates within the illuminated cross-section of the drop and the virtual coordinates of the acquired images. The angular dependences of the

Fig. 54 Contours of the eigenfunctions $\Pi_{1,T}, \ldots, \Pi_{4,T}$ from the dominant POD modes $1, \ldots, 4$ for a decomposition of the fluid temperature fluctuations T'_1 from 204 temperature fields (after the 50th crest) in the cross-plane. *Solid lines* represent positive values; *broken lines* indicate negative values. $Re = 725$ (mixed convection), $Pr = 4.82$ (Günther and Rudolf von Rohr 2002b)
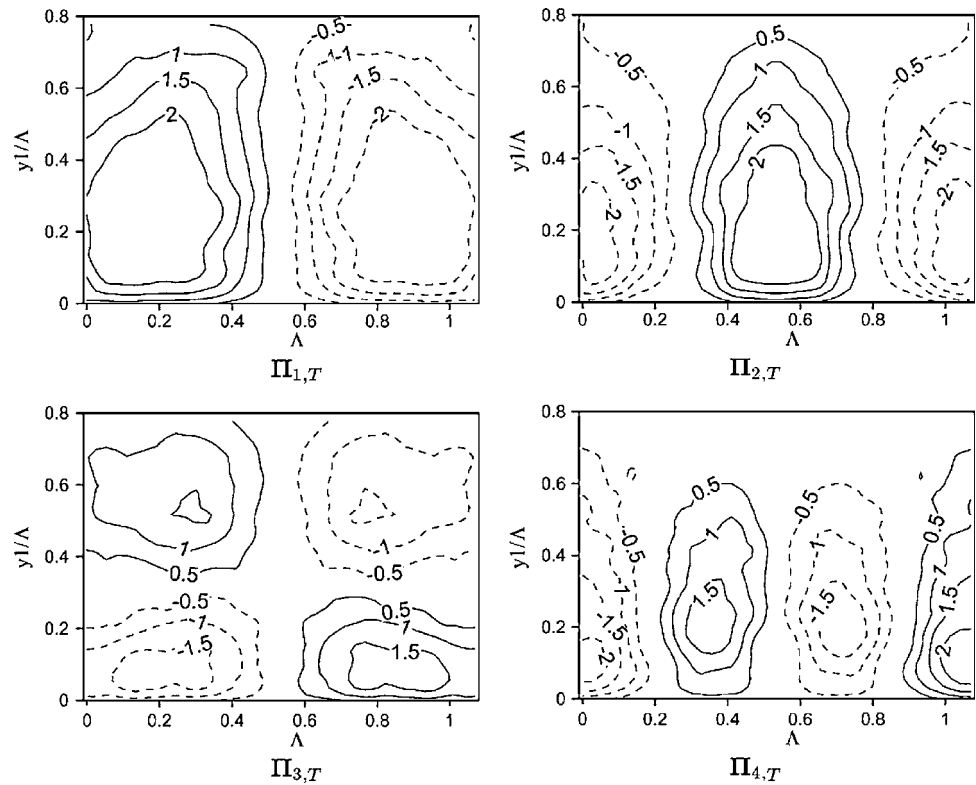
Fig. 55 Contours of the eigenfunctions $\Pi_{1,T}, \ldots, \Pi_{4,T}$ from the dominant POD modes $1, \ldots, 4$ for a decomposition of the fluid temperature fluctuations T'_1 from 317 temperature fields (after the 50th crest) in the cross-plane. *Solid lines* represent positive values; *broken lines* indicate negative values. $Re = 3,300$ (forced convection), $Pr = 4.82$ (Günther and Rudolf von Rohr 2002b)
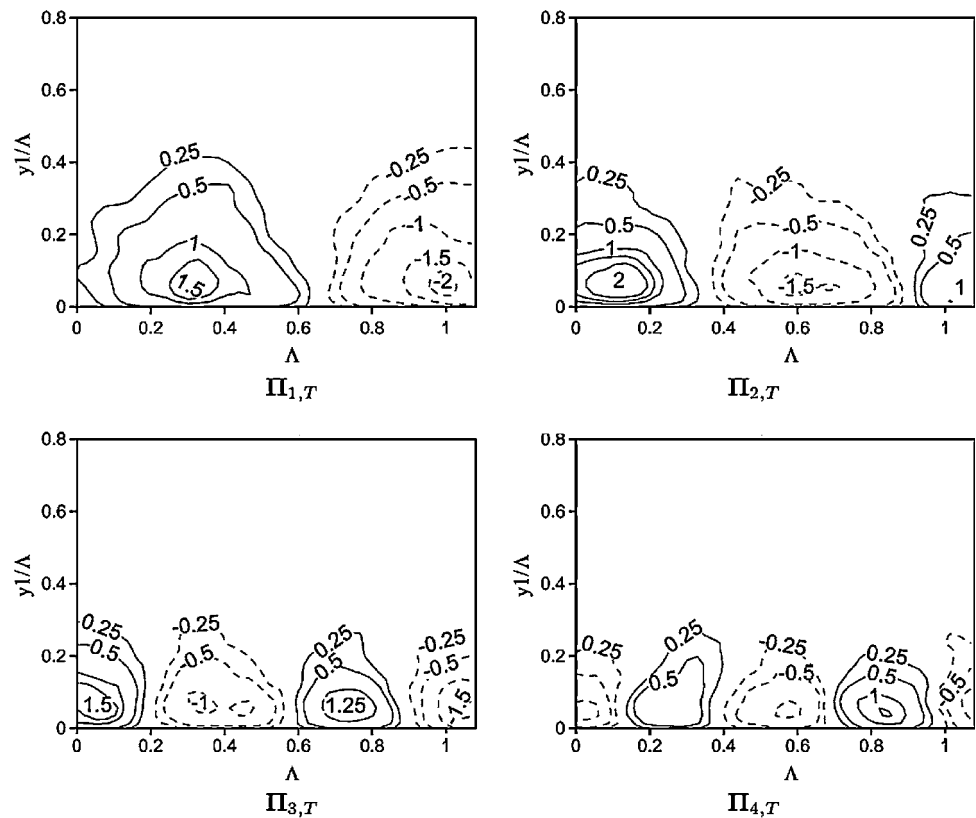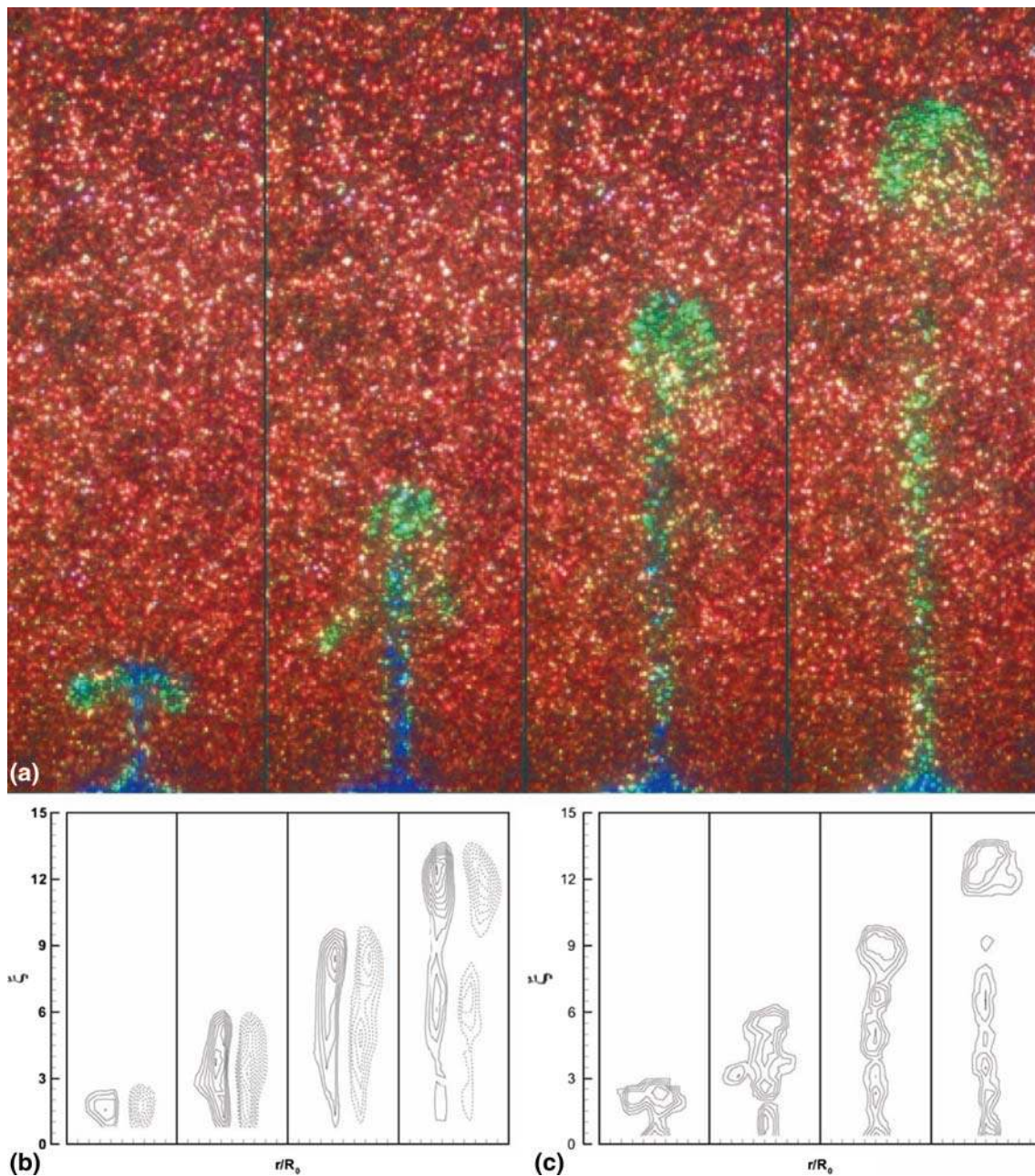
Fig. 56 Snapshots of the flow at non-dimensional times of 2.58, 5.17, 7.77, and 10.36. **a** Images of the starting plume, brightened to improve visibility and cropped horizontally to show the region of interest; **b** vorticity contours; **c** temperature contours (Pottebaum and Gharib 2004)

CNLCs' color scatter were also accounted for in order to determine accurate temperature calculations. Figure 57 shows the severity of the drop's curvature and the color reflection variation due to changes in the viewing angle. Upon acquiring a series of images, the time dependence of the flow was studied. Figure 58a, b, for example, show a raw image and its associated velocity field, and Fig. 58c is a schematic showing the evolving temperature field within the drop that develops due to the Marangoni effect.

In a unique experiment based on visual observations, Pehl et al. (2000) were able to show the feasibility of using CNLCs for visualizing temperature fields in pressurized liquids of up to 7,000 bar. Figure 59 shows the non-uniform temperature field at 3,920 bar during pressurization from 2,670 to 3,920 within 18 s. While Ireland and Jones (2000) have shown that pressures up to 133 bar do not affect CNLCs, the present work reveals that pressures as large as just over 3,900 bar affect the color play of the

Fig. 57 Resulting images due to different included angles. *Left* 90° included angle, *right* 50° included angle (Treuner et al. 1995)
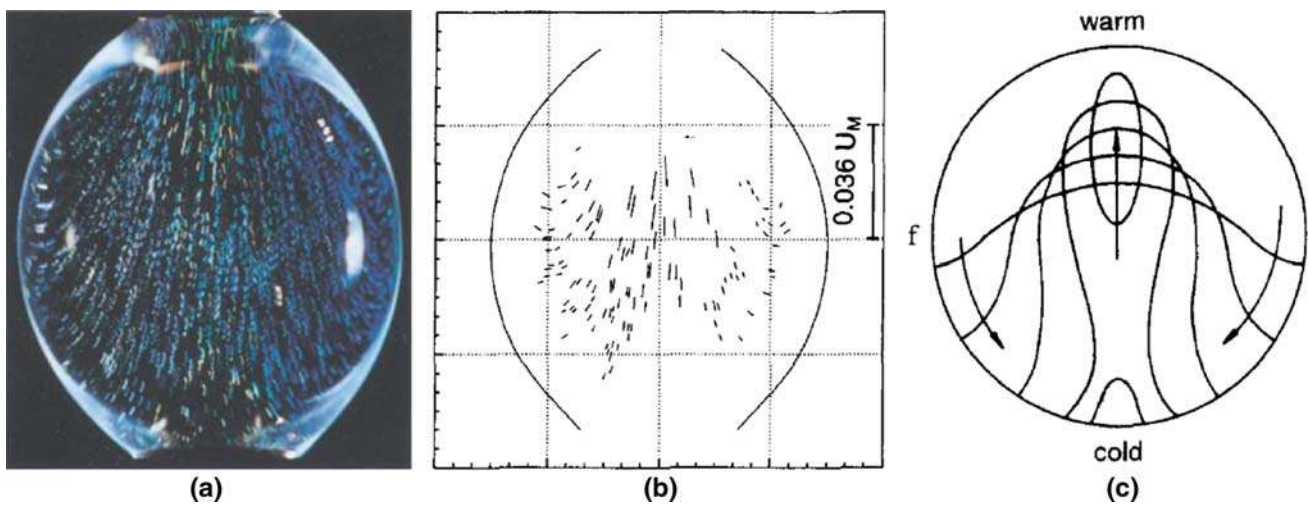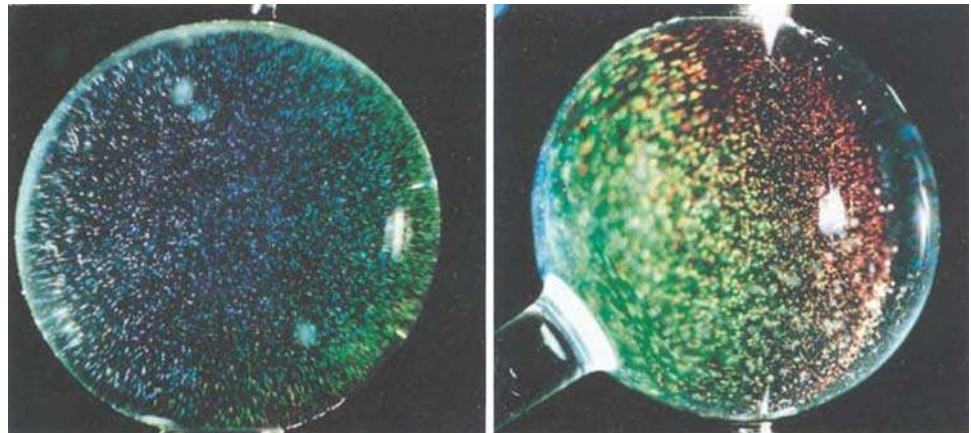
Fig. 58 a Sample image, **b** resulting velocity field, **c** evolving temperature field due to the Marangoni effect (Treuner et al. 1995)
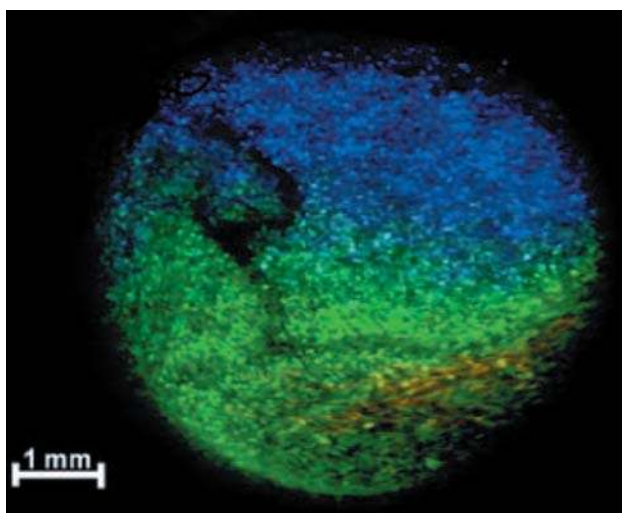
Fig. 59 Inhomogeneous temperature field at 3,920 bar originated by pressurizing water from 2,670 to 3,920 bar; CNLCs with start temperature at 10°C and a range of 1 K (Pehl et al. 2000)
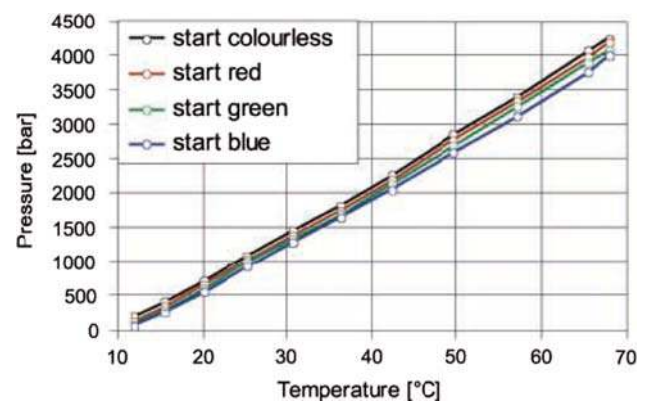
Fig. 60 Pressure/temperature data of isochromes (Pehl et al. 2000)

CNLCs. Figure 60 shows that for constant pressures and increasing temperatures, the scattered CNLCs wavelengths shift from red to blue, while for constant temperatures,

Fig. 61 Isothermal contour surface of thermal plumes (28.6°C). **a** Plume structure corresponding to a particular section of the flow, **b** plume structure in whole flow field (Fujisawa et al. 2005)
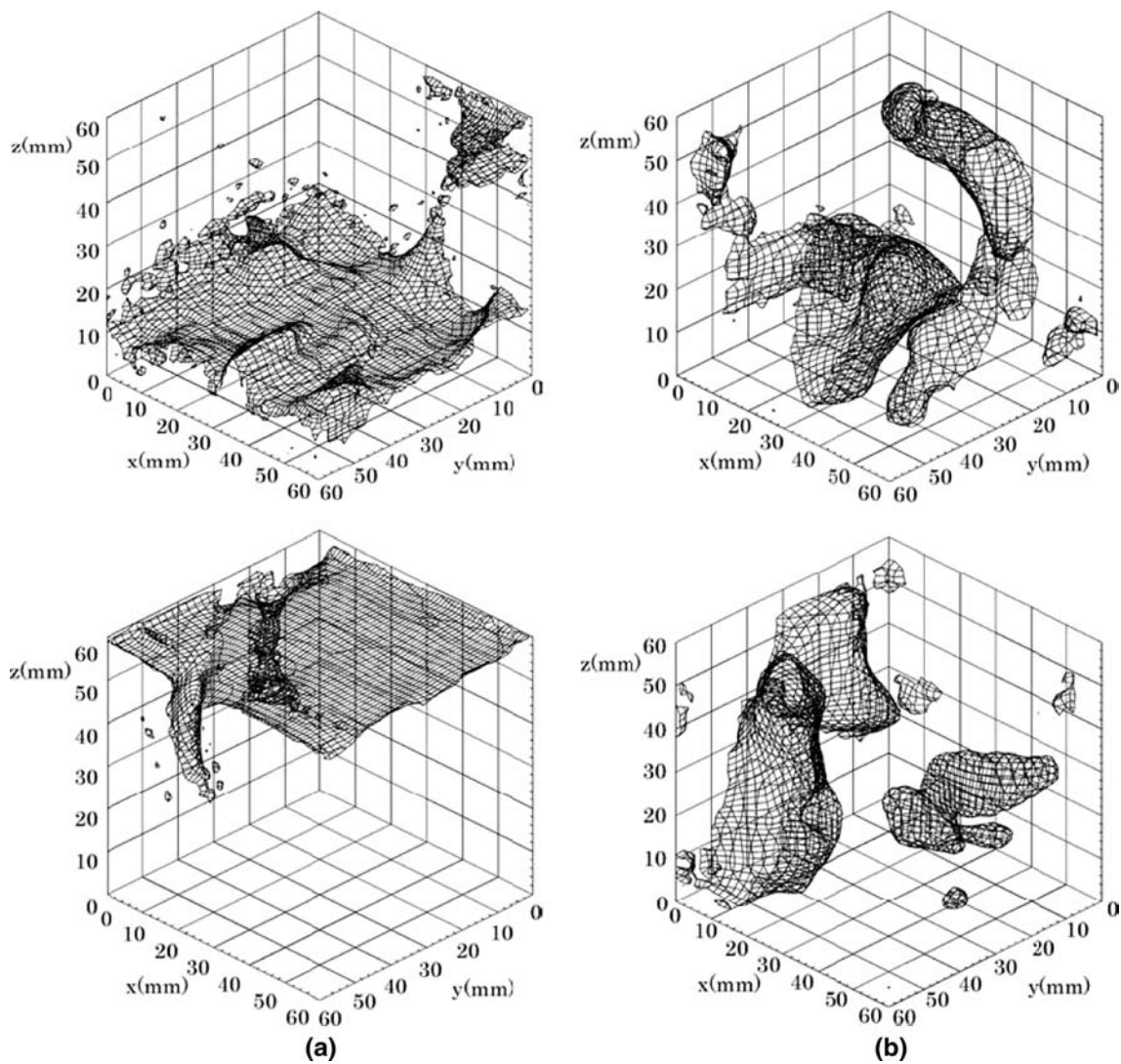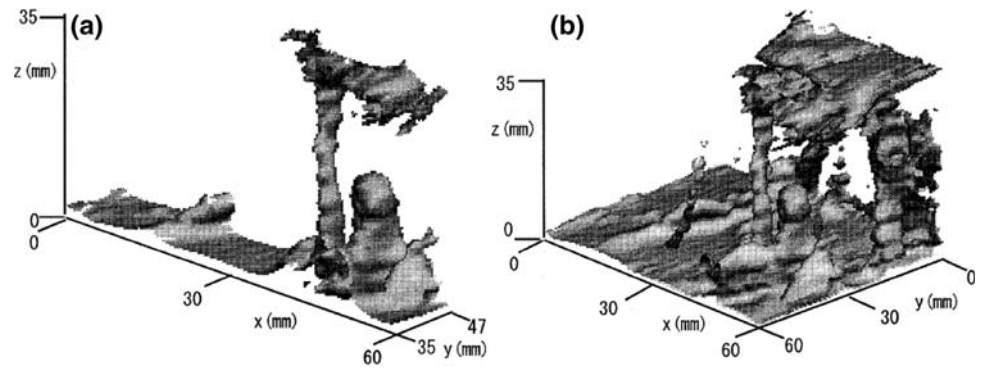
Fig. 62 *Left* contour surfaces of isothermal temperatures: **a** *T* = 28.6°C, **b** *T* = 28.4°C. *Right* contours surfaces of constant vertical velocities: **a** *v* = 1.1 mm/s, **b** *v* = −0.8 mm/s (Fujisawa et al. 2005)

Fig. 63 *Left* horizontal and vertical plane temperature fields. *Right* horizontal and vertical plane velocity fields. For both plots, the vertical plane is located at $y = 0$, however, it is shown towards the back to allow for viewing of the horizontal plane data (Fujisawa et al. 2008)
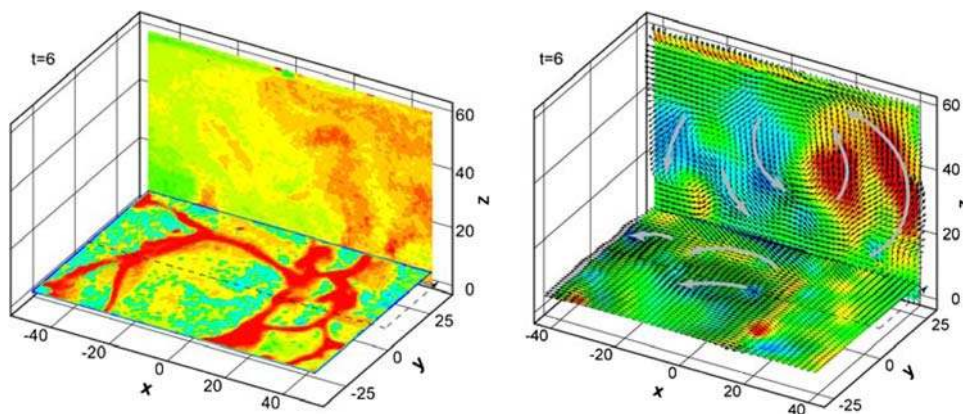
increasing pressures results in an opposite shift of the reflected CNLCs wavelengths from blue to red.

7.2 Three-dimensional DPIT/V applications

Since three-dimensional DPIT/V is relatively new, its applications and implementations are few. In developing the scanning DPIT/V method, Fujisawa and Funatani (2000) have mapped a three-dimensional turbulent thermal convection flow field. Towards this end, they were able to map the resulting plume structures within the flow field, as shown in Fig. 61. In combining this technique with stereo-DPIV, Fujisawa et al. (2005) have further mapped the development of plume structures within a three-dimensional turbulent thermal convection flow field. Figure 62 (left) shows the temperature isotherms at 28.6 and 28.4°C, while Fig. 62 (right) shows the velocity magnitude contours for 1.1 and −0.8 mm/s. Fujisawa et al. (2008) have also investigated the spokes structures of unsteady non-penetrative turbulent thermal convection within a horizontal fluid layer. Using simultaneous liquid crystal thermometry and velocimetry within two sheets, they were able to map the flow field, as shown in Fig. 63. Their results show that the convection patterns are created by the hot thermals emanating from the spoke structures, and the cool fluid moving downwards towards the center of the regions surrounded by the spokes. POD analyses also reproduced the main features of the convection, verifying the said observations.

Using a photographic scanning DPIT/V method, Ciofalo et al. (2003) were able to map steady-state Rayleigh–Benard convective flow using tomographic methods. Glycerol was used as the working fluid within a $60 \times 120 \times 240$ mm^3 chamber, seeded with 20–50 μm diameter CNLC particles. The Rayleigh numbers of the flows studied were within 3,000–20,000. Figure 64 shows the 3D assembly of 2D slices of the flow field. Figure 64a shows the existence of four transverse rollers, while Fig. 64b
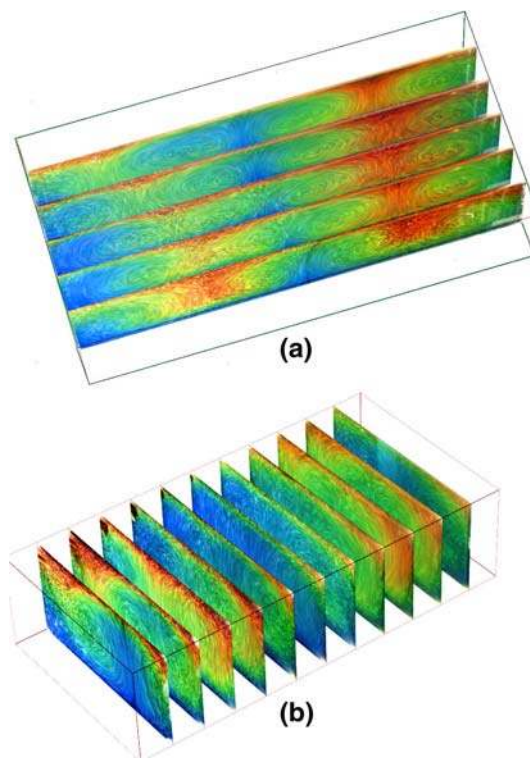
Fig. 64 Three-dimensional assembly of individual in-plane images obtained by multiple exposures **a** longitudinal sections **b** transverse sections (Ciofalo et al. 2003)

show the existence of longitudinal rollers. The colors reflect the temperature according to the color play of CNLCs, where blue is hot and red is cold. Three-dimensional reconstructions of the flow are shown in Fig. 65. The authors explain that Fig. 65 (left) clearly shows the existence of the four transverse rollers as well as their meandering, while Fig. 65 (right) exhibits recirculation regions that are spatially non-stationary, suggesting that the longitudinal rollers are not strictly aligned with the enclosure sides.
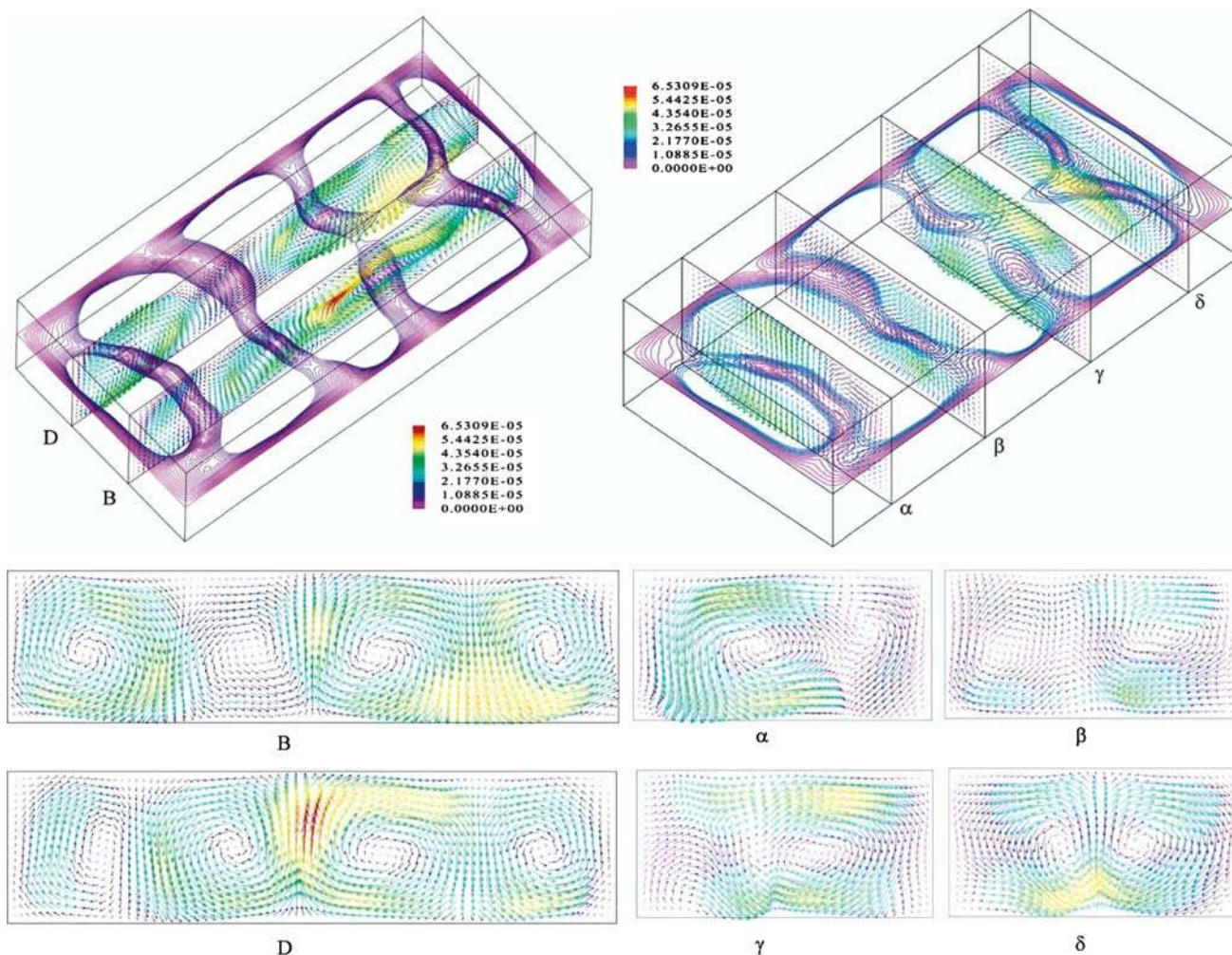
Fig. 65 Axonometric view of the enclosure showing isolines of the low speed (velocity magnitude $<12 \times 10^{-6}$ m/s) on the horizontal mid-plane and *left* velocity vector plots on selected longitudinal planes, *right* velocity vector plots on selected transverse planes. The *vector colors* indicate speed (Ciofalo et al. 2003)

Fig. 66 Maximization of color reflection. *Left* reflection spectra of cholesteric liquid crystal layers, l, left-handed mixture; r, right-handed mixture; S, left-handed layer superimposed over the right-handed layer. *Right* l_1 and l_2 are two identical left-handed layers; m, l_1 superimposed over l_2; S, l_1 superimposed over l_2 with a halfwave plate in between (Makow 1980)
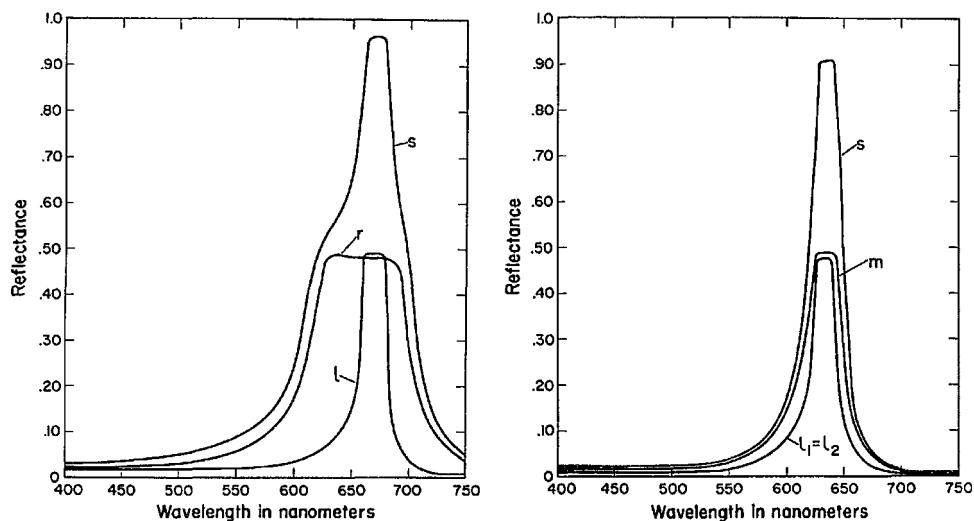
8. Concluding remarks

In conclusion, DPIT/V provides a powerful non-invasive and quantitative flow visualization method, capable of providing temperature and velocity measurements within two or three dimensions for a wide gamut of temperature and velocity ranges. CNLCs' temperature uncertainties, as described earlier, are from negligible to 7% of the calibrated temperature range, for approaches which account for the viewing angle. Since their temperature uncertainties are a function of its color-scatter temperature range, DPIT/V is ideal for use within smaller temperature ranges. Simultaneously, the motions of these liquid crystal particles can also be processed with DPIV algorithms to extract accurate velocity measurements. In conclusion, this review has not only laid out the principles of this methodology, but has also described the diverse and rich applications of this methodology.

While significant progress has been made towards the development of DPIT/V, there are potential improvements that can be implemented. Effective calibration methods used with liquid crystal paints that take into account the effect of background light (Sect. 5.1.3), digital resolution (Sect. 5.1.7), measurement noise (Sect. 5.1.8), hue calculations other color spaces (Sect. 5.1.11), and uncertainty analysis (Sect. 5.1.12) have not been used in DPIT/V applications, thereby providing avenues for improvement. Also, Roth and Anderson (2007) propose developing a calibration system based on light transmission through the liquid crystal as it may have the advantages of larger calibration ranges and less sensitivity toward illumination. Furthermore, realizing that since CNLCs reflect only 50% of the incident light (either the left- or right-handed circularly polarized component) within the reflection band, Makow and Sanders (1978) have shown that by either superimposing a layer of left-handed CNLC over a right-handed CNLC, or by using two layers of left-handed (or right-handed) CNLCs with a halfwave birefringent plate in between, it would be possible to obtain nearly 100% reflection within the reflection band (see Fig. 66). Implementation of such an approach would ease the illumination requirements by a factor of two. Other improvements may be achieved by furthering Frey's studies towards lowering uncertainties (see Sect. 5.1.7) by digitizing images with 10- or 12-bit resolution CCDs with correspondingly less noise. Also, a study of all of the applicable color spaces towards liquid crystal calibration would help identify the optimum color space for use with DPIT/V. Equally important, velocimetry can be improved by implementation of deformation methods (Scarano and Riethmuller 2000; Scarano 2002). Lastly, DPIT/V's three-dimensional implementation is relatively new with only several investigations accomplished to date, making this aspect of DPIT/V open to further development as well as

furthering scientific understanding of three-dimensional flows.

References

Abu Talib AR, Neely AJ, Ireland PT, Mullender AJ (2004) A novel liquid crystal image processing technique using multiple gas temperature steps to determine heat transfer coefficient distribution and adiabatic wall temperature. ASME J Turbomach 126:587–596

Adams JE, Haas W, Wysocki J (1969) Optical properties of certain cholesteric liquid-crystal films. J Chem Phys 50(6):2458–2464

Adrian RJ (1983) Laser velocimetry. In: Goldstein RJ (ed) Fluid mechanics measurements. Hemisphere, Washington, pp 155–244

Adrian RJ (1984) Scattering particle characteristics and their effect on pulsed laser measurements of fluid flow: speckle velocimetry vs particle image velocimetry. Appl Opt 23:1690–1691

Adrian RJ (1988) Statistical properties of particle image velocimetry measurements in turbulent flow. In: Adrian RJ, Durao DFG, Durst F, Heitor MV, Maeda M, Whitelaw JH (eds) Laser anemometry in fluid mechanics. Springer, New York, pp 115–129

Adrian RJ (1991) Particle imaging techniques for experimental fluid mechanics. Ann Rev Fluid Mech 23:261–304A

Aeschliman DP, Croll RH, Kuntz DW (1995) Shear-stress-sensitive liquid crystals for hypersonic boundary-layer transition detection. J Spacecr Rockets 32:749–757

Ahn J, Jung IS, Lee JS (2003) Film cooling from two rows of holes with opposite orientation angles- injectant behavior and adiabatic film cooling effectiveness. Int J Heat Fluid Flow 24:91–99

Ahn J, Choi H, Lee JS (2005) Large eddy simulation of flow and heat transfer in a channel roughened by square or semicircle ribs. ASME J Turbomach 127:263–269

Ai D, Ding P-P, Chen P-H (2001) The selection criterion of injection temperature pair for transient liquid crystal thermography on film cooling measurements. Int J Heat Mass Transf 44:1389–1399

Akino N, Kunugi T, Ichimiya K, Mitsushiro K, Ueda M (1986a) Improved liquid crystal thermometry excluding human color sensation, parts I and II, Concept and calibration. In: Kim JH, Moffat RJ (eds) Pressure and temperature measurements, vol 58. ASME HTD, Anaheim, pp 57–68

Akino N, Kunugi T, Ichimiya K, Mitsushiro K, Ueda M (1986b) Improved liquid crystal thermometry excluding human color sensation, part II, applications to the determination of wall temperature distributions. In: Kim JH, Moffat RJ (eds) Pressure and temperature measurements, vol 58. ASME HTD, Anaheim, pp 63–68

Akino N, Kunugi T, Ichimiya K, Mitsushiro K, Ueda M (1989) Improved liquid-crystal thermometry excluding human color sensation. Trans ASME J Heat Transf 111:558–565

Akino N, Kunugi T, Ichimiya K, Ueda M, Kurosawa A (1987) Liquid crystal thermometry based on automatic color evaluation and applications to measure turbulent heat transfer. In: Hirata M, Kasagi N (eds) Second international symposium on transport phenomena in turbulent flows, Tokyo, Japan, pp 627–640

Anderson MR, Baughn JW (2005a) Liquid-crystal thermometry: illumination spectral effects. Part 1—experiments. J Heat Transf 127:581–587

Anderson MR, Baughn JW (2005b) Liquid-crystal thermometry: illumination spectral effects. Part 2—theory. J Heat Transf 127:588–596

Ardasheva MM, Ryzhkova MV (1978) The use of liquid crystals in an aerodynamic heating test. Fluid Mech Sov Res 6:128–136

Arjocu SC, Liburdy JA (2000) Identification of dominant heat transfer modes associated with the impingement of an elliptical jet array. ASME J Heat Transf 122:240–247

Ashforth-Frost S, Jambunathan K (1996a) Effect of nozzle geometry and semi-confinement on the potential core of a turbulent axisymmetric free jet. Int Comm Heat Mass Transf 23:155–162

Ashforth-Frost S, Jambunathan K (1996b) Numerical prediction of semi-confined jet impingement and comparison with experimental data. Int J Numer Methods Fluids 23:295–306

Ashforth-Frost S, Jambunathan K, Whitney CF, Ball SJ (1997) Heat transfer from a flat plate to a turbulent axisymmetric impinging jet. Proc Inst Mech Eng 211:167–172

Auton TR, Hunt JCE, Prud'homme M (1988) The force exerted on a body in inviscid unsteady non-uniform rotational flow. J Fluid Mech 197:241–257

Azad GS, Han J-C, Boyle RJ (2000a) Heat transfer and flow on the squealer tip of a gas turbine blade. J Turbomach 122:725–732

Azad GS, Huang YH, Han JC (2000b) Impingement heat transfer on dimpled surfaces using a transient liquid crystal technique. J Thermophys Heat Transf 14:186–193

Babinsky H, Edwards JA (1996) Automatic liquid crystal thermography for transient heat transfer measurements in hypersonic flow. Exp Fluids 21(4):227–236

Barlow DN, Kim YW, Florschuetz LW (1997) Transient liquid crystal technique for convective heat transfer on rough surfaces. J Turbomach 119:14–22

Baughn JW (1995) Liquid crystal methods for studying turbulent heat transfer. Int J Heat Fluid Flow 16:365–375

Baughn JW, Anderson MR, Mayhew JE, Wolf JD (1999) Hysteresis of thermochromic liquid crystal temperature measurement based on hue. Trans ASME J Heat Transf 121:1067–1072

Baughn JW, Ireland PT, Jones TV, Saniei N (1989) A comparison of the transient and heated-coating methods for the measurement of local heat transfer coefficients on a pin fin. ASME J Heat Transf 111:877–881

Behle M, Schulz K, Leiner W, Fiebig M (1996) Color-based image processing to measure local temperature distribution by wide-band liquid crystal thermography. Appl Sci Res 56:113–143

Berger-Schunn (1994) Practical Color Measurement: A primer for the beginner, a reminder for the expert. In: Goodman JW (ed) Wiley, New York

Berkooz G, Elezgaray J, Holmes P, Lumley J, Poje AC (1994) The proper orthogonal decomposition, wavelets and modal approaches to the dynamics of coherent structures in turbulence. Appl Sci Res 53:321–338

Berns RS (2000) Billmeyer and Saltzman's principles of color technology. Wiley, New York

Boree J (2003) Extended proper orthogonal decomposition: a tool to analyse correlated events in turbulent flows. Exp Fluids 35(2):188–192

Brown GL, Roshko A (1974) On density effects and large structure in turbulent mixing layers. J Fluid Mech 64:775–816

Bühler L, Erhard P, Günther G, Müller U, Zimmermann G (1987) Natural convection in vertical gaps heated at the lower side—an experimental an numerical study. In: Bau HM, Bertram LA, Lorpela SA (eds) Bifurcation phenomena in thermal processes and convections. ASME, HTD-vol 94/AMD-vol 89, pp 67–74

Buttsworth DR, Elston SJ, Jones TV (1998) Direct full surface skin friction measurement using nematic liquid crystal techniques. J Turbomach 120:847–853

Buttsworth DR, Elston SJ, Jones TV (2000) Skin friction measurements on reflective surfaces using nematic liquid crystal. Exp Fluids 28(1):64–73

Camci C, Kim K (1992) A new hue capturing techniques for the quantitative interpretation of liquid crystal images used in convective heat transfer studies. ASME J Turbomach 114:765–775

Camci C, Kim K, Hippensteele SA (1992) A new hue capturing technique for the quantitative interpretation of liquid crystal images used in convective heat transfer studies. J Turbomach 114:765–775

Camci C, Kim K, Hippensteele SA, Poinsatte PE (1993) Evaluation of a hue capturing based transient liquid-crystal method for high resolution mapping of convective heat-transfer on curved surfaces. J Heat Transf 115:311–318

Cavallero D, Tanda G (2002) An experimental investigation of forced convection heat transfer in channels with rib turbulators by means of liquid crystal thermography. Exp Therm Fluid Sci 26:115–121

Chambers AC, Gillespie DRH, Ireland PT, Dailey GM (2003) A novel transient liquid crystal technique to determine heat transfer coefficient distributions and adiabatic wall temperature in a three-temperature problem. J Turbomach 125:538–546

Chan TL (2001) Evaluation of viewing-angle effect on determination of local heat transfer coefficients on a curved surface using transient and heat-coating liquid-crystal methods. Exp Fluids 31(4):447–456

Chan TL, Ashforth-Frost S, Jambunathan K (2001) Calibrating for viewing angle effect during heat transfer measurements on a curved surface. Int J Heat Mass Transf 44:2209–2223

Chaudhari AM, Woudenberg TM, Albin M, Goodson KE (1998) Transient liquid crystal thermography of microfabricated PCR vessel arrays. J Microelectromech Syst 7:345–355

Chen P-H, Ding P-P, Ai D (2001) An improved data reduction method for transient liquid crystal thermography on film cooling measurements. Int J Heat Mass Transf 44:1379–1387

Chyu MK, Ding H, Downs JP, Soechting FO (1998) Determination of local heat transfer coefficient based on bulk mean temperature using a transient liquid crystals technique. Exp Therm Fluid Sci 18:142–149

Chyu MK, Yu Y, Ding H (1999) Heat transfer enhancement in rectangular channels with concavities. J Enhanc Heat Trans 6:429–439

Ciofalo M, Signorino M, Simiano M (2003) Tomographic particle-image velocimetry and thermometry in Rayleigh–Benard convection using suspended thermochromic liquid crystals and digital image processing. Exp Fluids 34(2):156–172

Collings PJ (2002) Liquid crystals: nature's delicate phase of matter. Princeton University Press, Princeton

Cooper TE, Field RJ, Meyer JF (1975) Liquid crystal thermography and its application to the study of convective heat transfer. ASME J Heat Transf 97:442–450

Critoph RE, Holland MK, Fisher M (1999) Comparison of steady state and transient methods for measurement of local heat transfer in plate fin-tube heat exchangers using liquid crystal thermography with radiant heating. Int J Heat Mass Transf 42:1–12

Csendes A, Szekely V, Rencz M (1996) Thermal mapping with liquid crystal method. Microelectron Eng 31:281–290

Dabiri D (1992) The effect of forced boundary conditions on the flow field of a square convection cell. PhD thesis, University of California, San Diego

Dabiri D, Gharib M (1996) The effects of forced boundary conditions on flow within a cubic cavity using digital particle image thermometry and velocimetry (DPITV). Exp Therm Fluid Sci 13:349–363

Dabiri D, Gharib M (1991a) Digital particle image thermometry: the method and implementation. Exp Fluids 11(2–3):77–86

Dabiri D, Gharib M (1991b) Digital particle image thermometry and its application to a heated vortex-ring. In: Applications of laser anemometry to fluid mechanics. Fifth international symposium on application of laser techniques to fluid mechanics, Lisbon, Portugal, July 9–12, pp 81–101

Dabiri D, Gharib M (1995) Digital particle image thermometry and velocimetry. In: Flow visualization VII, proceedings of the seventh international symposium on flow visualization, 11–14 September, pp 558–563

Dano BPE, Liburdy JA, Kanokjaruvijit K (2005) Flow characteristics and heat transfer performances of a semiconfined impinging array of jets-effect of nozzle geometry. Int J Heat Mass Transf 48:691–701

Das MK, Tariq A, Panigrahi PK, Muralidhar K (2005) Estimation of convective heat transfer coefficient from transient liquid crystal data using an inverse technique. Inverse Probl Sci Eng 13:133–155

de Vries (1951) Rotatory power and other optical properties of certain liquid crystals. Acta Crystallogr 4:219–226

Delville J, Bonnet JP (2001) Review of coherent structures in turbulent free shear flows and their possible influence on computational methods. Flow Turbul Combust 66:333–353

Demus D, Chemie S (1990) Types and classification of liquid crystals. In: Bahadur B (ed) Liquid crystals, applications and uses, vol 1. World Scientific, New Jersey, pp 1–36

Drost U, Bolcs A (1999) Investigation of detailed film cooling effectiveness and heat transfer distributions on a gas turbine airfoil. J Turbomach 121:233–242

Dukle NM, Hollingsworth DK (1996a) Liquid crystal images of the transition from jet impingement convection to nucleate boiling part I: Monotonic distribution of the convection coefficient. Exp Therm Fluid Sci 12:274–287

Dukle NM, Hollingsworth DK (1996b) Liquid crystal images of the transition from jet impingement convection to nucleate boiling part II: nonmonotonic distribution of the convection coefficient. Exp Therm Fluid Sci 12:288–297

Du H, Ekkad S, Han JC (1997) Effect of unsteady wake with trailing edge coolant ejection on detailed heat transfer coefficient distributions for a gas turbine blade. J Heat Transf 119:242–248

Du H, Ekkad S, Han JC (1999) Effect of unsteady wake with trailing edge coolant ejection on film cooling performance for a gas turbine blade. J Turbomach 121:448–455

Ekkad SV, Han J-C (1996) Heat transfer inside and downstream of cavities using transient liquid crystal method. J Thermophys Heat Transf 10:511–516

Ekkad SV, Han J-C (1999) Heat transfer distributions on a cylinder with simulated thermal barrier coating spallation. J Thermophys Heat Transf 13:76–81

Ekkad SV, Han J-C (2000a) A transient liquid crystal thermography technique for gas turbine heat transfer measurements. Meas Sci Technol 11:957–968

Ekkad SV, Han J-C (2000b) Film cooling measurements on cylindrical models with simulated thermal barrier coating spallation. J Thermophys Heat Transf 14:194–200

Ekkad SV, Han JC, Du H (1998) Detailed film cooling measurements on a cylindrical leading edge model: Effect of free-stream turbulence and coolant density. J Turbomach 120:799–807

Ekkad SV, Huang YZ, Han JC (1999) Impingement heat transfer on a target plate with film cooling holes. Thermophys Heat Transf 13:522–528

Ekkad SV, Pamela G, Acharya S (2000) Influence of crossflow-induced swirl and impingement on heat transfer in an internal coolant passage of a turbine airfoil. J Heat Transf 122:587–597

Ekkad SV, Zapata D, Han C (1997) Film effectiveness over a flat surface with air and CO_2 injection through compound angle holes using a transient liquid crystal image method. J Turbomach 199:587–593

El-Gabry LA, Kaminski DA (2005) Experimental investigation of local heat transfer distribution on smooth and roughened surfaces under an array of angled impinging jets. ASME J Turbomach 127:532–544

Elser W, Ennulat RD (1976) Selective reflection of cholesteric liquid crystals. In: Brown G (ed) Advances in liquid crystals, vol 2. Academic Press, New York, pp 73–172

Engels G, Peck RE, Kim Y (2001) Investigation of a quasi-steady liquid crystal technique for film cooling heat transfer measurements. Exp Heat Transf 14:181–198

Facchini B, Innocenti L, Surace M (2006) Design criteria for ribbed channels—experimental investigation and theoretical analysis. Int J Heat Mass Transf 40:3130–3141

Facchini B, Surace M (2006) Impingement cooling for modern combustors: experimental analysis of heat transfer and effectiveness. Exp Fluids 40(4):601–611

Farina DJ, Hacker JM, Moffat RJ, Eaton JK (1994) Illuminant invariant calibration of thermochromic liquid crystal. Exp Therm Fluid Sci 9:1–12

Fergason JL (1964) Liquid Crystals. Scientific American 211:77–85

Fergason JL (1966) Cholesteric structure—I optical properties. Molec Cryst 1:293–307

Fergason JL (1968) Liquid crystals in nondestructive testing. Appl Opt 7:1729–1737

Foley JD, van Dam A, Feiner SK, Hughes JF (1996) Computer graphics: principles and practice. In: Gordon PS (ed) Addison-Wesley, New York

Freidel G (1922) Les etats mesomorphes de la matiere. Annales de Physique 18:273–474

Frey H (1988) Digitale bildverarbeitung in farbräumen. PhD thesis, Technical University of Munich, Munich, Germany

Fujisawa N, Aoyama A, Kosaka S (2003) Measurement of shear-stress distribution over a surface by liquid-crystal coating. Meas Sci Technol 14:1655–1661

Fujisawa N, Adrian RJ (1999) Three-dimensional temperature measurement in turbulent thermal convection by extended range scanning liquid crystal thermometry. J Vis 1:355–364

Fujisawa N, Funatani S (2000) Simultaneous measurement of temperature and velocity in a turbulent thermal convection by the extended range scanning liquid crystal visualization technique. Exp Fluids 29:s158–s165

Fujisawa N, Hashizume Y (2001) An uncertainty analysis of temperature and velocity measured by a liquid crystal visualization technique. Meas Sci Technol 12:1235–1242

Fujisawa N, Nakajima T, Katoh N, Hashizume Y (2004) An uncertainty analysis of temperature and velocity measured by stereo liquid-crystal thermometry and velocimetry. Meas Sci Technol 15:799–806

Fujisawa N, Funatani S, Katoh N (2005) Scanning liquid-crystal thermometry and stereo velocimetry for simultaneous three-dimensional measurement of temperature and velocity field in a turbulent Rayleigh–Benard convection. Exp Fluids 38(3):291–303

Fujisawa N, Watanabe M, Hashizume Y (2008) Visualization of turbulence structure in unsteady non-penetrative thermal convection using liquid crystal thermometry and stereo velocimetry. J Vis 11:173–180

Funatani S, Fujisawa N (2002) Simultaneous measurement of temperature and three velocity components in planar cross section by liquid-crystal thermometry combined with stereoscopic particle image velocimetry. Meas Sci Technol 13:1197–1205

Funatani S, Fujisawa N, Matsuura T (2000) Multi-point calibration technique of liquid crystal thermometry and its application to three-dimensional temperature measurement of thermal convection. J Flow Vis Image Process 7:353–366

Gao X, Sundén B (2001) Heat transfer and pressure drop measurements in rib-roughened rectangular ducts. Exp Therm Fluid Sci 24:25–34

Geers LFG, Hanjalic K, Tummers MJ (2006) Wall imprint of turbulent structures and heat transfer in multiple impinging jet arrays. J Fluid Mech 546:255–284

Gennes PG, Prost J (1993) The physics of liquid crystals. Oxford University Press, New York

Gharib M, Dabiri D (2000) Digital particle image velocimetry. In: Smits AJ, Lim TT (eds) Flow visualization, techniques and examples. Imperial College Press, Singapore

Gleeson HF, Coles HJ (1989) Optical properties of chiral nematic liquid crystals. Mol Cryst Liquid Cryst 170:9–34

Grant I (1994) Selected papers on particle image velocimetry In: Grant I (ed) SPIE milestone series, vol MS 99. SPIE Optical Engineering Press, Bellingham

Grassi W, Testi D, Della Vista D, Torelli G (2007) Calibration of a sheet of thermosensitive liquid crystals viewed orthogonally. Measurements 40:898–903

Grewal GS, Bharara M, Cobb JE, Dubey VN, Claremont DJ (2006) A novel approach to thermochromic liquid crystal calibration using neural networks. Meas Sci Technol 17:1918–1924

Guild J (1931) The colorimetric properties of the spectrum. Philos Trans R Soc Lond Ser A 230:149–187

Günther A, Rudolf von Rohr Ph (2002a) Influence of the optical configuration on temperature measurements with fluid-dispersed TLCs. Exp Fluids 33(5):920–930

Günther A, Rudolf von Rohr Ph (2002b) Structure of the temperature field in a flow over heated waves. Exp Fluids 33(6):920–930

Hacker JM, Eaton JK (1996) Measurements of heat transfer in a separated and reattaching flow with spatially varying thermal boundary conditions. Int J Heat Fluid Flow 18:131–141

Hay JL, Hollingsworth DK (1996) A comparison of trichromic systems for use in the calibration of polymer-dispersed thermochromic liquid crystals. Exp Therm Fluid Sci 12:1–12

Hay JL, Hollingsworth DK (1998) Calibration of micro-encapsulated liquid crystals using hue angle and a dimensionless temperature. Exp Therm Fluid Sci 18:251–257

Hiller WJ, Kowalewski TA (1986) Simultaneous measurement of temperature and velocity fields in thermal convective flows. In: Claude Veret (ed) Flow visualization IV, proceedings of the 4th international symposium on flow visualization, 26–29 August, Paris, France. Hemisphere, New York, pp 617–622

Hiller WJ, Koch ST, Kowalewski TA (1989a) Three-dimensional structures in laminar natural convection in a cubic enclosure. Exp Therm Fluid Sci 2:34–44

Hiller WJ, Koch ST, Kowalewski TA, De Vahl Davis G, Behnia M (1989b) Experimental and numerical investigation of natural convection in a cube with two heated side walls. In: Moffatt HK, Tsinober A (eds) Topological fluid mechanics, proceedings of the IUTAM symposium, 13–18 August. Cambridge University Press, Cambridge, pp 717–727

Hiller WJ, Koch ST, Kowalewski TA, Range K (1991) Visualization of 3-D convection—comparison with numerical results. In: Esp. da Revista Brasileira de Ciencias Mecanicas (ed) 11th ABCM mechanical engineering conference, 11–13 December, Sao Paulo, Brazil, vol 2, pp 21–24

Hiller WJ, Koch ST, Kowalewski TA, Stella F (1993) Onset of natural convection in a cube. Int J Heat Mass Transf 36:3251–3263

Hjelmfelt AT, Mockros LF (1966) Motion of discrete particles in a turbulent fluid. Appl Sci Res 16:149–161

Hoffs A, Bolcs A, Harasgama SP (1997) Transient heat transfer experiments in a linear cascade via an insertion mechanism using the liquid crystal technique. J Turbomach 199:9–13

Hollingsworth DK, Boehman AL, Smith EG, Moffat RJ (1989) Measurement of temperature and heat transfer coefficient distributions in a complex flow using liquid crystal thermography and true-color image processing. In: ASME collected papers in heat transfer, HTD-vol 123, Winter annual meeting of ASME, San Francisco, 10–15 December. ASME, New York, pp 35–42

Holmes BJ, Obara CJ (1987) Advances in flow visualization using liquid crystal coatings. SAE technical paper 871017

Hu H, Koochesfahani MM (2006) Molecular tagging velocimetry and thermometry and its application to the wake of a heated circular cylinder. Meas Sci Technol 17:1269–1281

Hu SH, Richards CD, Richards RF (1994) Thermography of atomized fropelts in flight using thermochromic liquid crystals. In: 8th Annual ICASS conference of liquid atomization and spray systems, Belleve WA

Huang YZ, Ekkad SV, Han JC (1998) Detailed heat transfer distributions under an array of orthogonal impinging jets. J Thermophys Heat Transf 12:73–79

Hwang J-J, Cheng C-S (1999) Augmented heat transfer in a triangular duct by using multiple swirling jets. J Heat Trans 121:683–690

Hwang J-J, Chang B-Y (2000) Effect of outflow orientation on heat transfer and pressure drop in a triangular duct with an array of tangential jets. J Heat Trans 122:669–678

Hwang J-J, Cheng C-S (2001) Impingement cooling in triangular ducts using an array of side-entry wall jets. Int Heat Mass Transf 44:1053–1063

Hwang J-J, Lui C-C (1999) Detailed heat transfer characteristic comparison in straight and 90-deg turned trapezoidal ducts with pin-fin arrays. Int J Heat Mass Transf 42:4005–4016

Iles A, Fortt R, de Mello AJ (2005) Thermal optimisation of the Reimer–Tiemann reaction using thermochromic liquid crystals on a microfluidic reactor. Lab Chip 5:540–544

Ireland PT, Jones TV (1987) The response time of a surface thermometer employing encapsulated thermochromic liquid crystals. J Phys E Sci Instrum 20:1195–1199

Ireland PT, Jones TV (2000) Liquid crystal measurements of heat transfer and surface shear stress. Meas Sci Tech 11:969–986

Ireland PT, Neely AJ, Gillespie DRH, Robertson AJ (1999) Turbulent heat transfer measurements using liquid crystals. Int J Heat Fluid Flow 20:355–367

Jain AK (1989) Fundamentals of digital image processing. In: Kailath T (ed) Prentice-Hall, New Jersey

Javitt NB (2002) Cholesterol, hydroxycholesterols, and bile acids. Biochem Biophys Res Commun 292(5):1147–1153

Jeng T-M, Wang M-P, Hwang G-J, Hung Y-H (2004) A new semi-empirical model for predicting heat transfer characteristics in porous channels. Exp Therm Fluid Sci 29:9–21

Jeschke P, Biertümpfel R, Beer H (2000) Liquid-crystal thermography for heat-transfer measurements in the presence of longitudinal vortices in a natural convection flow. Meas Sci Technol 11:447–453

Jung IS, Lee JS (2000) Effects of orientation angles on film cooling over a flat plate—boundary layer temperature distributions and adiabatic film cooling effectiveness. ASME J Turbomach 122:153–160

Kahn FJ (1982) The molecular physics of liquid-crystal devices. Phys Today 35(5):66–74

Kaiser E (2001) Measurement and visualization of impingement cooling in narrow channels. Exp Fluids 30(6):603–612

Kasagi N, Hirata M, Kumada M (1981) Studies of full-converge film cooling: part 1, cooling effectiveness of thermally conductive wall. ASME paper no. 81-GT-37

Kassab AJ, Divo E, Kapat JS (2001) Multi-dimensional heat flux reconstruction using narrow-band thermochromic liquid crystal thermography. Inverse Probl Eng 9:537–559

Kawamoto H (2002) The history of liquid-crystal displays. Proc IEEE 90(4):460–500

Keane RD, Adrian RJ (1992) Theory of cross-correlation analysis of PIV images. Appl Sci Res 49:191–215

Kenning BDR, Yan YY (1996) Pool boiling heat transfer on a thin plate: features revealed by liquid crystal thermography. Int J Heat Mass Transf 39:3117–3137

Kenning DBR, Kono T, Wienecke M (2001) Investigation of boiling heat transfer by liquid crystal thermography. Exp Therm Fluid Sci 25:219–229

Keyes PH, Weston HT, Daniels WB (1973) Tricritical behavior in a liquid-crystal system. Phys Rev Lett 31:628–630

Kim K, Camci C (1995a) Fluid-dynamic and convective heat-transfer in impinging jets through implementation of a high-resolution liquid-crystal technique. 1 Flow and heat-transfer experiments. Int J Turbo Jet Eng 12(1):1–12

Kim K, Camci C (1995b) Fluid-dynamic and convective heat-transfer in impinging jets through implementation of a high-resolution liquid-crystal technique. 2. Navier-stokes computation of impulsively starting heat-transfer experiments. Int J Turbo Jet Eng 12(1):13–19

Kim T, Hodson HP, Lu TJ (2005) Contribution of vortex structures and flow separation to local and overall pressure and heat transfer characteristics in an ultralightweight lattice material. Int J Heat Mass Transf 48:4243–4264

Kimura I, Hyodo T, Ozawa M (1998) Temperature and velocity measurement of a 3D thermal flow field using thermo-sensitive liquid crystals. J Vis 1:145–152

Kimura I, Takamori T, Ozawa M, Takenaka N, Sakaguchi T (1989a) Simultaneous measurement of flow and temperature fields based on color image information. In: Flow visualization V, proceedings of the fifth international symposium on flow visualization, August 21–25, Prague, Czechoslovakia, pp 29–34

Kimura I, Takamori T, Ozawa M, Takenaka N, Manabe Y (1989b) Quantitative thermal flow visualization using color image processing (application to a natural convection visualized by liquid crystals). In: Khalighi B, Brown MJ, Freitas CJ (eds) Flow visualization, vol 85. ASME-FED, pp 261–269

Kingsley-Rowe JR, Lock GD, Owen JM (2005) Transient heat transfer measurements using thermochromic liquid crystal—lateral-conduction error. Int J Heat Fluid Flow 26:256–263

Kitamura K, Kimura F (1995) Heat transfer and fluid flow of natural convection adjacent to upward-facing horizontal plates. Int J Heat Mass Transf 38:3149–3159

Klein EJ (1968a) Liquid crystals in aerodynamic testing. Aeronaut Astronaut 6(7):70–73

Klein EJ (1968b) Application of liquid crystals to boundary-layer flow visualization. AIAA paper, 68-376

Klein EJ, Margozzi AP (1970) Apparatus for the calibration of shear-sensitive liquid crystals. Rev Sci Instrum 41:238–239

Kobayashi T, Saga T, Foeg-Hee D (1998) Time response characteristics of microcapsulated liquid-crystal particles. Heat Transf Jpn Res 27:298–390

Kodzwa PM, Eaton JK (2007) Angular effects on thermochromic liquid crystal thermography. Exp Fluids 43(6):929–937

Kodzwa PM, Elkins CJ, Mukerji D, Eaton J (2007) Thermochromic liquid crystal temperature measurements through a borescope imaging system. Exp Fluids 43(4):475–486

Kowalewski TA (2002) Particle image velocimetry and thermometry for two-phase flow problems. Ann NY Acad Sci 972:213–222

Kowalewski TA (1999) Particle image velocimetry and thermometry using liquid crystals. In: 8me colloque nationale de visualisation et de traitment d'images en mecanique des fluides, 1–4 June, ENSICA, Toulouse, France, pp 33–48

Kowalewski TA (2001) Particle image velocimetry and thermometry using liquid crystals tracers. In: Kompemhans J (ed) PIV'01 4th international symposium on particle image velocimetry, DLR, Mitteilung, Göttingen, pp 1134.1–1134.10

Kowalewski TA, Rebow M (1999) Freezing of water in a differentially heated cubic cavity. Int J Comp Fluid Dyn 11:193–210

Kowalewski TA, Ligrani P, Dreizler A, Schulz C, Fey U, Egami Y (2007) Temperature and heat flux. In: Tropea C, Yarin AL, Foss JF (eds) Springer handbook of experimental fluid mechanics, 1st edn. Springer, Berlin, pp 487–561

Kukreja RT, Lau SC (1998) Distributions of local heat transfer coefficient on surfaces with solid and perforated ribs. Enhanc Heat Transf 5:9–21

Lakshminarasimhan MS, Lu Q, Chin Y, Hollingsworth DK, Witte LC (2005) Fully developed nucleate boiling in narrow vertical channels. J Heat Transf 127:941–944

Lee J, Lee S-J (1999) Stagnation region heat transfer of a turbulent axisymmetric jet impingement. Exp Heat Transf 12:137–156

Lee J, Lee S-J (2000) The effect of nozzle aspect ratio on stagnation region heat transfer characteristics of elliptic impinging jet. Int J Heat Mass Transf 43:555–575

Lee DH, Chung JH, Won SY, Kim YT, Boo KS (2000) A new liquid crystal color calibration technique using neural networks and median filtering. KSME Int 14(1):113–120

Lee JS, Jung HG, Kang SB (2002) Effect of embedded vortices on film cooling performance on a flat plate. Exp Therm Fluid Sci 26:197–204

Lehmann O (1889) Über fliessende krystalle. Z Phys Chem 4:462–472

Lemburg R (1971) Liquid crystal for the visualization of unsteady boundary layers. In: Third Canadian congress of applied mechanics, Calgary, pp 525–526

Li H, Xing C, Braun MJ (2007) Natural convection in a bottom-heated top-cooled cubic cavity with a baffle at the median height: experiment and model validation. Exp Fluids 43(9):895–905

Lighthill J (1978) Waves in fluids. Cambridge University Press, Cambridge

Ling JPC, Ireland PT, Turner L (2004) A technique for processing transient heat transfer, liquid crystal experiments in the presence of lateral conduction. J Turbomach 126:247–258

Liou T-M, Chen C-C, Tsai T-W (2000a) Heat transfer and fluid flow in a square duct with 12 different shaped vortex generators. ASME J Heat Transf 122:327–335

Liou T-M, Chen C-C, Tzeng Y-Y, Tsai T-W (2000b) Nonintrusive measurements of near-wall fluid flow and surface heat transfer in a serpentine passage. Int J Heat Mass Transf 43:3233–3244

Liou T-M, Chen C-C, Chen M-Y (2001) TLCT and LDV measurements of heat transfer and fluid flow in a rotating sharp turning duct. Int J Heat Mass Transf 44:1777–1787

Liou T-M, Chen M-Y, Wang Y-M (2003) Heat transfer, fluid flow, and pressure measurements inside a rotating two-pass duct with detached 90-deg ribs. ASME J Turbomach 125:565–574

Litster JD, Birgeneau RJ (1982) Phases and phase transition. Phys Today 35(5):26–33

Lock GD, Wilson M, Owen JM (2005a) Influence of fluid dynamics on heat transfer in a preswirl rotating-disk system. ASME J Eng Gas Turbine Power 127:791–797

Lock GD, Yan Y, Newton PJ, Wilson M, Owen JM (2005b) Heat transfer measurements using liquid crystals in a preswirl rotating-disk system. ASME J Eng Gas Turbine Power 127:375–382

Loebisch L (1872) Berichte der Deutschen Chemischen Gesellschaft 5:510–514

Lourenco LM, Krothapalli A, Smith CA (1989) Particle image velocimetry. In: Gad-El-Hak M (ed) Advances in fluid mechanics measurements. Springer, Berlin, pp 128–199

Lumley JL (1970) Stochastic tools in turbulence. Academic Press, New York

Lutjen PM, Mishra D, Prasad V (2001) Three-dimensional visualization and measurement of temperature field using liquid crystal scanning thermography. J Heat Transf 123:1006–1014

Ma X, Karniadakis GE, Park H, Gharib M (2002) DPIV/T-driven convective heat transfer simulation. Int J Heat Mass Transf 45:3517–3527

Ma X, Karniadakis GE, Park H, Gharib M (2003) DPIV-driven flow simulation: a new computational paradigm. Proc R Soc Lond A 459:547–565

Maier A, Sheldrae TH, Wilcock D (2000a) Geometric parameters influencing flow in an axisymmetric IC engine inlet port assembly: part I—valve flow characteristics. J Fluid Eng 122:650–657

Maier A, Sheldrae TH, Wilcock D (2000b) Geometric parameters influencing flow in an axisymmetric IC engine inlet port assembly: Part II—parametric variation of valve geometry. J Fluid Eng 122:658–665

Makow DM (1980) Peak reflectance ad color gamut of superimposed left- and right-handed cholesteric liquid crystals. Appl Opt 19:1274–1277

Makow D (1991) Liquid crystals in decorative and visual arts. In: Bahadur B (ed) Liquid crystals, applications and uses, vol 2. World Scientific, New Jersey, pp 121–156

Makow DM, Sanders CL (1978) Additive colour properties and colour gamut of cholesteric liquid crystals. Nature 276(5683):48–50

Martinez-Botas RF, Lock GD, Jones TV (1995) Heat-transfer measurements in an annular cascade of transonic gas-turbine blades using the transient liquid-crystal technique. J Turbomach 117:425–431

Mathieu J (1911) J Bull Soc Trans Min 34:13

Matsuda H, Ikeda K, Nakata Y, Otomo F, Takeo S, Fukuyama Y (2000) A new thermochromic liquid crystal temperature identification technique using color space interpolations and its application to film cooling effectiveness measurements. J Flow Vis Image Process 7:103–121

Maxey MR (1987) The motion of a small rigid sphere in a non-uniform flow. Phys Fluids 30:1579–1582

Maxey MR, Riley JJ (1983) Equation of motion for a small rigid sphere in a nonuniform flow. Phys Fluids 26:863–889

Maxwell JC (1855) Experiments on colour, perceived by the eye, with remarks on colour-blindness. T Roy Soc Edin 24(2):275–298

Maxwell JC (1965) Scientific papers of James Clerk Maxwell. In: Nevern WD (ed) The Scientific papers of James Clerk Maxwell, vol 1&2. Dover, New York

Mayhew JE, Baughn JW, Byerley AR (2003) The effect of freestream turbulence on film cooling adiabatic effectiveness. Int J Heat Fluid Flow 24:669–679

McDonnell DG (1987) Thermochromic cholesteric liquid crystals. In: Gray GW (ed) Thermotropic liquid crystals, vol 22. Wiley, London, pp 120–144

Mckeon BJ, Comte-Bellot G, Foss JF, Westerweeel J, Scarano F, Tropea C, Meyers JF, Lee JW, Cavone AA, Schodl R, Koochesfahani MM, Nocera DG, Andreopoulos Y, Dahm WJA, Mullin JA, Wallace JM, Vukoslavcevic PV, Morris SC, Pardyjak ER, Cuerva A (2007) Velocity, vorticity, and Mach number. In: Tropea C, Yarin AL, Foss JF (eds) Springer handbook of experimental fluid mechanics, 1st edn. Springer, Berlin, pp 215–471

Mei R (1996) Velocity fidelity of flow tracer particles. Exp Fluids 22:1–13

Meinders ER, Van Der Meer TH, Hanjalic K (1998) Local convective heat transfer from an array of wall-mounted cubes. Int J Heat Mass Transf 41:335–346

Melling A (1997) Tracer particles and seeding for particle image velocimetry. Meas Sci Technol 8(12):1406–1416

Metzger DE, Bunker RS, Bosch G (1991) Transient liquid-crystal measurement of local heat-transfer on a rotating disk with jet impingement. J Turbomach 113:52–59

Mikhailov MD (2003) Evaluating convective heat transfer coefficients from a given set of data by using mathematica. Commun Numer Methods Eng 19:441–443

Mishra D, Lutjen PM, Chen QS, Prasad V (2000) Tomographic reconstruction of three-dimensional temperature field using liquid crystal scanning thermography. Exp Heat Transf 13(4):235–258

Mitchell BS (2004) An introduction to materials engineering and science for chemical and materials engineers. Wiley, New Jersey

Mochizuki T, Nozaki T, Mori YH, Kaji N (1999) Heat transfer to liquid drops passing through an immiscible liquid medium between tilted parallel-plate electrodes. Int J Heat Mass Transf 42:311–3129

Moffat RJ (1990) Some experimental methods for heat transfer studies. Exp Therm Fluid Sci 3:14–32

Moon HK, O'Connell T, Sharma R (2003) Heat transfer enhancement using a convex-patterned surface. ASME J Turbomach 125:274–280

Muwanga R, Hassan I (2006a) Local heat transfer measurements in microchannels using liquid crystal thermography: methodology development and validation. ASME J Heat Transf 128:617–626

Muwanga R, Hassan I (2006b) Local heat transfer measurements on a curved microsurface using liquid crystal thermography. J Thermophys Heat Transf 20:884–894

Muwanga R, Hassan I (2007) A flow boiling heat transfer investigation of FC-72 in a microtube using liquid crystal thermography. J Heat Transf 129:977–987

Nakano T, Fujisawa N (2006) Wind tunnel testing of shear-stress measurement by liquid-crystal coating. J Vis 9:135–136

Neely AJ, Ireland PT, Harper LR (1997) Extended surface convective cooling studies of engine components using the transient liquid crystal technique. Proc Inst Mech Eng 211:273–287

Newton PJ, Lock GD, Krishnababu SK, Hodson HP, Dawes WN, Hannis J, Whitney C (2006) Heat transfer and aerodynamics of turbine blade tips in a linear cascade. ASME J Turbomach 128:300–309

Newton PJ, Yan Y, Stevens NE, Evatt ST, Lock GD, Owen JM (2003a) Transient heat transfer measurements using thermochromic liquid crystal. Part 1—an improved technique. Int J Heat Fluid Flow 24(1):14–22

Newton PJ, Yan Y, Stevens NE, Evatt ST, Lock GD, Owen JM (2003b) Transient heat transfer measurements using thermochromic liquid crystal. Part 2—experimental uncertainties. Int J Heat Fluid Flow 24(1):23–28

Noh J, Sung SW, Jeon MK, Kim SH, Lee LP, Woo SI (2005) In situ thermal diagnostics of the micro-PCR system using liquid crystals. Sens Actuators 122:196–202

Nozaki T, Mochizuki T, Kaji N, Mory YH (1995) Application of liquid-crystal thermometry to drop temperature measurements. Exp Fluids 18:137–144

O'Brien S, Zhong S (2001) Visualisation of flow separation with shear-sensitive liquid crystals. Aeronaut J 105:597–602

Ochoa AD, Baughn JW, Byerley AR (2005) A new technique for dynamic heat transfer measurements and flow visualization using liquid crystal thermography. Int J Heat Fluid Flow 26:264–275

Ogden TR, Hendricks EW (1984) Liquid crystal thermography in water tunnels. Exp Fluids 2:65–66

Onbasioglu & Onbasioglu (2003) On enhancement of heat transfer with ribs. Appl Therm Eng 24:43–57

Oseen CW (1933) The theory of liquid crystals. Trans Faraday Soc 29:883–900

Owen JM, Newton PJ, Lock GD (2003) Transient heat transfer measurements using thermochromic liquid crystal. Part 1: an improved technique. Int J Heat Fluid Flow 24(1):14–22

Ozawa M, Müller U, Kimura I, Takamori T (1992) Flow and temperature measurement of natural convection in a Hele-Shaw cell using a thermo-sensitive liquid-crystal tracer. Exp Fluids 12:213–222

Park HG (1998) A study of heat transport processes in the wake of a stationary and oscillating circular cylinder using digital particle

image velocimetry/thermometry. PhD thesis, California Institute of Technology, Pasadena, CA, USA

Park HG, Gharib M (2001) Experimental study of heat convection from stationary and oscillating circular cylinder in cross flow. J Heat Transf 123:51–62

Park HG, Dabiri D, Gharib M (2001) Digital particle image velocimetry/thermometry and application to the wake of a heated circular cylinder. Exp Fluids 30:327–338

Parsley M (1991) The Hallcrest handbook of thermochromic liquid crystal technology. Hallcrest, Glenview

Pehl M, Werner F, Degado A (2000) First visualization of temperature fields in liquids at high pressure using thermochromic liquid crystals. Exp Fluids 29:302–304

Pershan PS (1982) Lyotropic liquid crystal. Phys Today 35(5):34–39

Platzer K-H, Hirsch C, Metzger DE, Wittig S (1992) Computer-based areal surface temperature and local heat transfer measurements with thermochromic liquid crystals (TLC). Exp Fluids 13:26–32

Pohl L, Finkenzeller U (1990) Physical properties of liquid crystals. In: Bahadur B (ed) Liquid crystals, applications and uses, vol 1. World Scientific, New Jersey, pp 139–170

Poje AC, Lumley JL (1995) A model for large-scale structures in turbulent shear flows. J Fluid Mech 285:349–369

Pollmann P, Stegemeyer H (1974) Influence of all-round pressure on structure of cholesteric mesophases. Berichte Der Bunsen-Gesellschaft-Physical Chemistry Chemical Physics 78:843–848

Pottebaum TS, Gharib M (2004) The pinch-off process in a starting buoyant plume. Exp Fluids 37:87–94

Pottebaum TS, Gharib M (2006) Using oscillations to enhance heat transfer for a circular cylinder. Int J Heat Mass Transf 49:3190–3210

Pradeep AM, Sullerey RK (2004) Detection of separation in S-duct diffusers using shear sensitive liquid crystals. J Vis 7:299–307

Praisner TJ, Smith CR (2006a) The dynamics of the horseshoe vortex and associated endwall heat transfer: part I—temporal behavior. J Turbomachinery 128:747–754

Praisner TJ, Smith CR (2006b) The dynamics of the horseshoe vortex and associated endwall heat transfer—part II- time-mean results. J Turbomach 128:755–762

Praisner TJ, Sabatini DR, Smith CR (2001) Simultaneously combined liquid crystal surface heat transfer and PIV flow-field measurements. Exp Fluids 30:1–10

Prandtl L, Tietjens OG (1934) Applied hydro- and aeromechanics. McGraw-Hill, New York

Prasad AK (2000) Stereoscopic particle image velocimetry. Exp Fluids 29:103–116

Pratt WK (1991) Digital image processing. Wiley, New York

Raffel M, Willert M, Kompenhans J (1998) Particle image velocimetry, a practical guide. Springer, Berlin

Rangel RH, Coimbra CFM (1998) General solution of the particle momentum equation in unsteady Stokes flows. J Fluid Mech 370:53–72

Rayman B (1887) Contribution à l'histoire de la cholestérine. Bulletin de la Société Chimique de France, Nouvelle Série 47:898–901

Reda DC, Aeschliman DP (1992) Liquid-crystal coatings for surface shear-stress visualization in hypersonic flows. AIAA J 29:155–158

Reda DC, Muratore JJ (1994) Measurement of surface shear stress vectors using liquid crystal coatings. AIAA J 32:1576–1582

Reda DC, Wilder MC (1992) Liquid crystal coatings for surface shear-stress visualization in hypersonic flows. J Spacecr Rockets 29:155–158

Reda DC, Wilder MC (2001) Shear-sensitive liquid crystal coating method applied through transparent test surfaces. AIAA J 39:195–197

Reda DC, Muratore JJ, Heineck T (1994) Time and flow-direction responses of shear-stress-sensitive liquid crystal coatings. AIAA J 32:693–700

Reda DC, Wilder MC, Crowder JP (1997a) Simultaneous, full-surface visualizations of transition and separation using liquid crystal coatings. AIAA J 35:615–616

Reda DC, Wilder MC, Farina DJ, Zilliac G (1997b) New methodology for the measurement of surface shear stress vector distributions. AIAA J 4:608–614

Reda DC, Wilder MC, Mehta RD, Zilliac G (1998) Measurement of continuous pressure and shear distributions using coating and imaging techniques. AIAA J 36:895–899

Reinitzer F (1888) Beiträge zur kenntniss des cholesterins. Wiener Monatschr Für Chem 9:421–441

Richards CD, Richards RF (1998) Transient temperature measurements in a convectively cooled droplet. Exp Fluids 25:392–400

Roberts GT, East RA (1996) Liquid crystal thermography for heat transfer measurement in hypersonic flows: a review. J Spacecr Rockets 33:761–768

Roesgen T, Totaro R (2002) A statistical calibration technique for thermochromic liquid crystals. Exp Fluids 33:732–734

Roshko A (1993) Perspectives on bluff body aerodynamics. J Wind Eng Ind Aerodyn 49:79–100

Rossotti H (1983) Colour, why the world isn't gray. Princeton University Press, Princeton

Roth TB, Anderson AM (2007) The effects of film thickness, light polarization and light intensity on the light transmission characteristics of thermochromic liquid crystal. ASME J Heat Transf 129:372–378

Russ JC (2002) The image processing handbook. CRC, Boca Raton

Sabatino D, Smith CR (2002) Simultaneous velocity-surface heat transfer behavior of turbulent spots. Exp Fluids 33:13–21

Sabatino DR, Praisner TJ, Smith CR (2000) A high-accuracy calibration technique for thermochromic liquid crystal temperature measurements. Exp Fluids 28:497–505

Sage I (1990) Thermochromic liquid crystals in devices. In: Bahadur B (ed) Liquid crystals, applications and uses, vol 3. World Scientific, New Jersey, pp 301–341

Samulski ET (1982) Polymeric liquid crystal. Phys Today 35(5):40–46

Saniei N (2002) Liquid crystals and their application in heat transfer measurements. Heat Transfer Eng 23(4):1–2

Saniei N, Yan XJ (2000) An experimental study of heat transfer from a disk rotating in an infinite environment including heat transfer enhancement by jet impingement cooling. J Enhanc Heat Transf 7:231–245

Sargison JE, Oldfield MLG, Guo SM, Lock GD, Rawlinson AJ (2005) Flow visualisation of the external flow from a converging slot-hole film-cooling geometry. Exp Fluids 38:304–318

Savory E, Syes DM, Toy N (2000) Visualization of transition on an axisymmetric body using shear sensitive liquid crystals. Opt Diag Eng 4:16–25

Scala LC, Dixon GD (1969) Long term stability of cholesteric liquid crystal systems. Mol Cryst Liq Cryst 7:443–455

Scala LC, Dixon GD (1970) Long term stability of cholesteric liquid crystal systems 2. Mol Cryst Liq Cryst 10:411–423

Scarano F (2002) Iterative image deformation methods in PIV. Meas Sci Technol 13:R1–R19

Scarano F, Riethmuller ML (2000) Advances in iterative multigrid PIV image processing. Exp Fluids(Suppl) S52–S60

Schöler H (1990) Thermal imaging on missiles in hypersonic flow. AGARD fluid dynamics symposium on "Missile Aerodynamics" Friedrichshafen, Germany 22–26 29:1–29:5

Shusser M, Gharib M (2000) Energy and velocity of a forming vortex ring. J Fluid Mech 416:173–185

Sillekens JJM, Rindt CCM, van Steevenhoven AA (1998) Development of laminar mixed convection in a horizontal square channel with heated side walls. Int J Heat Fluid Flow 19:270–281

Simonich JC, Moffat RJ (1982) New technique for mapping heat-transfer coefficient contours. Rev Sci Instrum 53:678–683

Smith CR, Praisner TJ, Sabatino DR (2000) Surface temperature sensing with thermochromic liquid crystals. In: Smits AJ, Lim TT (eds) Flow visualization, techniques and examples. Imperial College Press, Singapore, pp 149–167

Smith CR, Sabatino DR, Praisner TJ (2001) Temperature sensing with thermochromic liquid crystals. Exp Fluids 30:190–201

Soloff SM, Adrian RJ, Liu ZC (1997) Distortion compensation for generalized stereoscopic particle image velocimetry. Meas Sci Technol 8:1441–1451

Son C, Gillespie D, Ireland P, Dailey GM (2001) Heat transfer and flow characteristics of an engine representative impingement cooling system. J Turbomach 123:154–160

Spencer MC, Jones TV, Lock GD (1996) Endwall heat transfer measurements in an annular cascade of nozzle guide vanes at engine representative Reynolds and Mach numbers. J Heat Fluid Flow 17:139–147

Stasiek J (1997) Thermochromic liquid crystals and true colour image processing in heat transfer and fluid-flow research. Heat Mass Transf 33:27–39

Stasiek J, Stasiek A, Jewartowski M, Collins MW (2006) Liquid crystal thermometry and true-colour digital image processing. Opt Laser Technol 38:243–256

Stasiek JA, Kowalewski TA (2002) Thermochromic liquid crystals applied for heat transfer research. Opto-electron Rev 10:1–10

Sun JH, Leong KC, Liu CY (1997) Influence of hue origin on the hue-temperature calibration of thermochromic liquid crystals. Heat Mass Transf 33:121–127

Tanda G (2004) Heat transfer in rectangular channels with transverse and v-shaped broken ribs. Int J Heat Mass Transf 47:229–243

Tariq A, Ranigrahi PK, Muralidhar K (2004) Flow and heat transfer in the wake of a surface-mounted rib with a slit. Exp Fluids 37:701–719

Tariq A, Singh K, Panigrahi PK (2003) Flow and heat transfer in a rectangular duct with single rib and two ribs mounted on the bottom surface. J Enhanc Heat Transf 10:171–198

Teng S, Sohn DK, Han JC (2000) Unsteady wake effect on film temperature an effectiveness distributions for a gas turbine blade. J Turbomach 122:340–347

Toy N, Disimile PJ, Savory E (1999) Local shear stress measurements within a rectangular yawed cavity using liquid crystals. Opt Diag Engr 3:91–101

Trautman MA, Glezer A (2002) The manipulation of the streamwise vortex instability in a natural convection boundary layer along a heated inclined flat plate. J Fluid Mech 470:31–61

Treuner M, Rath HJ, Duda U, Siekmann J (1995) Thermocapillary flow in drops under low gravity analysed by the use of liquid crystals. Exp Fluids 19:264–273

Turner JS (1973) Buoyancy effects in fluids. Cambridge University Press, Cambridge

Uzol O, Camci C (2005) Heat transfer, pressure loss and flow field measurements downstream of staggered two-row circular and elliptical pin fin arrays. ASME J Heat Transf 127:458–471

Vejrazka J, Marty Ph (2007) An alternative technique for the interpretation of temperature measurements using thermochromic liquid crystals. Heat Transf Eng 28:154–162

von Wolfersdorf J (2007) Influence of lateral conduction due to flow temperature variations in transient heat transfer measurements. Int J Heat Mass Transf 50:1122–1127

Wagner E, Stephan P (2007) Frequency response of a surface thermometer based on unencapsulated thermochromic liquid crystals. Exp Therm Fluid Sci 31:687–699

Wagner G, Schneider E, von Wolfersdorf J, Ott P, Weigand B (2007) Method for analysis of showerhead film cooling experiments on highly curved surfaces. Exp Therm Fluid Sci 31:381–389

Wang Z, Ireland PT, Jones TV, Davenport R (1996) A color image processing system for transient liquid crystal heat transfer experiments. J Turbomach 118:421–427

Wang L, Sundén B (2004) An experimental investigation of heat transfer and fluid flow in a rectangular duct with broken v-shaped ribs. Exp Heat Transf 17:243–259

Westerweel J (1993) Digital particle image velocimetry—theory and application. PhD thesis, Delft University Press

Westerweel J (1997) Fundamentals of digital particle image velocimetry. Meas Sci Technol 8:1379–1392

Wiberg R, Lior N (2004) Errors in thermochromic liquid crystal thermometry. Rev Sci Instrum 75(9):2985–2993

Wierzbowski M, Stasiek J (2002) Liquid crystal technique application for heat transfer investigation in a fin-tube heat exchanger element. J Vis 5:161–168

Willert CE, Gharib M (1991) Digital particle image velocimetry. Exp Fluids 10:181–193

Woodmnasee WE (1966) Cholesteric liquid crystals and their application to thermal nondestructive testing. Mater Eval 24:564–566 571–572

Woodmnasee WE (1968) Aerospace thermal mapping applications of liquid crystals. Appl Opt 7:1721–1727

Wozniak G, Wozniak K, Siekmann J (1996) Non-isothermal flow diagnostics using microencapsulated cholesteric particles. Appl Sci Res 56:145–156

Wright WD (1928–1929) A re-determination of the mixture curves of the spectrum. Trans Opt Soc Lond 30:141–164

Wyszecki G, Stiles WS (1982) Color science: concepts and methods, quantitative data and formulae. Wiley, New York

Yan X, Saniei N (1996) Measurements of local heat transfer coefficients from a flat plate to a pair of circular air impinging jets. Exp Heat Transf 1:29–47

Yan X, Saniei N (1997) Heat transfer from an obliquely impinging circular air jet to a flat plate. Int J Heat Fluid Flow 18:591–599

Yan Y, Owen JM (2002) Uncertainties in transient heat transfer measurements with liquid crystal. Int J Heat Fluid Flow 23:29–35

Yoon SH, Kim MS (2002) Investigation of circumferential variation of heat transfer coefficients during in-tube evaporation for R-22 and R-407C using liquid crystal. ASME J Heat Transf 124:845–853

Young T (1802) On the theory of light and colours (The 1801 Bakerian Lecture). Philos Trans R Soc Lond 92:12–48

Yuen CHN, Martinez-Botas RF (2005) Film cooling characteristics of rows of round holes at various streamwise angles in a crossflow: part II. Heat transfer coefficients. Int J Heat Mass Transf 48:5017–5035

Zhang X, Stasiek J, Collins MW (1995) Experimental and numerical analysis of convective heat transfer in turbulent channel flow with square and circular columns. Exp Therm Fluid Sci 10:229–237

Zharkova GM, Streltsov SA, Khachaturyan VM, Samsonova I (1999a) Selective reflection of light from aqueous dispersions of encapsulated cholesteric liquid crystals. Mol Cryst Liq Cryst 331:635–642

Zharkova GM, Streltsov SA, Khachaturyan VM (1999b) Aqueous dispersions of cholesteric liquid crystals and their optical properties. J Struct Chem 40:419–423

Zhong S, Kittichaikan C, Hodson HP, Ireland PT (1999) A study of unsteady wake-induced boundary-layer transition with thermochromic liquid crystals. Proc Inst Mech Eng 213:163–171